Madeleine Hystad

The distribution and impact of chromium impurities in compensated SoG-silicon

Master thesis

Trondheim, Spring 2009

Supervisors:

Lars Arnberg
Astrid L. Ramstad

The Norwegian University of Science and Technology

NTNU
Innovation and Creativity

Preface

The work of this thesis has been conducted at the Department of Materials Science and Engineering at the Norwegian University of Science and Technology (NTNU) from spring 08 through spring 09. The report presents the results of the investigation of chromium impurities in solar grade silicon.

The master thesis project has been performed independently, honest and in accordance with the Examination Regulations at NTNU.

Trondheim, May 2009.

Madeleine Hystad

Acknowledgement

Many people have been involved in my work over the last three semesters and they all deserve recognition and gratitude for their contributions.

My supervisor, Professor Lars Arnberg, deserves the greatest thanks for guiding me through the amazing and comprehensive field of silicon and solar cells. Thank you for always taking the time to discuss every achievement, proceeding and challenges that I've encountered on my way. Your support and engagement is invaluable.

I could not have made this thesis feasible without the effort and contribution from Chiara Modanese and Marisa Di Sabatino. Thank you both for all your help, effort and training on instruments like GDMS, resistivity, EBSD, PVScan and FTIR. Our close collaboration, inspiring conversations and your encouraging words are highly appreciated.

Thanks are also addressed to the project leader, Ragnar Fagerberg, for your interest, involvement and valuable input.

My non-technical co-supervisor, Astrid L. Ramstad, deserves thanks for reading through my thesis, correcting misspellings etc.

Financial support of my master thesis by Elkem Solar and the Norwegian Research Council is greatly acknowledged. A special thanks to Anne-Karin Søiland at Elkem Solar for her participation and follow-up.

I will also like to thank the following persons for their helping hand:
Martin Syvertsen (casting), Birgitte Karlsen (coating of crucibles and etching), Ove Darell (cutting of ingot), Dr. Kristian Peter og Pedro Diaz-Perez at International Solar Energy Research Center (ISC) in Konstanz (solar cell processing), Morten Peder Raanes (microprobe), Arve Holt, Rune Søndenå and Bent Thomassen at IFE (gettering and FeB/CrB pair experiments), Øystein Dahl (EBIC and Auger) and Gaute Stokkan (CDI).

My fantastic dancing girls and the loyal lunch gang should also be credited for sticking around through ups and downs.

To my amazing parents and little brother: with all my love, thank you!

At last, Tore, thank you for everything. Thank you for reading through all my master thesis drafts and involving in my work. Thank you for supporting me, giving me attention when needed, taking care of me and, finally, for always being there for me.

Abstract

The metallurgical refinement of silicon is one of the novel production processes developed for producing silicon exclusively for solar cells. The compensated solar grade (SoG) silicon generally contains a higher level of impurities than polysilicon. In these contaminated materials the impurity distribution, interaction between several impurity elements, and interaction between impurities and crystal structure, is not known. Investigations must be performed in order to determine how significant the impurities impact the electronic bulk properties of silicon.

This report presents an investigation of the effect of chromium on compensated SoG-silicon. Two ingots were cast with compensated feedstock from Elkem Solar and the addition of 50 ppmw chromium. The concentration and distribution of impurity elements were measured. Microstructure imaging such as grain orientation and dislocation density, as well as investigations on the electrical properties including resistivity, minority carrier lifetime and solar cell characteristics, were performed.

High concentrations of phosphorus and boron were present, but no majority carrier type transition (p- to n-type) occurred due to breakdown of the planar solidification front in the top of the ingot. An investigation of transition elements by GDMS detected only traces of chromium, iron and titanium at half ingot height, close to the detection limit of the instrument. Even at these low concentrations chromium degraded the electrical properties of the material, where regions with highest obtainable lifetimes corresponded to 1 μs.

Lifetime will vary according to the dominating defect state of chromium or iron. The material did not show changes in lifetime after light soaking or heat treatment, therefore a study of their respective pairs did not succeed.

Chromium possesses excellent gettering properties and a phosphorus diffusion gettering process enhanced the minority carrier lifetime by two orders of magnitude. This also implies that chromium is mostly found dissolved in the silicon lattice as an interstitial specie. Furthermore, the lowest lifetime regions before gettering corresponded to grains and twins, indicating the crucial extent of point defects originating from interstitial chromium. The lifetime improvement observed in gettering experiments are also reflected in the solar cell characteristics. The efficiencies matched polysilicon cells with efficiencies around 14 %. The results imply that moderate concentrations of fast diffusing impurities are acceptable as long as low energy precipitation sites are within the diffusion length of the impurities during gettering.

Table of content

1 Introduction

Renewable energy resources are of great immediate interest and are, therefore, given considerable attention in diverse fields of research. Photovoltaic (PV) cells are one of the alternatives in sustainable energy development. With an impressive market growth of 110 % in 2008 (62 % in 2007) and an annual growth exceeding 20 % each of the last years [1], PV-cells have demonstrated their potential as an alternative energy source and will be a future research area in many years to come.

Although several materials are available for PV-cell production, most solar cells manufactured today are made from multicrystalline (mc) silicon. Shortage of silicon feedstock provides a challenge for the PV-industry. This together with the fact that 25-50 % [2] of the total cost of making a solar cell is constituted by silicon material, stimulates the extensive search for feedstock material and novel production processes, as well as intensifying the research on the detrimental properties of impurity elements present in new silicon feedstock.

Today only 15 % - 18 % of the sun's radiation is exploited and converted to electricity although the potential for a single cell with optimum band gap is approximately 33 % [3]. This is due to several factors, but the main ones are impurity elements and defects in the material. It is well known that even small concentrations of impurities (ppb level) will influence the properties of silicon material, and hence the electronic properties of the complete solar cell [4].

The feedstock is the greatest contributor of impurities to silicon, but significant amounts also enter the silicon during the solidification step. The impurities will, among other factors, contribute to a reduction in the solar cell conversion efficiency. Defects in the crystal lattice, e.g. grain boundaries and dislocations, are also contributors to this.

The content and tolerance of the most abundant impurity elements are relatively well known in standard polysilicon produced from the Siemens process. However, in more novel production processes, like metallurgical refined silicon as produced by Elkem Solar (ES), more knowledge concerning the sensibility, tolerance and impact of these elements is needed.

This thesis will contribute to this by presenting tentative work on the effect of chromium in silicon material from Elkem Solar, and the interaction with other impurities. A laboratory scale ingot has been doped with chromium. Investigations on the cast ingot provided information on distribution of elements in the ingot, grain- and defect structure, as well as investigations on electronic properties such as resistivity and carrier lifetime. Solar cells have also been processed, and a representative selection of characterization techniques has been applied.

The ultimate objective is to establish how the impurities behave, interact and influence silicon with different processing conditions and casting technologies, to be able to control the quality of the material. This will, among other factors, be a step towards developing better material with higher efficiencies at a lower cost, and subsequently be comparable to other renewable energy sources.

Chromium is an interesting impurity element in mc-silicon which degrades the electrical properties of the material. Even though it is present in concentrations comparable to that of iron, it is not known whether the two transition elements behave similarly. Moreover, little has been published about chromium in silicon.

The work performed has not only included investigations on as-cast material, but expands the aspect of the research by incorporating the characteristics of solar cells made of the same material. Therefore a closer connection between material quality and behavior of the complete solar cell can be studied.

The background for understanding the theoretical part, results and discussions in the thesis are presented first, followed by a more detailed section of impurities in silicon. Chromium and its interaction with silicon and dopants will constitute the main part of this section, but also a complementary section about iron and some details about aluminum are given. Principles of some of the characterization techniques used are described. Furthermore, results will be discussed in the prospective of silicon's properties and similar work performed by others. Finally, conclusions and suggestions for further work are proposed.

2 Theoretical Background

This section will present a brief background in order to introduce the reader to subjects that are essential for understanding later discussions. Topics treated will be the foundation of the work performed.

2.1 Basic principles of a solar cell

A solar cell consists of both boron-doped and phosphorus-doped silicon regions, more commonly referred to as p-type and n-type material respectively. Boron contains one electron less than silicon in its valence shell and thus p-type silicon will have an excess of positive charges. The *major* charge carrier will then be holes (positive charges) while the *minority* charge carriers are electrons (negative charges). For n-type material the situation is completely reversed, hence holes are the minority charge carriers [3, 5].

The interface between the two regions is called a pn-junction. Due to excess concentration of opposite charges in the two types of materials, diffusion of charges across the junction will occur when the pn-junction is established, which subsequently introduces an electric field that opposes any further charge flow [5].

The p- and n-type material is connected to each of the contacts of an external circuit. When light shines upon a solar cell, free minority charge carriers, which can conduct electricity, are generated. Generated electrons will flow from p-type to n-type region while holes will flow in the opposite direction producing a net current. A basic sketch of these principles is shown in Figure 1.

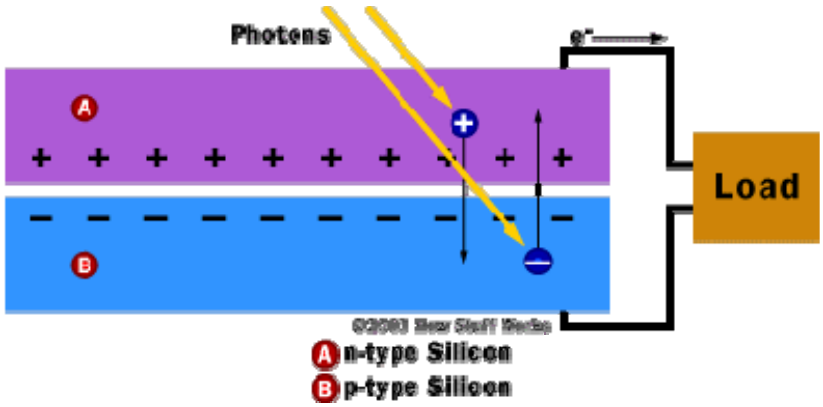

Figure 1: The basic principles of a solar cell when light (photons) shines upon a silicon cell. Charge carriers are forced to move through the external circuit and hence the electricity can be utilized [6]

Other characteristics of a solar cell are anti-reflecting coating which reduce the reflectivity, and a reinforcing material at the back as well as a glass cover plate on top to provide mechanical rigidity [5].

2.2 Elkem Solar's metallurgical upgrading process

Production of ingots for solar cell processing by the Elkem Solar process involves a five-step procedure for upgrading the material from metallurgical grade (MG) silicon to solar grade (SoG) quality. The process is illustrated in Figure 2.

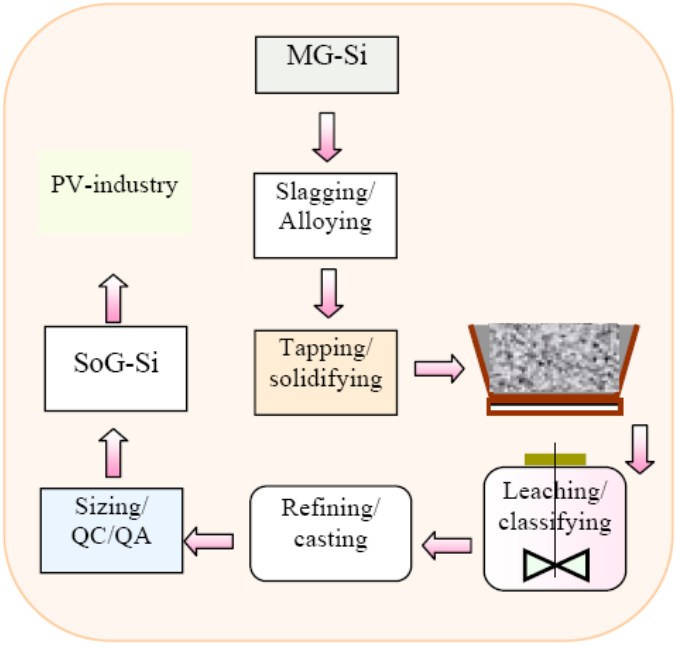

Figure 2: The Elkem Solar process for upgrading silicon from MG-silicon to SoG-silicon [7]

The first step is to produce metallurgical grade silicon from raw materials, including quartz, carbon and coke. Then the MG-silicon is slag treated to extract boron from the silicon. The silicon is solidified, precipitating pure silicon crystals, and leaving the impurities in the melt until the end of the solidification where the impurities segregate to the grain boundaries of the alloy. The grain boundary phases are dissolved and removed in a hydro-metallurgical step using leaching. Directional solidification in the fourth step is applied to refine the silicon further. At last the upgraded silicon material is cleaned and sized in a post-treatment. [7]

The upgraded metallurgical silicon produced in the Elkem Solar process contains relatively high concentrations of boron and phosphorus compared to polysilicon and is classified as a compensated material. Thus, a compensated material is defined as a material that contains significant amounts of donors (phosphorus) and acceptors (boron). However, it has not yet been clearly established how the degree of compensation should be defined; two alternatives from recent publications are given below [8, 9]:

$$C_l = \frac{N_D}{(N_A - N_D)} \tag{2.1}$$

$$R_C = \frac{(N_A + N_D)}{(N_A - N_D)} \tag{2.2}$$

C_l is the referred to as the level of compensation while R_C is the compensation constant. N_A and N_D are the total acceptor (boron) and donor (phosphorus) concentration respectively. The dopants are inhomogeneous distributed throughout the ingot due to the different distribution (segregation) coefficients, as will be presented later, and can sometime be evident as a p- to n-type transition along the height of the ingot.

The effect of compensation includes reduction in free carrier concentration, shift of Fermi level closer to mid-band gap, increase in *minority* carrier lifetime and decrease in *majority* carrier mobility [10]. In addition, the recombination strength of transition metal impurities and occupation of defect levels introduced in the silicon band gap are factors which must be considered [8].

Dopants can form complexes with impurities, especially light elements and especially when both species are present in high concentration, where the complexes can act as strong recombination centers. [11]

Elkem Solar's metallurgical refining process is assumed to be more cost effective and less energy consuming than traditional routes [7]. Solar cells produced from 100 % Elkem Solar feedstock have achieved efficiencies comparable to standard solar cell silicon. Even though the material contains higher concentration of impurities it is assumed that these impurities are confined to specific defects in the material, and therefore does not impact the solar cell conversion efficiency significantly more than solar cells produced from cleaner material [10].

2.3 Directional solidification

During directional solidification it is assumed that a local equilibrium exists close to the solid-liquid interface. Most impurity elements (e.g. Fe, Cr, B, Al) are more soluble in liquid silicon than the solid phase due to a negative liquidus slope and hence have a distribution coefficient, k_0, less than unity, as sketched in Figure 3.

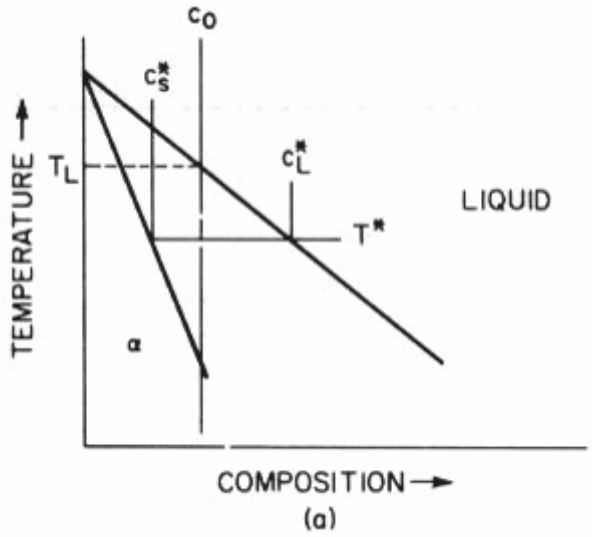

Figure 3: A small extraction of the phase diagram of alloyed silicon under equilibrium conditions. It is assumed that the liquidus and solidus lines are straight (i.e. k_0 is constant) for the range of compositions shown here [12]

The equilibrium distribution coefficient, k_0, is given as the solid to liquid solute concentration at the interface:

$$k_0 = \frac{C_s^*}{C_l^*} \tag{2.3}$$

C_s* is the solute concentration in the solid phase and C_l* is the solute concentration in the liquid phase at the solid liquid phase boundary. For straight solidus and liquidus lines k_0 will be constant. When $k_0 < 1$ the solute is rejected from the solid into liquid phase leaving concentration variations in the solidified silicon referred to as segregation. Concentration of the solute as a function of the fraction solidified can be described by the Gulliver-Scheil equation assuming complete mixing in the liquid phase and no diffusion in the solid phase:

$$C_s^* = k_0 C_0 (1 - f_s)^{(k_0 - 1)} \tag{2.4}$$

Where C_0 is the initial solute concentration [12, 13].

Table 1 gives an overview of various impurity elements and their equilibrium distribution coefficient, also referred to as segregation coefficient. Notice that oxygen and boron have a distribution coefficient close to unity, hence, only a slight segregation can occur.

Table 1: An overview of the equilibrium segregation coefficient, k_0, for various elements in silicon as given by two different references

Element	k_0	Ref.
Al	$2.0 \cdot 10^{-3}$	[14]
B	0.8	[14]
C	0.07	[15]
Cr	$1.1 \cdot 10^{-5}$	[16]
Cu	$1.5 \cdot 10^{-5}$	[14]
Fe	$8 \cdot 10^{-6}$	[14]
N	$7 \cdot 10^{-4}$	[15]
Ni	$3.0 \cdot 10^{-5}$	[17]
O	1.4	[15]
P	0.35	[14]
Ti	$3.6 \cdot 10^{-6}$	[16]

Towards the end of the solidification high concentrations of impurities (solute) can be present in the liquid phase and cause constitutional undercooling and breakdown of the solidification front. This will lead to uncontrolled growth, like dendrite growth and nucleation of new grains [18].

Istratov et al. [19] investigated how cooling rates affect the impurity distributions and observed that slow cooling rates leave larger metal precipitates with low density between each precipitation, while faster cooling favors more homogeneously distributed metal precipitates. A sufficient convective flow in the melt can to some extent postpone the direct precipitation of impurities until the end of the solidification as they are distributed away from the proceeding solidification front [18].

2.4 Recombination

2.4.1 Minority carrier lifetime

Light with adequate wavelength shining on a semiconductor excites an electron, generating an electron-hole pair, and creates excess carriers that are free to move throughout the material. The excess carriers will eventually recombine with a carrier of opposite charge, and hence carrier lifetime and net recombination rate can be defined for electron and holes respectively [5]:

$$\tau_e = \frac{\Delta n}{U}$$
$$\tau_h = \frac{\Delta p}{U} \quad (2.5)$$

Where U is the net recombination rate and Δn and Δp are the excess carrier concentrations. The distance a charge carrier can diffuse before it is recombined is referred to as the diffusion length [5], here given for an electron being the charge carrier:

$$L_e = \sqrt{D_e \tau_e} \quad (2.6)$$

D_e is the diffusion coefficient for electrons which is dependent upon the mobility of the charge carrier, and τ_e is the lifetime as defined above.

Minority carrier lifetime is related to the diffusion length of the carriers in silicon and hence also represents the solar cell performance. However, it can be expected that real lifetime in the solar cell are enhanced compared to as-cut silicon due to thermal treatments during solar cell processing [3]. A more detailed explanation for this is given in a later Section (3.5) about gettering techniques.

2.4.2 Mechanisms of recombination

There are three different mechanisms for recombination of electrons and holes; Auger, Radiative and Shockley-Read-Hall (SRH) [5, 20]. When an electron relaxes and recombines with a hole, the excess energy can be transferred to another electron either in the conduction band or the valence band as shown in Figure 4. The other electron will also relax after a while to its original state emitting phonons. This is what is called an Auger recombination [5].

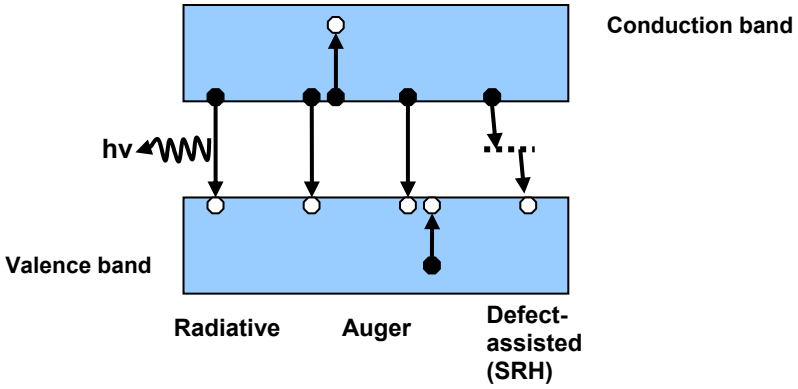

Figure 4: The three recombination mechanisms in mc-silicon. Reconstructed from [21]

An electron making a transition to an energy state lower in energy, without transferring the excess energy to another electron, can emit light with wavelength corresponding to

the distance between the two energy levels. The process is called radiative recombination. Due to silicon being an indirect band gap material radiative recombination can only occur through a two-step process involving a phonon, as illustrated in Figure 5. Thus it is not commonly observed for indirect band gap semiconductors. [5]

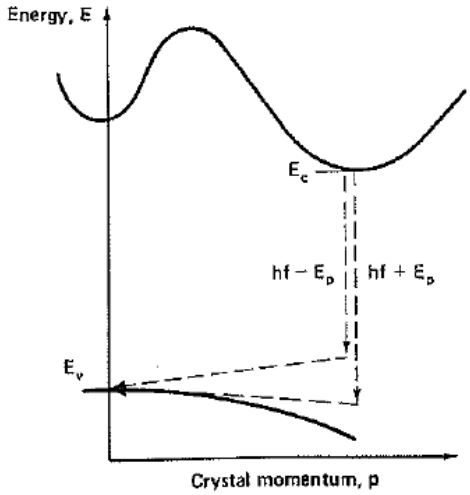

Figure 5: A two-step process is required for radiative recombination to occur in silicon and other indirect band gap semiconductors. Shown here are two alternative pathways for electrons to relax [5].

SRH recombination is by far the most common recombination process in silicon and involves recombination through defect or trap energy states located within the silicon band gap. If the trap captures a minority carrier (electron or hole depending on the type of doping), and before releasing it also captures another carrier of opposite charge, the two will recombine. [3]

The net minority carrier lifetime will be a factor of the three bulk processes and is defined as [3]:

$$\frac{1}{\tau_{tot}} = \frac{1}{\tau_{SRH}} + \frac{1}{\tau_{Rad}} + \frac{1}{\tau_{Aug}} \tag{2.7}$$

Where SRH is the Shockley-Read Hall, Rad the radiative and Aug is the lifetime due to Auger recombination.

Impurities and defects in the silicon lattice typically introduce trap states causing SRH recombination and hence are the two main reasons for degradation of efficiency in mc-silicon. This thesis will consider the effect of impurities, mainly chromium, present in mc-silicon, while crystal defects have been carefully studied by others [22-24] and are beyond the scope of this thesis. Impurities in mc-silicon drastically lower the minority carrier lifetimes by recombination mechanisms as described above.

In general, n-type material has a greater tolerance for impurities than p-type since holes are not significantly influenced by point defects [25]. However, this is not true for chromium, which affects both p-type and n-type similarly. Complementary discussions about this will be presented in Section 3.7.2.

n-type material has several advantages over p-type, including absence of boron-oxygen complexes and low variation of minority carrier lifetimes with injection level [26]. Yet challenges remain for it to be commercialized, the main one being the need for a good emitter to create a p-n-junction [25]. Investigations on the properties of chromium in silicon are thus also of significance in the steps towards commercialization of n-type material production.

2.5 Solar cell properties

Parameters as open circuit voltage (V_{OC}), short circuit current (I_{SC}) and fill factor (FF) characterize the performance of a solar cell. They influence the efficiency of the solar cell (η) altogether. Expressions for each of the parameters as well as factors that affect them will be presented. Reductions in the solar cell efficiency can be due to many reasons; some of them are given in the sections below.

2.5.1 Short circuit current

Which semiconductor material that is employed and its characteristics will affect the short circuit current obtained. The short circuit current are current withdrawn from the solar cell circuit when the two terminals in the cell (like on a battery) are connected. Illuminated conditions are a prerequisite. [3]

I_{SC} is assumed to be roughly proportional to the area under illumination and another designation is often applied instead, referred to as the short circuit current density, J_{SC} [3]. The number of minority carriers that diffuse to the junction before being recombined determines the short circuit current density.

By neglecting the recombination but including the generation of carriers in the space-charge region the change in current density for electrons and holes in this particular region of the cell gives Equation (2.8) [5]:

$$\left|\delta J_e\right| = \left|\delta J_h\right| = qGW \tag{2.8}$$

G is the generation rate and W the width of the depletion region given by the sum of the diffusion lengths of electrons and holes, $L_e + L_h$. For solar cell based on p-type silicon the expression can be simplified to give the short circuit current density [27]:

$$J_{SC} = qG_eL_e \tag{2.9}$$

q is the electronic charge while e is abbreviation for electron which is the minority carrier in p-type material.

The maximum short circuit current obtainable is given by the number of photons incident on the solar cell with energy larger than the band gap energy of the silicon. Furthermore, by decreasing the band gap the short circuit current will increase. [5]

Loss of short circuit current is principally due to optical challenges. Much of the light absorbed are reflected from the surface of the solar cell. An anti-reflection coating will reduce this loss. Metal contacts on both front and back of the cell reduce the area which can be exposed to illumination. Recombination of free carriers at surfaces or in the bulk sufficiently far away from the junction also contributes to I_{SC}/J_{SC} losses.

2.5.2 Open circuit voltage

When terminals in a solar cell are isolated from each other a voltage is produced which is referred to as the open circuit voltage [3]. V_{OC} depends on the silicon material properties, mainly through the saturation current density, I_0. The saturation current density is the maximum current that can flow through a circuit without dissipation of heat. The intrinsic concentration of carriers in un-doped silicon, n_i, are a function of the density of electrons and holes and hence also the material properties [5].

The expression for V_{OC} is given in Equation (2.10) [5]:

$$V_{OC} = \frac{kT}{q} \ln\left(\frac{I_L}{I_0} + 1\right) \tag{2.10}$$

T is the temperature, k the Boltzmann constant and q the electronic charge. The three constitutes a constant equal to 26 mV at room temperature. I_L is the light generated current. For a maximum open circuit voltage I_0 must be as small as possible.

Alternatively the expression can be written as a function of free carrier densities, Δn, at the edge of the space-charge region (depletion region), i.e. the area around the junction where carrier concentrations are very small, and the intrinsic concentration, n_i^2 [27]:

$$V_{OC} = \frac{kT}{q} \ln\left(\frac{\Delta n(N_A + \Delta n)}{n_i^2}\right) \tag{2.11}$$

If the band gap of the material decreases, the maximum obtainable open circuit voltage will also decrease. Recombination of minority carriers will, as for I_{SC}, result in losses in V_{OC}. The potential maximum V_{OC} is limited by the inherent capability of the pn-junction to give only a fraction of $V_{OC\,max}$. [5] High temperatures have a negative effect on the open circuit voltage which decreases 2.3 mV per ºC [28].

2.5.3 Fill factor and efficiency

The current-voltage characteristics of a solar cell will decide the possible power output. At a certain voltage (V_{mp}) and current (I_{mp}) the output is at its utmost. This is shown below in Figure 6.

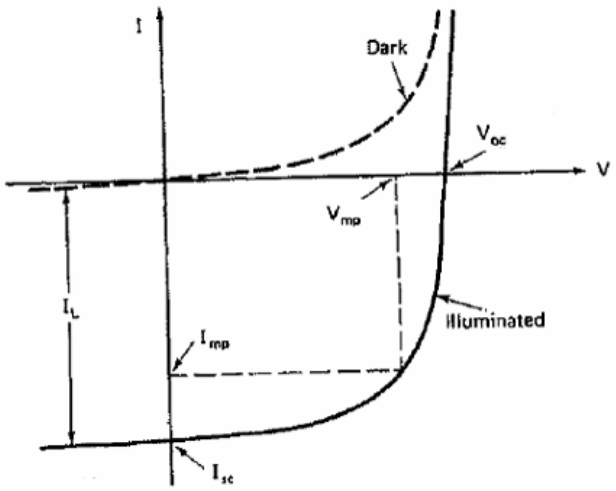

Figure 6: The I-V characteristics of pn-junction when illuminated and in the dark

The fill factor is a measure of the area of the square defined by $V_{mp}I_{mp}$ according to the expression [5]:

$$FF = \frac{V_{mp} I_{mp}}{V_{OC} I_{SC}} \tag{2.12}$$

The greatest achievable fill factor for silicon is 0.84 corresponding to an open circuit voltage of 700 mV.

Since the FF is a function of V_{OC} and I_{SC} their mechanisms for losses can be applied in this case as well. Series resistance and shunt resistance are features to take into consideration when it comes to fill factor losses. Bulk resistance in the silicon material itself, bulk resistance of the metal contacts and contact resistance in the connection between silicon and metal are all accounted for in the series resistance loss, while shunt resistance is a result of leakage at the pn-junction due to large precipitates/particles and crystal defects. [5]

The solar cell efficiency is a function of the fill factor:

$$\eta = \frac{V_{OC} I_{SC} FF}{P_{input}} \tag{2.13}$$

P_{input} is the power input from the illumination incident on the solar cell.

There is one fundamental loss mechanism that limits the solar cell efficiency. Even though some photons have twice the energy of the band gap only one electron can be excited into the conduction band. Hence, as long as the energy of the photon is larger than the band gap energy it doesn't matter how much larger it is. Each semiconductor material can thus exploit only parts of the solar spectrum. [5]

Typical performance characteristics of silicon solar cells are given in Table 2.

Table 2: Solar cell parameters for different silicon materials, reconstructed from [29]

Cell type	Area [cm^2]	V_{OC} [mV]	J_{SC} [mA/cm^2]	FF	η [%]
Crystalline Si	4.0	706	42.2	82.8	24.7 ± 0.5
Multicrystalline Si	1.0	664	37.7	80.9	20.3 ± 0.5
Amorphous Si	1.1	859	17.5	63.0	9.5 ± 0.3

A shown for amorphous silicon, cells with large V_{OC} tend to have small J_{SC} due to the different band gap relation.

Zahedi *et al.* [7] reported solar cell parameters from previous investigations of Elkem Solar silicon feedstock cast in a Crystalox DS250 furnace. The results are shown in Table 3 and correspond to an average value of several cells.

Table 3: Solar cell performance of five different lab-scale ingots cast with Elkem Solar silicon feedstock. Also included is two reference cells, ref is processed in the same batch as the other cells while com ref is a commercial reference cell. Table is reconstructed from [7]

Ingot no.	Area [cm^2]	Res. [Ω cm]	FF	J_{SC} [mA/cm^2]	V_{OC} [mV]	<η> [%]
1	100	0.21	72	27	607	11.6
2	156	0.50	74	30	614	13.3
3	156	0.42	74	26	596	11.0
4	156	1.00	74	30	600	13.1
5	156	1.00	75	31	609	13.9
Ref.	100	0.74	74	29	608	11.3
Com ref.	156	-	75	32	612	14.6

High oxygen content is the reason for low cell efficiency in the reference (not com ref). Some deviation in resistivity is also partly responsible for different cell performances [7]. With an adapted lab-type solar cell processing efficiencies exceeding 18 % have been achieved from cells consisting of Elkem Solar feedstock [30]. Furthermore, with a standard industrial cell processing an average efficiency of 15.4 % has been recorded, with 100 % Elkem Solar Silicon (ESS^{TM}) [31].

3 Impurities in mc-silicon

A literature study of impurity elements present in mc-silicon, their concentration range and detrimental effect is presented in this chapter. Gettering, a common technique for rendering the impurities partly harmless, is also described. The main focus is however on the characteristics and behavior of chromium and iron impurities as well as their interaction with other impurities and defects.

3.1 Previous work on impurities

Davis *et al.* [4] did fundamental work on the effects of metallic impurities on silicon for solar cells by adding controlled amounts of dopants to Czochralski (monocrystalline) silicon. In addition they developed a model that predicts the solar cell conversion efficiency as a function of a single metal impurity concentration present in the material, as shown in Figure 7 [4]. It should be noted that metal impurities both interact with each other and defects in mc-silicon and care should be taken when interpreting and comparing results with Davis *et al.*'s work. Ludwig and Woodbury [32, 33] early recognized the effect of impurities on solar cell material and the interaction between elements. It lead to a comprehensive study of transition metal impurities in silicon.

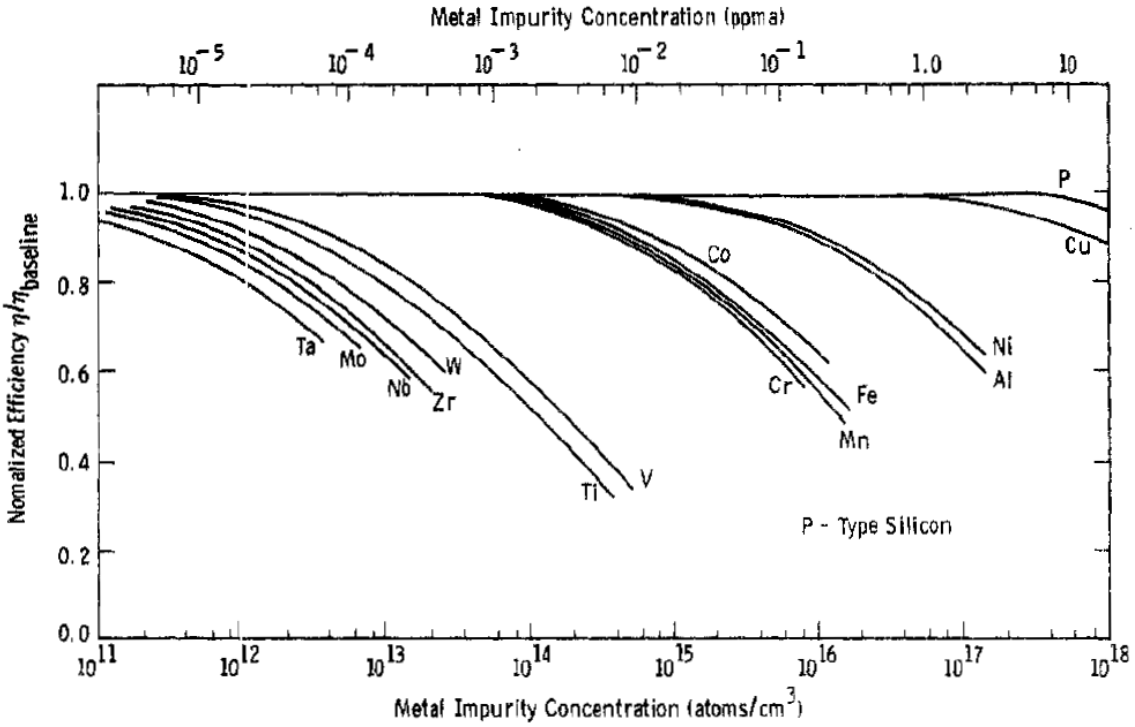

Figure 7: The effect of metal impurity concentrations in silicon as a function of efficiencies, as computed by Davis *et al.* [4]

3.2 Distribution of impurities

Impurities present in SoG-silicon are mainly introduced by the feedstock material, as mentioned previously, but also crucible, coating and gas components developing from furnace parts can be a source of contamination to the melt. Especially during directional solidification the solid-state in-diffusion from crucible and coating plays an important role due to very long crystallization and cooling times [34, 35].

The most common impurity elements found in SoG-silicon include iron, chromium, copper, titanium, nickel, nitrogen, oxygen and carbon. They can be found either as dissolved atoms, interstitially or substitutionally in the crystal lattice, as inclusions, precipitates or as complexes with substitutional boron [36].

When the solubility limit is reached precipitates are formed either directly from the melt or in the solid silicon during cooling, as solubility is highly temperature dependent. Maximum solid solubility of a selection of impurities is given in Table 4. Typical sites of precipitation in mc-silicon are grain boundaries and defects in the crystal lattice, serving as lower energy, and thus more favorable, sites. Inclusions typically consist of oxides or silicates and other non-metallic particles. [25]

Table 4: Solid solubility of dopants and impurities in silicon for a given temperature

Impurity	C_s^m [atoms/cm^3]	T [°C]	Ref.
Al	$2.0 \cdot 10^{19}$	1100	[14]
B	$6.0 \cdot 10^{20}$	1420	[14]
Cr	$1.0 \cdot 10^{14}$	1200	[37]
Fe	$3.0 \cdot 10^{16}$	1325	[14]
O	$3.0 \cdot 10^{18}$	1420	[15]
P	$1.3 \cdot 10^{21}$	1200	[14]

All 3d transition elements present in mc-silicon are positively charged due to the formation of a donor level in the silicon band gap. Coulombic attractions act between transition elements and boron, which behaves as an acceptor when present in silicon, combining them to a neutral complex (element-B) [38]. Aluminum possesses the same acceptor characteristics as boron and can also form complexes with transition metals [8]. However, little literature has been published about the topic, and the extent of the element-Al pairs and their effect is uncertain.

Concentration, chemical state and location of impurity elements in the cast ingot are controlled by several mechanisms, the most important ones are given in Figure 8 [25, 35].

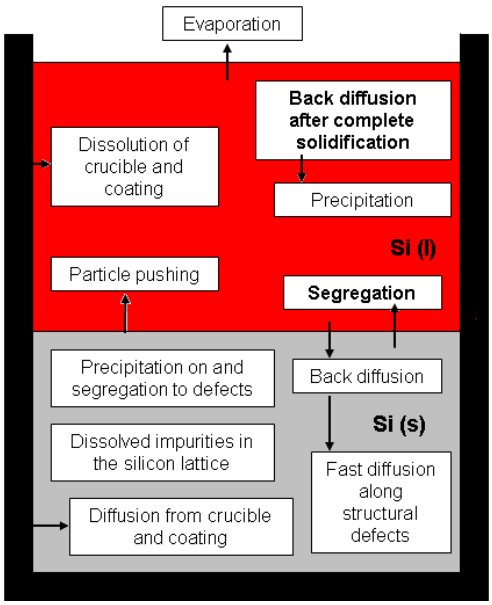

Figure 8: The processes occurring during casting that influence the final chemical distribution of impurities. Segregation and back diffusion, as marked in bold, are the greatest contributors. Figure is reproduced from [25, 35].

Segregation and back diffusion after complete solidification are the greatest contributors to the overall distribution. The distribution due to segregation can be calculated by the Gulliver-Scheil's equation, but this equation does not account for back diffusion [25]. Back diffusion is a solid-state phenomenon where impurities diffuse from the top of the solidified ingot back into the bulk. It can be observed as a maximum in the impurity concentration (e.g. Cr) around 95 % height of the ingot instead of at the very top (100 %), as first expected.

3.3 Concentration of impurities

Even though most transition metals are only present at ppb levels (~ 10^{11} - 10^{14} atoms/cm^{-3}) in mc-silicon, they have a significant effect on the electronic properties. Typical concentrations in mc-silicon given by Istratov *et al.* [39] and Macdonald *et al.* [40] are quoted in Table 5.

Table 5: Concentration of different transition elements in mc-silicon measured by NAA (Neutron Activation Analysis)

Element	Macdonald *et al.* (cm^{-3})	Istratov *et al.* (cm^{-3})
Fe	$1x10^{14}$	$4.7x10^{14}$
Cr	$2x10^{13}$	$1.9x10^{13}$
Cu	$2x10^{13}$	$<1.6x10^{14}$
Ni	$<3x10^{14}$	-
Co	$3x10^{11}$	$8x10^{12}$

According to Martinuzzi *et al.* [26] boron and phosphorus concentration in a upgraded metallurgical material are in the range of 10^{18} atoms/cm^3 (10-20 ppbw), while concentration of metallic impurities are in the range of 10^{16} atoms/cm^3.

Geerligs *et al.* [41] investigated the required impurity level in SoG-silicon feedstock for a 3 $\%_{rel}$ reduction of solar cell efficiency. This corresponded among others to an aluminum concentration less than 0.08 ppmw and 0.17 ppmw of titanium.

Elements like As, Sb, Sn and Zn are located on substitutional positions in silicon, while O, Ag, Co, Cr, Cu and Fe are interstitial elements [40]. The origin for this is mainly size related, except for atoms that fits perfectly into the structure of silicon like carbon does. Hence, carbon is also a substitutional element. Carbon and oxygen can pair up with other elements too (e.g. SiC or B-O complexes) and/or precipitate like the transition elements [36].

3.4 Transition elements in SoG-silicon

McHugo *et al.* [42, 43] observed a correlation between regions of low minority carrier lifetimes and the presence of iron, chromium and nickel precipitates in mc-silicon. Similar results are reported by Davis *et al.* [4] in a fundamental study of transition metal doped monocrystalline Cz-silicon.

Transition metal impurities present in the silicon are known to cause reduced solar cell conversion efficiency by introducing an energy donor level in the silicon band gap functioning as a trap and recombination centre [5]. The localization and capture cross-sections of the donor level in the band gap determines the recombination strength [25, 44]. Figure 9 indicates the location of energy levels introduced by various elements.

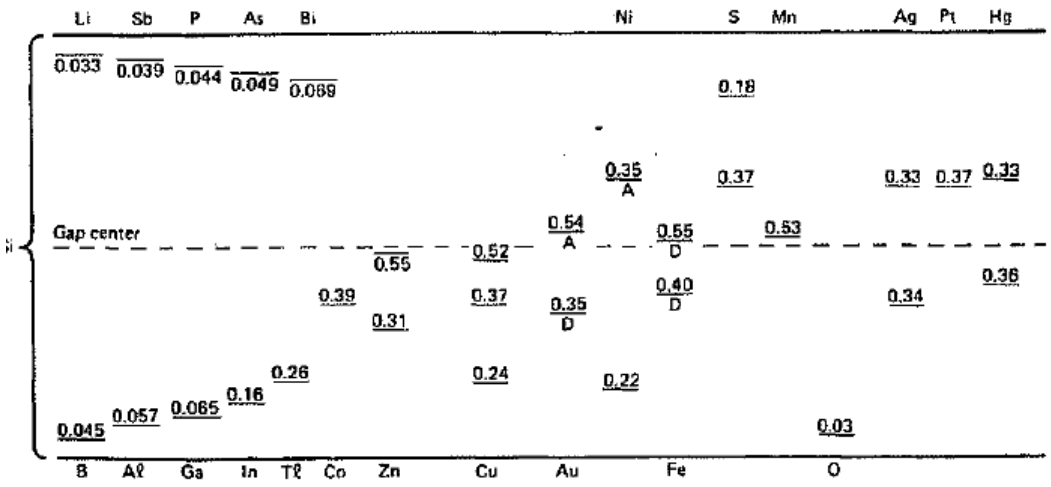

Figure 9: Energy levels introduced in the forbidden silicon band gap by impurities in mc-silicon. Denotation A is for acceptor, D is for donor [5]. Note that Cr is not included in this figure, but will be presented in later sections. Donor levels introduced by coupling of elements are neither included.

Donor levels located close to mid band gap, referred to as deep-level traps, are particularly detrimental to the electronic properties since a carrier relaxing from the conduction band can be trapped by the donor level long enough for the trap to also capture a carrier of opposite charge and thus recombining the two (SRH recombination described earlier). Such a recombination, sketched in Figure 10, decreases the minority carrier lifetime and the diffusion length in the material [3, 5].

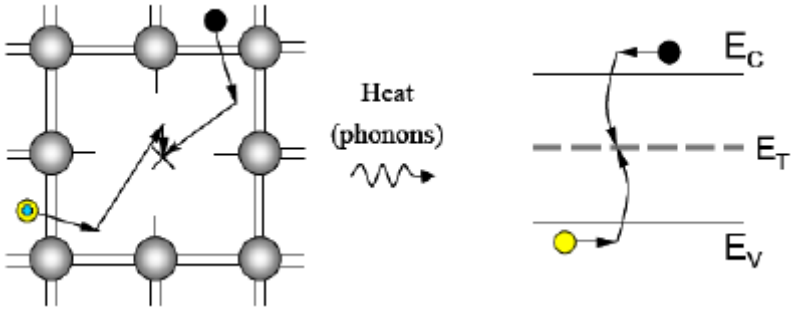

Figure 10: SRH recombination of carriers of opposite charge in the silicon lattice (left) and in more detail through a defect state located in the band gap (right) [45]

The distribution of impurity atoms throughout the silicon ingot, thus also the localization within the grains, is important when considering the extent of their detrimental impact. Istratov *et al.* claimed that it is the distribution of impurities, and not so much the total bulk concentration, that affects the solar cell efficiency [39]. Hence, UMG-silicon containing more impurities than polysilicon can still match the solar cell conversion efficiencies achieved with purer silicon, as shown in [30].

Precipitates lower the recombination activity per metal atom in comparison with homogeneously distributed impurities in the bulk [2]. Holt *et al.* explained this as decreasing density of precipitates with increasing size of precipitate clusters [46].

Buonassisi *et al.* [35] concluded with the same. As the average precipitation size increases, a reduction in density between precipitations, and an increase in the average carrier diffusion length occurs. This will in turn result in enhanced solar cell properties. Additionally, the capture cross-section for each impurity atom is reduced compared to dissolved atoms, assuming that both species introduce deep-levels.

The presence of impurities in precipitate clusters does by no mean render them completely harmless, but the impurities are less harmful than when they are finely dispersed. Dissolved atoms are more destructive due to the vigorous reduction in diffusion lengths [47]. Even though large precipitates clusters don't have a significant direct impact on minority carrier lifetime some of the atoms in the cluster can dissolve and affect the lifetime indirectly instead [35].

3.5 Gettering of impurities

Gettering is a high-temperature (800-900 ºC) technique where atoms diffuse through the silicon lattice to sites where they will cause less damage [43]. Gettering includes precipitation on energetically favorable sites at the surface or at defect sites within the bulk (i.e. grain boundaries and dislocations) as metal-silicides. Additionally, atom trapping at defects and segregation into other phases with higher solubility of these impurities than silicon are potential gettering sites [10]. Phosphorus or aluminum gettering, the two most common gettering techniques, can result in effective diffusion of impurities and an enhancement in lifetime. An improvement from 40 to 90 μs was observed by Cuevas *et al.* [48] after gettering of multicrystalline wafers with resistivity of 0.4 Ωcm. In an iron-doped multicrystalline ingot Kvande [25] investigated the lifetime before and after gettering, observing an enhancement of two orders of magnitude, while Ryningen [22] obtained doubling of the lifetime in SoG-silicon from Elkem Solar.

Even though dissolved and finely dispersed impurities are more harmful than precipitates, interstitial species especially, can be gettered much easier than precipitates because the latter have a much higher binding energy [43]. Macdonald *et al.* [40] concluded that some less tightly bonded precipitates can however be dissolved and become gettered. Macdonald *et al.* [40] also observed that phosphorus gettering did not change the concentration of some of the elements present in the silicon; all of them being substitutional species, while all the interstitial species investigated showed large differences in concentration before and after gettering. The reason for such a behavior is the difference in diffusivity of impurity elements present in mc-silicon. An overview of diffusion coefficients is given in Table 6 for various transition elements.

Table 6: Diffusion coefficients for interstitial transition elements present in silicon. Table is reconstructed from [49] which has collected data from various sources.

Element	D (Temp) [cm^2/s]	Temp. range [°C]
Co	$0.097 \cdot \exp\left(-\frac{1.79}{k_B T}\right)$	900-1100
Cr	$1.0 \cdot \exp\left(-\frac{1.0 \pm 0.3}{k_B T}\right)$	900-1250
Cu	$0.5 \cdot \exp\left(-\frac{0.4}{k_B T}\right)$	400-700
Fe	$0.62 \cdot \exp\left(-\frac{0.87}{k_B T}\right)$	1000-1250
Mn	$0.069 \pm 0.022 \cdot \exp\left(-\frac{0.63 \pm 0.03}{k_B T}\right)$	900-1200
Ni	$0.2 \cdot \exp\left(-\frac{0.47}{k_B T}\right)$	800-1300
Ti	$1.45 \cdot \exp\left(-\frac{1.79}{k_B T}\right)$	950-1200
V	$0.9 \cdot \exp\left(-\frac{1.55}{k_B T}\right)$	600-1200

After gettering low performance regions can still be found in the material due to the formation of more stable metal complexes instead of the gettering metal-silicide component. This is also the case for slow diffusing elements in silicon like titanium. Hence, extended duration of the gettering procedure is necessary to trap titanium. [50]

Other limiting factors to gettering, discussed by Perichaud *et al.*[50], is high oxygen concentrations limiting the external gettering, to some extent the carbon concentrations and defect density. When concentrations exceed $6 \cdot 10^{17}$ cm^{-3} a substantial degradation of the diffusion length can occur. Two mechanisms are competing; internal gettering by oxygen precipitates and external gettering by the phosphorus layer.

Regions with high dislocation density, especially when decorated with metal impurities, are of low performance. These regions have a tendency to react poorly to gettering and only minor improvements in minority carrier lifetimes, equivalent to diffusion lengths, occur [50]. Bentzen [51] attributed the low lifetime enhancement after gettering in some regions of the wafer to this phenomenon as well.

3.6 Donor species

Boron can form complexes with impurity elements like transition metals or oxygen. The same is true for aluminum. Donors like boron and aluminum can, to be discussed later, form complexes with transition metals. Boron and aluminum also pair up with oxygen to form an electrically active defect complex.

The formation of boron oxygen complexes occur under illumination. 4 minutes of illumination by 1 sun at 120 ºC was enough to introduce the boron oxygen pairs in feedstock containing $3.1 \cdot 10^{17}$ and $3.4 \cdot 10^{17}$ cm^{-3} of boron and phosphorus respectively [11]. The complex state consists of an oxygen dimer, O_{2i}^{*}, and substitutional boron, and introduces a deep-level defect within the silicon band gap which will decrease the minority carrier lifetime. By annealing at temperatures above 200 ºC the meta-stable complex can be deactivated [52].

Three different approaches can be made to reduce the impact of the boron oxygen complex; i) Reducing the oxygen content, ii) substitute boron with other dopants, e.g. gallium or indium and iii) apply a high-temperature step in the solar cell processing. The latter of the three alternatives is applied in all the silicon industry today in the form of phosphorus diffusion, while reduction of total oxygen content is highly relevant research. [53]

3.7 Some common impurities in silicon

As stated in the beginning of this chapter, a more careful consideration of specific impurity elements relevant for this work are given below.

3.7.1 Iron

Iron is one of the most well known and studied impurities in silicon. More than 30 different iron complexes have been detected, however, with various dispersions and recombination activities. The two main iron species present in silicon, which also are the dominant recombinant complexes, are interstitial iron (Fe_i) and iron-boron pairs (Fe_iB_s, referred to as FeB from now on) [54]. Even though only about 1 % of the iron found in as-grown mc-silicon is present as an interstitial species, it has a substantial impact on minority carrier lifetime [36]. As illustrated in Figure 11, the energy levels introduced by Fe_i and FeB is located at E_v+0.38 eV and between E_c-0.23 and E_c-0.29 eV respectively [54], both being deep-defect levels.

Coletti *et al.* [55] showed a clear correlation between iron-doped silicon and reduction in lifetime. A p-type ingot doped with 53 ppmw of iron showed lifetimes of approximately 1-2 µs, while the reference (p-type, undoped) showed lifetimes of 50-75 µs.

Iron seems to be able to diffuse and precipitate at gettering sites (e.g. grain boundaries) quite easy, as observed by Istratov *et al.* [39]. If the minority carrier cross-section for such precipitates is smaller than the distance between the gettering sites, the

concentration of iron within grains can be drastically decreased, and hence the carrier diffusion length would be enhanced.

Iron is unlike chromium not as recombinant in n-type silicon as p-type. This is due to a much larger capture cross-section for electrons than holes. Hence, producing n-type material and creating the pn-junction by diffusing acceptors into the material, would have a substantial impact on iron's properties in silicon. In n-type silicon the quality of the material will not be influenced to the same extent by these interstitial point defects [25]. As-cut lifetimes in iron doped n-type material where reported by Coletti *et al.* [55] to be in the range of 6-20 µs, while p-type material doped with the same amount of iron showed lifetimes of only 1-2 µs. Some properties of iron in silicon is shown in Table 7.

Table 7: The properties of iron in silicon

Property	Value	Denotation	Ref
Segregation coefficient	$8.0 \cdot 10^{-6}$	-	[14]
Solid solubility (1325 ºC)	$3.0 \cdot 10^{16}$	atoms/cm^3	[14]
Diffusion coefficient	$0.62 \cdot \exp\left(-\frac{0.87}{k_B T}\right)$	cm^2/s	[49]

A more comprehensive review of iron's properties, complexes and impact on silicon and silicon devices are given by Istratov et al [54, 56].

3.7.2 Chromium

Chromium is an element commonly found in mc-silicon, but its influence and detrimental properties have not been given much attention compared to its near-neighbor in the periodic table, iron. Even though chromium concentrations in most mc-silicon materials are comparable to concentrations of iron, the latter element has been more thoroughly studied. Chromium is, however, also interesting to study more carefully both because of its resemblances and dissimilarities with iron and its influence on mc-silicon.

Iron, as well as nickel and aluminum, can be tolerated in higher concentrations in n-type material than p-type, i.e. the detrimental effect on the material is less on n-type than p-type. Asymmetric electron and hole capture cross-section is the reason for this and only shallow trap levels are introduced by these elements in n-type material [25]. Chromium, on the other hand, does not possess such a property having similar electron and hole capture cross-sections [57], represented in Table 8. Deep-level recombination centers originating from chromium in p-type material is present in n-type as well. Hence, both n-type and p-type material have a similar (low) tolerance for chromium concentrations present in the silicon.

Table 8: Location of the energy level introduced in the silicon band gap and electron capture cross-section (σ_e) and hole capture cross-section (σ_h) of interstitial chromium and chromium-boron pairs. The symmetry factor, k, is explained in another section. All data are collected at 300 K if not otherwise is stated.

	Energy level [eV]	σ_n [cm^2]	σ_p [cm^2]	$k = \sigma_n / \sigma_p$	Reference
Cr_i	E_C-0.23	$2.5x10^{-13}$	$1.25x10^{-13}$	2	[58]
CrB	E_V+0.27	$1.5x10^{-13}$	-	-	
Cr_i	E_C-0.24	$2x10^{-14}$	$4x10^{-15}$	5	[38] [a]
CrB	E_V+0.28	$5x10^{-15}$	$1x10^{-14}$	0.5	
CrB	-	-	$8.4x10^{-14}$ $1.0x10^{-14}$ (160 K)	-	[59] [60]

[a] No temperature dependence found

Chromium can either be found in a precipitated state or located at interstitial sites in the silicon lattice, which introduces two energy levels in the silicon band gap, one for the free interstitial atom (Cr_i) and one for the pair with boron (Cr_iB_s, referred to as CrB from now on). They are located at 0.23 eV below the conduction band (E_C-0.23) and 0.27 eV above the valence band (E_V+0.27) respectively [60]. This is illustrated in Figure 11.

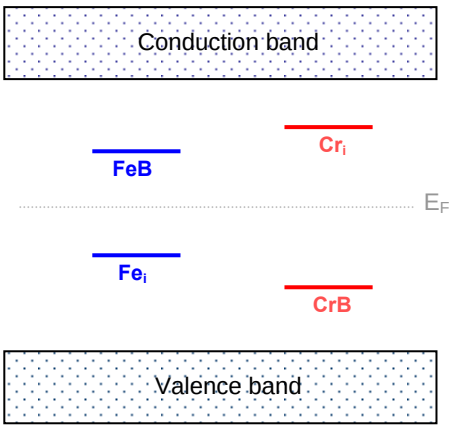

Figure 11: The energy levels introduced by interstitial chromium and iron as well as chromium-boron and iron-boron pairs. The Fermi level (E_F) in an intrinsic semiconductor has been included as well. It should be noted that the sketch is not represent able on a quantitative energy scale.

Bathey *et al.* [61] observed a decreasing trend in the electronic properties (V_{OC}, J_{SC} and power) when chromium was present in average concentrations above $3x10^{16}$ cm^{-3}. Schmidt *et al.* [62] computed that chromium concentrations above ~10^{12} cm^{-3} will be sufficient to reduce the lifetime of holes in n-type silicon. Due to the symmetric capture cross-section of chromium it can be assumed that the same results will be true for p-type material.

As for iron, Martinuzzi *et al.* [57] observed that chromium segregates well in mc-silicon and that it can be removed, or at least reduce the detrimental impact, by heterogeneous

precipitation and gettering. This indicates that even chromium has a detrimental effect on the properties of silicon; these effects are less pronounced (or even absent) in the complete solar cell. Gettering through phosphorus diffusion has been observed to be especially efficient towards iron and chromium due to a combination of two gettering mechanisms; relaxation and segregation gettering [50]. Details around these gettering mechanisms will not be given any further attention.

Some of the properties of chromium in silicon are given below in Table 9.

Table 9: The properties of chromium in silicon

Property	Value	Denotation	Ref
Segregation coefficient	$1.1 \cdot 10^{-5}$	-	[16]
Solid solubility (1200 ºC)	$1.0 \cdot 10^{14}$	atoms/cm^{-3}	
Diffusion	$1.0 \cdot \exp\left(\frac{-1.0 \pm 0.3}{k_B T}\right)$	cm^2/s	[63]

3.7.3 Chromium-boron and iron-boron pairs

Under thermal equilibrium interstitial chromium and boron will pair up entirely (assuming $[B_s] >> [Cr_i]$) [64]. Because of this the boron concentration is vital for the solid solubility of chromium in mc-silicon [44]. Chromium can also pair up with other acceptors than boron, including aluminum and gallium, as investigated by Ludwig and Woodbury [32].

FeB pairs are, like CrB pairs, present in mc-silicon and can be dissociated into interstitial iron and substitutional boron respectively, by standard illumination conditions (i.e. AM 1.5G, 0.1 Wcm^{-2}). The illumination creates free electrons and holes (minority carriers) which shifts the position of the quasi-Fermi level, as illustrated in Figure 12, to above the donor level introduced by the interstitial iron. The shift results in a neutrally charged iron atom that cannot pair up with boron due to lack of attractive Coulombic forces between the two elements [60].

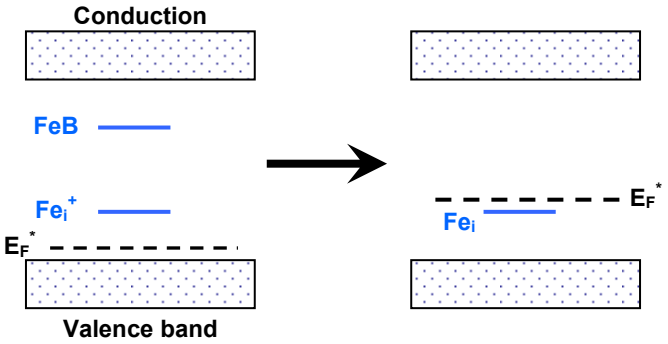

Figure 12: The shift in the quasi-Fermi level, E_F^*, in energy by illumination results in no pairing between interstitial iron and substitutional boron due to lack of Coulombic forces. Before the shift

the interstitial iron is positively charged, Fe_i^+. Notice that the acceptor level of boron is not included in the figure and that the figure is for illustration and is hence not correct with respect to energy.

Since the donor level corresponding to interstitial chromium is situated in the upper half of the silicon band gap the quasi-Fermi level does not gain enough energy (by free minority carriers) from illumination to be shifted above the donor level of interstitial chromium and hence discharge Cr^+ (interstitial specie). CrB pairs can, however, be dissociated into their respective charged atoms by heat treatment above 200 ºC. This will also dissociate the FeB pairs [60].

Both boron pairs will associate again with time after being dissociated. Several values for the time constant for the re-association (τ_{ass}) of CrB and FeB pairs have been suggested. Mishra [58] suggested that FeB pair re-associate 30 times faster than CrB in Cz-silicon (N_A=4x10^{14} cm^{-3}), while according to Istratov *et al.* [56] the time constant for CrB is one order of magnitude slower than FeB. Schmidt *et al.* [38] determined τ_{ass} for CrB to be 10 hours and attributed FeB pairs with a time constant of 10 minutes (N_A=1.2x10^{15} cm^{-3}). More recently Dubois *et al.* [59] established τ_{ass} of CrB and FeB pairs to 5.1x10^5 and 3.15x10^4 seconds respectively (N_A=8.0x10^{14} cm^{-3}).

However, Conzelmann *et al.* [60] arrived at the conclusion that re-association times are dependent upon boron concentration. The coupling in samples that contain high concentrations of boron, typically 10^{15} atoms/cm^3 or higher, saturated within a day, while it took several weeks for the pairs to completely re-associate the when only 2x10^{14} atoms/cm^3 (or lower) of boron was present.

The slower re-association of CrB pairs is due to the lower diffusivity of chromium in silicon. The impact of chromium on lifetime can consequently be separated from the effect of iron through measurements on complexes formed with boron. By measuring minority carrier lifetimes after illumination of a sample (FeB pair dissociation), then after heat treatment (both pairs dissociate) and comparing the results to a reference, the most recombination active centre can be determined. However, it must be assumed that the interaction of other elements is ignored and that the reduction in lifetime is only due to iron and chromium. [64]

In compensated material the high concentrations of boron and phosphorus can affect the extent of element-boron pairs due to annihilation of the dopants (reduction in free minority carriers) as well as a shift of the quasi-Fermi level towards mid-band gap. Such a shift will result in less affinity of electrons for boron atoms, hence a greater concentration of boron atoms remain neutral, and no Coulombic forces can attract positive charged transition elements. The recombination strength of element-boron pairs is consequently reduced. [65]

When considering the most interesting donor-acceptor pairs involved in this thesis, FeB and CrB pairs, the general case presented in the previous paragraph is more complex. Cr_i introduces a donor level in the upper half of the silicon band gap, while the Fermi level is always located in the lower half of the band gap in p-type material, which is the type used for almost all commercial solar cells today. Hence, interstitial chromium will remain

positively charged for all compensation levels in p-type material and CrB pair formation will always take place. On the other hand, the defect level introduced by interstitial iron is found in the lower half of the silicon band gap. Above a certain compensation level, where boron concentration is below 10^{14} cm^{-3}, iron cannot remain associated with boron [65]. Schmidt *et al.* claimed that the quasi-Fermi level will be located below the defect level introduced by interstitial chromium for boron concentrations not exceeding $4x10^{15}$ cm^{-3}. [38]

3.7.4 Crossover point

In the literature published on CrB pairs conflicting results have been presented concerning the most recombination active species of Cr_i and CrB. Similar controversy is reported in the literature concerning FeB pairs.

Excess carrier density, and hence lifetime curves for FeB pairs as well as its respective interstitial and substitutional species, have been demonstrated to be dependent upon injection level and to some extent doping concentration and temperature [66-68]. This provides an explanation for the diverse results presented in literature.

The donor level originating from the CrB pair is located between that of chromium and boron (E_v + 0.045 eV [5]), forming a deeper level than FeB and thus possessing greater recombination strength [60]. This is also confirmed by simulations computed by Dubois *et al.* [64]. For the CrB pairs a multiphonon recombination mechanism was suggested by Schmidt *et al.* [38] after investigations on the temperature dependency of the hole capture cross-section in n-type material.

By using Shockley-Read-Hall (SRH) theory in calculations, Schmidt *et al.* [38] furthermore computed that the most active recombination centre of Cr_i or CrB pairs depends upon the doping concentration of chromium and boron in p-type silicon.

The associated and dissociated state of element-boron pairs give individual lifetime curves with a distinct different injection level dependency. At a particular excess carrier density, Δn_{cr}, the lifetime remains constant before and after illumination, i.e. before and after dissociation of element-boron pairs. The specific point can be obtained by plotting lifetime as a function of the injection level, or alternatively the excess carrier density, when all element-boron pairs are associated as well as when dissociated. The point where the curves cross are referred to as the crossover point [67, 68]:

$$\tau_{associated} = \tau_{dissociated} \tag{3.1}$$

Tau, τ, is the lifetime of the respective associated and dissociated states. The origin of the crossover point is the variant nature of the excess carrier density with defect levels. Macdonald *et al.* defined the crossover point as the excess carrier density at which the charge carrier lifetime remains unchanged when transforming the chemical state of non-precipitated iron from FeB pairs to interstitial iron [66]. However, identical measurements can be applied to any defect that occur in two chemical states and which

shows crossover point behavior. Birkholz *et al.* [67] stated that the unpublished work of J. Schmidt and D. Macdonald even showed a crossover point for both iron-gallium and iron-indium pairs.

Examples of crossover points from recent publications [66, 67] are shown below in Figure 13.

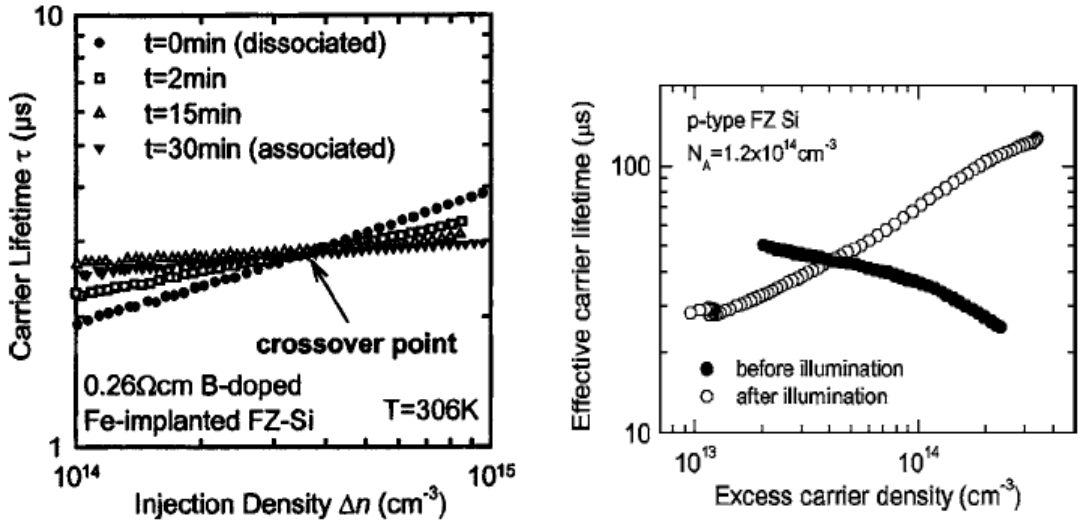

Figure 13: Examples of crossover points. Injection density or carrier density is plotted versus carrier lifetime before and after illumination [66, 67].

Such a plot will determine which of the states, the element-boron pair or the interstitial element, that show dominant recombination activity for a range of injection levels. Using the example to the right in Figure 13, the curve representing interstitial iron (after illumination) will be the dominant recombination state up to excess carrier densities corresponding to ~$3x10^{13}$ cm^{-3} (at the crossover point). Above this level iron-boron pairs will be most recombinant state and hence influence the lifetime to a greater extent.

Birkholz *et al.* [67] observed the temperature dependency of the crossover point, a shift towards higher injection densities with increasing temperature, as shown in Figure 14.

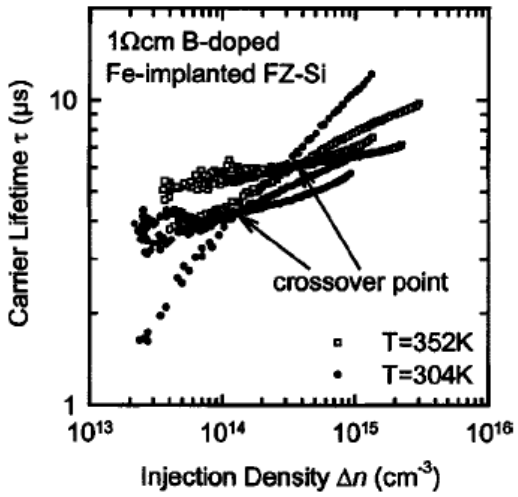

Figure 14: Temperature dependency of the crossover point, here illustrated by an intentionally iron contaminated samples [67]

3.7.5 Symmetry factor

The symmetry factor, k, is defined as [69]:

$$k \equiv \frac{\sigma_n}{\sigma_p} = \frac{\tau_{p0}}{\tau_{n0}} \tag{3.2}$$

The ratios of capture cross-sections of electrons (σ_n) to holes (σ_p) express the recombination activity for an impurity element in silicon. The symmetry factor can also be expressed as the ratio of the time constant for capturing holes (τ_{p0}) to electrons (τ_{n0}). For k = 1 the correlation is valid for both p- and n-type material. On the other hand, if the capture cross-sections possess an asymmetry, i.e. k≠1, the equation is only valid for p-type material [69].

The similar capture cross-sections of holes and electrons for the defect level of interstitial chromium are synonymous with electron and hole capture times, as stated in Equation 3.2. Thus, a symmetry factor closer to one means greater probability of trapping an electron and hole simultaneously, and hence also more recombinant. Interstitial chromium will therefore based on this criteria have greater recombination strength than iron. For interstitial iron there is a large difference in capture cross-section and the defect level is more like an electron trap rather than recombination center.

Comparing the two defect levels introduced by chromium species, interstitial chromium should be the most recombination active of the two due to the defect level being located closer to mid-band gap than for chromium-boron. Furthermore, the symmetry factor k is almost the same and hence doesn't constitute a significant factor when considering the most recombination active center.

3.7.6 Aluminum

Aluminum is a slow diffuser in silicon compared to many of the transition elements and is most likely introduced through feedstock material rather than by diffusion during processing [70]. Due to its considerably lower diffusivity it is not easily removed from the bulk by gettering [26]. Interstitial aluminum, like boron, introduces a shallow acceptor energy level at 0.057 eV above the valence band. Aluminum furthermore behaves similarly to boron by the formation of complexes with transition metals, as well as with oxygen if sufficiently high concentrations are present. Al-O complexes are highly recombinant due to the introduction of a deep level defect.

Rodot *et al.* [71] reported that aluminum creates recombination centers at concentrations $>10^{15}$ atoms/cm^3. A large decrease in carrier diffusion length was observed when concentrations exceeded this and Rodot *et al.* [71] attributed the recombination centre to Al-O complexes rather than the interstitial aluminum atom. The same was concluded by Rosenits *et al.* [70], which located the deep level defect at 0.44±0.02 eV, as defect levels corresponding to aluminum-vacancy and aluminum-iron complexes are located elsewhere in the silicon band gap. The capture cross-section for electrons and holes of the recombination center, $\sigma_n = 3.1\text{x}10^{-10}$ cm^2 and $\sigma_p = 3.6\text{x}10^{-13}$ cm^2 respectively, exhibits a typical asymmetry like many other impurities.

3.7.7 Titanium

Titanium introduces two defect levels in the silicon band gap at E_c-0.24 eV and at E_c-0.49 eV respectively, with a symmetry factor, *k*, of 7650 for the former and 25±12 for the latter defect level. Consequently, the defect level located 0.24 eV below the conduction band is the strongest recombination centre of the two. [72]

Rohatgi *et al.* investigated additions of titanium, iron and copper separately in boron doped Cz-silicon. A concentration only exceeding $3\cdot10^{11}$ cm^{-3} resulted in loss of solar cell efficiency, as is shown in Figure 15 [73]. This agrees well with what Davis *et al.* [4] reported the same year. Further investigations indicated that the loss of performance was due to a decrease in bulk lifetime, concentrations not being high enough to influence the shunt or series resistance [73].

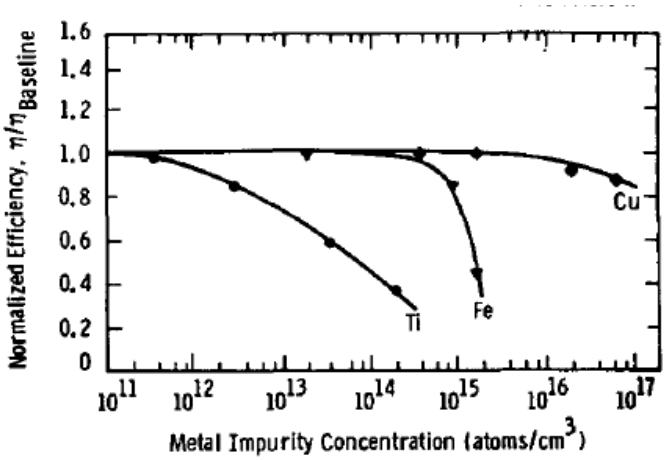

Figure 15: Metal impurity concentration of titanium, iron and copper plotted versus the normalized efficiency, i.e. the efficiency with respect to a baseline efficiency of a cell with no added impurity processed identical as the doped cells [73]

Investigations by Buonassisi *et al.* [74] resulted in no detection of titanium precipitates by μ-XRF in float zone silicon doped with $5 \cdot 10^{13}$ cm^{-3}. However, great recombination activity was observed at the grain boundaries and defects indicating the presence of titanium.

The slow diffusing properties of titanium distinguish this impurity from chromium, iron and other interstitial fast diffusers. Larger fractions of titanium will remain dissolved in silicon and will not form complexes with donors due to their immobility. Titanium degrades the electrical properties of silicon at such low concentrations because of the ineffective gettering at temperatures and times typically applied commercially. [74]

4 Characterization Techniques

The work of this master thesis has included several characterization techniques in order to investigate the material properties from as-cast to solar cells. This chapter will focus on the basic principles for several of the techniques applied, while more practical issues are considered later in the experimental Section.

4.1 GDMS – Glow Discharge Mass Spectroscopy

The GDMS instrument can detect trace elements at parts per billion (ppb) levels. A potential difference is applied between two electrodes incorporated in an argon atmosphere. The sample functioning as a cathode is sputtered with argon ions as they are accelerated towards the sample and release atoms from the cathode as well as secondary electrons. The sample atoms move towards the plasma where they collide with electrons or argon atoms/ions and hence are ionized. Lenses focus and accelerate the ionized sample atoms into the detector consisting of a mass analyzer separating the atoms according to the mass-charge ratio [75]. An illustration of the instrument can be seen in Figure 16 [76].

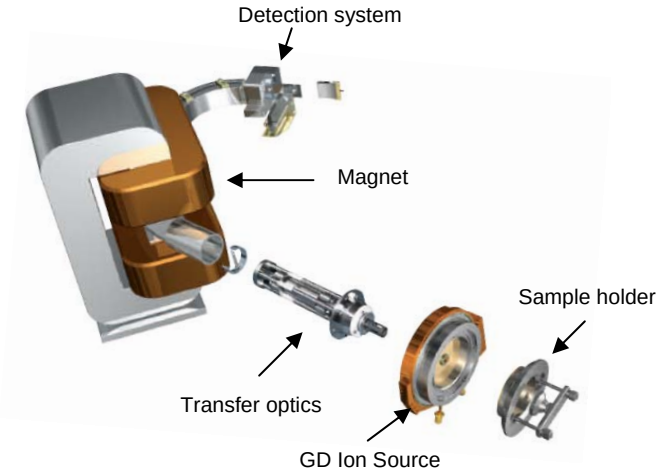

Figure 16: An illustration of the GDMS instrument [76]

4.2 FTIR – Fourier Transform Infrared Spectroscopy

FTIR detects the concentration of substitutional carbon and interstitial oxygen in silicon. When a sample is exposed to infrared light the chemical bonds will absorb the light through vibrations. The vibrations are characteristic for the atoms making up the bonds and the amount of light absorbed at a certain wavelength is recorded. A typical spectrum is shown in Figure 17, and the concentrations of atoms forming the chemical bonds are calculated from this absorbance spectrum. Interstitial oxygen has a characteristic

absorption peak at a wave number of 1107 cm^{-1} while substitutional carbon absorption occurs at 605 cm^{-1}. Silicon is transparent to light at these wavelengths and will not absorb significant amounts of the IR-radiation. [25]

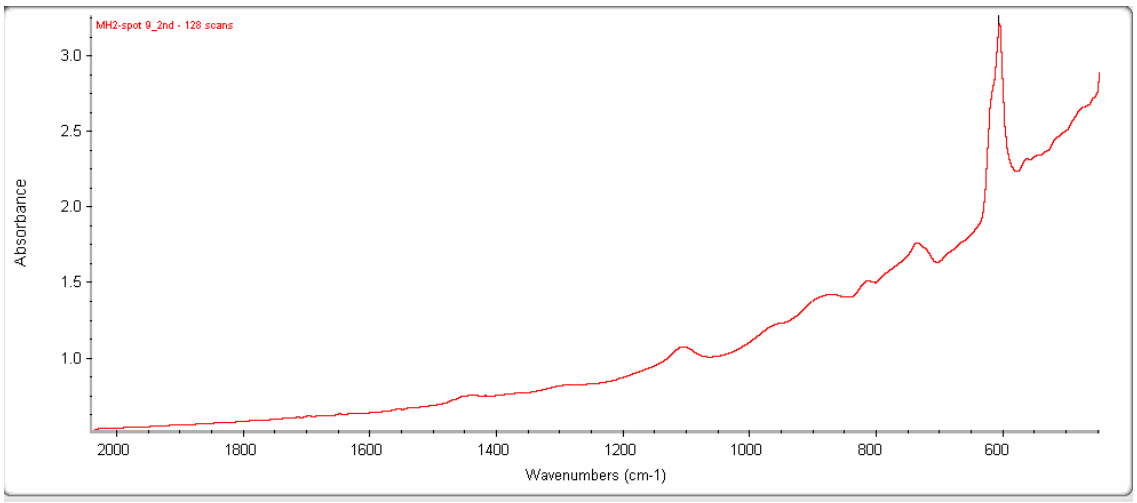

Figure 17: Oxygen and carbon absorption peak at 1107 and 605 cm^{-1}, respectively, obtained by FTIR measurements

4.3 EBSD – Electron Backscattering Diffraction

EBSD is a technique used to determine grain orientations, hence also grain- and twin boundaries, in the material. The instrument consists in brief outline of a scanning electron microscope (SEM) that is used to position the sample, a beam source and a phosphor detection screen. A sketch of the instrument is given in Figure 18 [77].

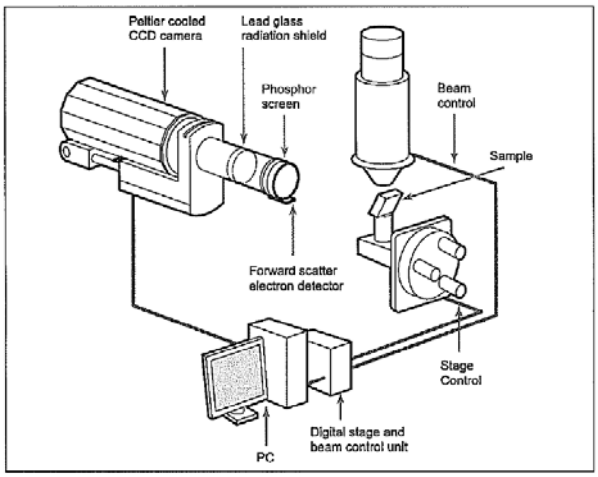

Figure 18: A sketch of the EBSD instrument including the most important characteristics [77].

When the electron beam scans the sample the electrons are scattered. The electrons that are incident on atomic planes at an angle that satisfy the Bragg equation [78] will form a diffraction pattern. The principle is shown in Figure 19. Electron backscatter patterns are

formed on the phosphor screen by activation of fluorescence. The diffraction pattern is characteristic of the crystal orientation. [77]

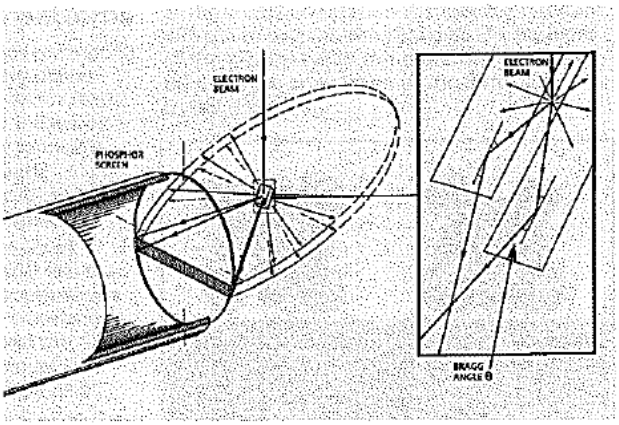

Figure 19: The principles behind the EBSD measurements: how electrons are scattered and create a diffraction pattern and how it is detected on the phosphor screen [77]

4.4 μW-PCD – Microwave Photo Conductance Decay

μW-PCD allows mapping of minority carrier lifetime across a sample. Illumination generates excess carriers which will increase the conductivity for a short period of time. Consequently the microwave reflectivity of the sample also changes and this alteration is detected by a microwave antenna that also emits microwaves. The excess carrier density, which minority carrier lifetime can be extracted from, is proportional to the microwave signal.

The recombination process is dominated by recombination of excess carriers at the surface as well as in the bulk. The measured lifetime, τ_{eff}, is thus a function of the bulk lifetime, τ_b, and at the same time strongly influenced by the surface recombination rate. To separate the two contributing factors are difficult.

However, by passivating the surface of the sample, surface recombination effects are reduced to a minimum and the effective lifetime measured should be dominated by the bulk lifetime, τ_b [22, 79].

μW-PCD can also estimate the concentration of interstitial iron by using the principle of iron-boron pairing. Lifetime is measured before and after illumination and the concentration of iron can be calculated according to the following equation [64]:

$$[Fe_i] = C_{Fe}\left(\frac{1}{\tau_{Fe}} - \frac{1}{\tau_{dark}}\right) \tag{4.1}$$

C_{Fe} is a constant depending on the recombination properties of iron.

4.5 PVScan – Physical Volume Scan

The optical scanning system of a PVScan map crystal defects including dislocation density, stacking faults and grain boundaries on polished and etched wafers. Grain boundaries penetrating the surface of etched wafers will form a v-shaped groove which scatter light with a low angle, hence light are reflected as a line almost perpendicular to the grain boundary. Dislocations scatter light off the circular etch pits as narrow cones, and an integrated sphere detector will detect the diffuse reflected light. Both types of reflections are illustrated in Figure 20 [80].

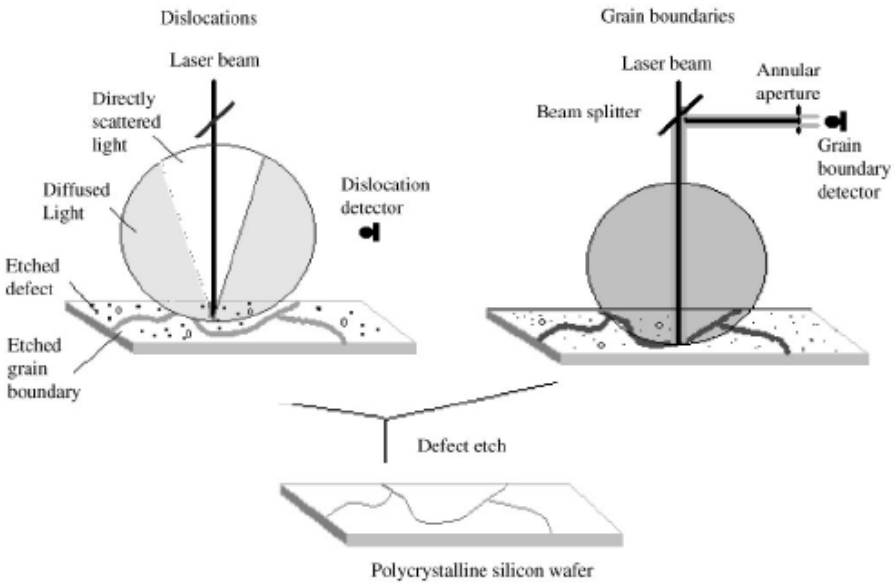

Figure 20: Reflection of light from dislocations, left, and grain boundaries, right, of etched wafers during PV-Scan measurements [80].

Two different systems ensure the simultaneous detection and separation between maps of grain boundaries and dislocations. The integrated scattered light is used to count defects. A dislocation free area will reflect all the light straight back and be registered as background. [22, 25]

Thermal stresses that arise during crystal growth are reflected in the distribution of defects in the material. Low dislocation densities of wafers match an average of $\leq 10^5$ cm^{-2}, as defined by Sopori *et al.* [80] and suggested by Ryningen. [22] Dislocation clusters and areas with high dislocation density are typically $\geq 10^6$ cm^{-2} [48].

4.6 Resistivity

Resistivity of semiconductors can be measured by a four-point probe where the two outer tips or needles apply a current (500μA) to the sample, while the two inner needles function as a voltmeter measuring the voltage between the two probes. The resistivity can

then be computed directly from the voltage and current. The four tips are equally spaced and total probe spacing is typically 0.635 mm, an illustration is shown in Figure 21.

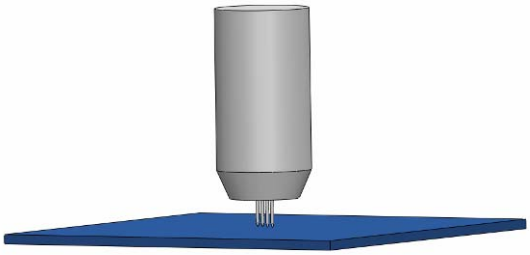

Figure 21: The resistivity instrument consisting of four probes equally spaced

Resistivity measurements reflect the concentration of doping elements (boron and phosphorus) present in silicon. For p-type silicon the boron content can be calculated from the following equation given by ASTM standard F 723-99 [81]:

$$N_B = \frac{1.330 \cdot 10^{16}}{\rho} + \frac{1.082 \cdot 10^{17}}{\rho[1 + (54.56\rho)^{1.105}]} \tag{4.2}$$

Where ρ is the resistance measured. The resistance will decrease when approaching the top of the ingot due to accumulation of dopants in the liquid phase during solidification. A higher concentration of dopants will consequently increase the conductivity of the material.

4.7 QSSPC – Quasi Steady State Photo Conductance

The QSSPC characterization of minority carrier lifetime is based upon the steady-state illumination, an alternative to the transient method exploited in for instance μw-PCD. When silicon is illuminated, excess carriers are generated which results in an increase in wafer conductance. The steady-state conditions must balance the generation and recombination of electron and hole pairs, here given by current densities [82]:

$$J_{photogeneration} = J_{recombination} \tag{4.3}$$

The quasi-steady-state technique diverges from a true steady-state illumination in that it employs a light pulse with a very slow variation compared to the effective lifetimes and long and exponential decay. The technique is non-destructive and can be applied to wafers, bulk samples and solar cells stripped for metal contacts. [82]

The instrument consists of a light flash and a conductivity coil where the coil is in contact with the sample quantifying the excess photoconductivity. The effective minority carrier lifetime can be expressed in terms of the the total recombination, $J_{recombination}$, and the excess photoconductance, $\Delta\sigma_L$ [25]:

$$\tau_{eff} = \frac{\Delta\sigma_L}{J_{recomb.}(\mu_e + \mu_h)} \tag{4.4}$$

μ_e and μ_h is the mobility of electrons and holes, respectively.

A large range of lifetimes, nano seconds to milli seconds, can be measured, only limited by the signal strength. At low injection levels significant effects from trapping can give excessively high lifetimes, and such measurements should be ignored. Within 60 micro seconds lifetime, the error is less than 1 %, increasing to 10 % when the lifetime exceeds 230 micro seconds. [82]

4.8 CDI – Carrier Density Imaging

CDI is a fast mapping technique with high spatial resolution. The carrier density imaging is based on the absorption and emission of IR-radiation (photons with lower energy than the band gap) by free carriers.

An illumination source and a source emitting IR-radiation are included in the set-up, a sketch is shown below in Figure 22.

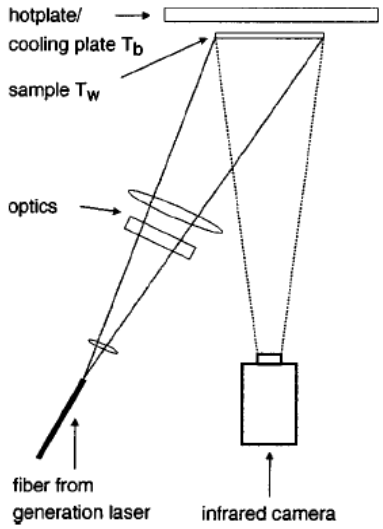

Figure 22: The CDI instrument set-up including a hotplate where samples is placed, a semiconductor laser and s CCD camera [83]

The illumination source consists of a semiconductor laser emitting light with higher energy than the band gap. Generation of additional free carriers by the laser will increase the absorption and emission of IR-radiation by transitions within the conduction or valence band. A CCD (charge coupled device) camera detects the transmitted IR-radiation from the sample. The transmissitivity of the wafer is measured during illumination with the laser as well as without. Subtraction of the two images obtained

indicates the IR-absorption of the free carriers. The difference can be exploited to calculate the induced excess free carriers. [83, 84]

The instrument can operate with two different operation modes; absorption or emission. The same amount of power which is absorbed must also be emitted for the material to remain the same temperature. [83]

4.9 EBIC – Electron Beam Induced Current

EBIC imaging is performed in a Scanning Electron Microscope (SEM). The principle of this characterization technique is the generation of charge carriers by an electron beam striking a sample. The free carriers move according to an electric field yielding a detectable current. The applied electric field is supplied by a pn-junction or Schottky contact, or it can be an externally electric field generating electron-hole pairs. The electrons from the electron beam experience internal scattering in the material. Small loss of energy and large angular deviation from their trajectory results in low energy secondary electrons and holes to be left behind the scattered electrons. The carrier generation in the material has the shape of a droplet and is normalized for all materials through a constant called the Grün length (R_e). An illustration is shown below in Figure 23. [85]

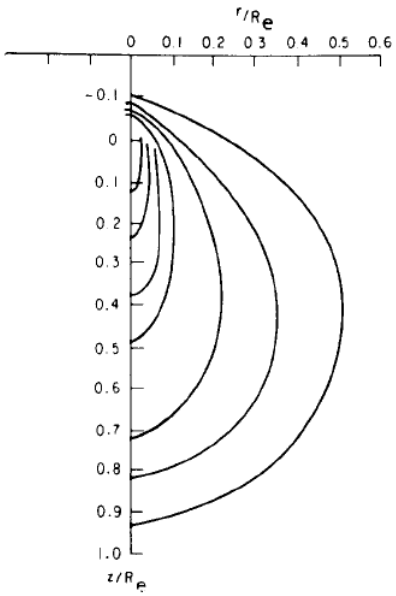

Figure 23: Illustration of how and where charge collection takes place during EBIC imaging [85]

The current that is collected from the charge carriers, I_{CC}, during a two-dimensional scan is used to create images, here referred to as EBIC images. The two-dimensional image is achieved by moving the beam across the sample. [85]

EBIC images reflect the material characteristics of a semiconductor by differentiating electrical activity. Crystallographic defects, grain boundaries and precipitates, for

instance, will reduce the lifetime or diffusion length of the charge carriers. This will appear as a reduction of I_{CC} in the EBIC image, in other words as darker contrast compared to areas of less recombination. [85]

4.10 Auger spectroscopy

Auger spectroscopy is based on the Auger effect involving three electrons. The Auger process is initiated by an electron making a transition from a core state to a higher level, leaving the atom in an excited state. This process must be stimulated from an external radiation source or equivalent. The electron leaves a hole which an electron from an outer shell relaxes to, transferring the excess energy to another outer shell electron. The latter electron will be an Auger electron emitted with a kinetic energy that is determined by the energy difference between the excited and relaxed states, and is independent of the original excitation radiation [86]. An illustration of the principle is shown in Figure 4.

Due to small mean free paths of inelastic electrons in the range of kinetic energy exploited, electrons collected in Auger spectroscopy originate from the near surface. The principle of electron-matter interaction forms a droplet shape; an illustration is given in Figure 24. The emitted Auger electrons are analyzed in terms of their kinetic energy, and the Auger spectrum contains the number of counts per unit time versus kinetic energy. Peaks descended from different elements can be discriminated according to an overview of already established peaks of elements. By ion bombardment (sputtering) intermittenly with recording Auger spectrum a depth profile of the sample can be achieved. [86]

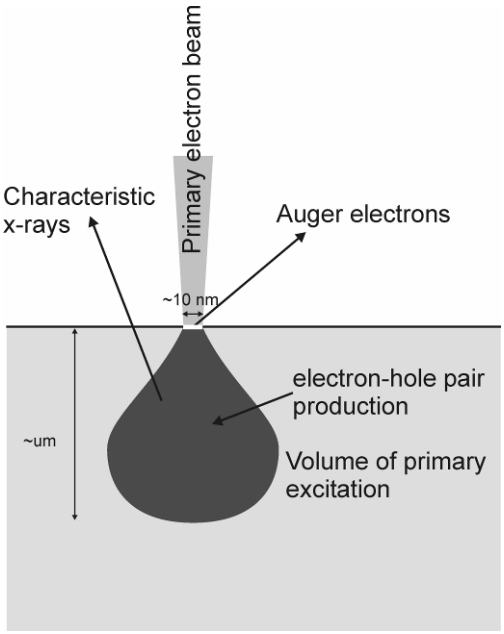

Figure 24: The interaction between electrons and material creating Auger electrons characterizing the elements present in the material [86]

5 Experimental Work

The casting process for the ingot, together with an outline for cutting and wafering, are presented in this chapter. Preparation of samples or wafers, including grinding, polishing and etching, are also described with the samples selection for the various characterization techniques as well as some practical details about the analyses. At last, a brief presentation of the solar cell process is given.

5.1 Casting

Two 12 kg ingots were cast in a pilot-scale induction furnace Crystalox DS 250 [87], in the Department of Materials Science and Engineering at NTNU. A sketch of the furnace is shown in Figure 25. The furnace produces ingots of 250 mm in diameter and approximately 100 mm in height. The planar solid-liquid solidification front is controlled by extracting heat vertically through a water-cooled variable heat leak (VHL), as shown in Figure 26, located underneath the crucible.

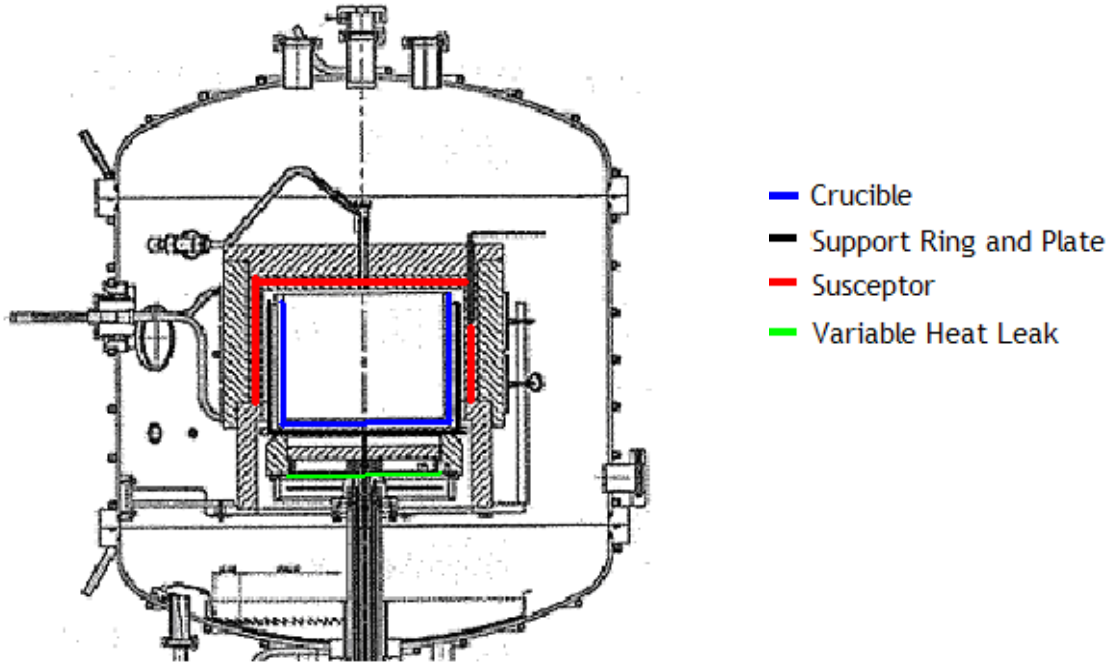

Figure 25: A cross-section of the Crystalox DS 250 furnace used in the casting [87]

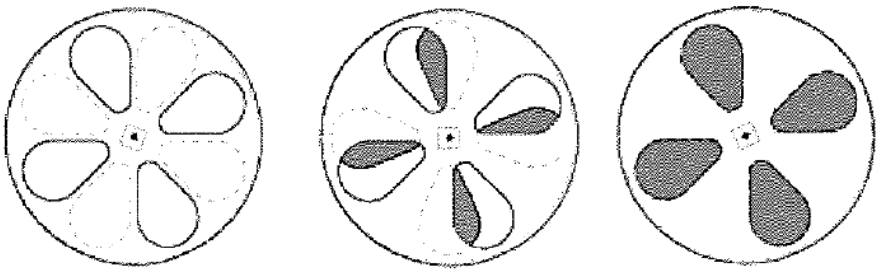

Figure 26: VHL (variable heat leak) cooling system in the furnace. The stippled lines indicated the "sluice" on the lower disk, while solid line indicated the top disk. Sketch illustrates the progress from closed (left) through partly open (middle) to completely open (right) heat leak [47].

A standard silicon dioxide crucible from Vesuvius and silicon nitride coating from H.C. Starck (first ingot) and UBE (second ingot) was used in the casting with Elkem Solar Silicon® (ESS™) feedstock as received by Elkem. The coating composition is presented in Table 10, while Table 11 gives an overview of the concentration of several impurity elements present in crucible, coating (H.C. Starck) and feedstock, respectively. Note that concentrations cannot be given as product specifications.

Table 10: Composition of the coating used on the crucible

Component	Amount [gram]	Function
Si_3N_4	100 gram	Matrix
De-ionized water	150 [a]	Solvent
Optapix	5 gram	Binder
Darvan	2 gram	De-foamer

[a] ml

Table 11: Concentrations of various impurity elements present in the crucible, coating and feedstock. Note that concentrations given cannot be used as product specification.

Element	Crucible [ppmw]	Coating [ppmw]	Feedstock analysis (as given by ES [a]) [ppmw]
B	-	1.7	0.46
O	< 0.15 % (As Al_2O_3)	12000	n.a.
Fe	30	13	< 2
Cr	-	0.66	< 0.5
Ti	10	0.72	< 0.2
Al	700	0.66	< 0.4

[a] by ICP-MS

Two identical castings, MH1 (initial charge weight =12.018 kg) and MH2 (initial charge weight = 12.000 kg), were made. Pure metallic chromium (99.999 %) was added to the

middle of the silicon charge, approximately after ¾ of stacking of feed material, in both MH1 (0.5948 gram) and MH2 (0.5965 gram). The concentration of chromium added to both ingots corresponded to 50 ppmw. The amount of doping was chosen based on the segregation behavior, and hence the equilibrium segregation coefficient, the detection limit of the GDMS instrument and former experience with doping same size ingots with iron [25].

Figure 27 shows a typical susceptor temperature profile used in the casting processes. No crucible rotation was used during the casting of MH1 due to broken parts in the rotation component, while in MH2 rotation was applied.

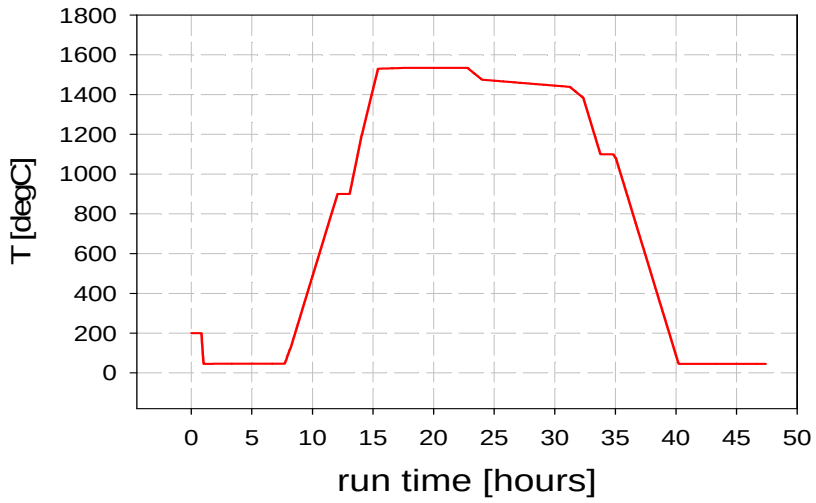

Figure 27: The susceptor set point temperature used for the castings

5.2 Cutting and Wafering

The complete ingots were cut according to Figure 28. The blocks (Q1, Q2, Q3, and Q4) are approximately 50x50x100 mm^3 each, and slice D, E, AB and BC are vertical cross-section cuts through the ingot. Block Q2 was horizontally cut into smaller samples, while block Q1 and Q3 was sent for wafering at Fraunhofer Institut Solar Energiesysteme (ISE in Germany). Wafering was performed using a multi wire slurry saw, cutting 250 µm thick wafers. The wafers were laser coded from bottom, starting at 1, to top, ending at 225-235 depending on ingot height.

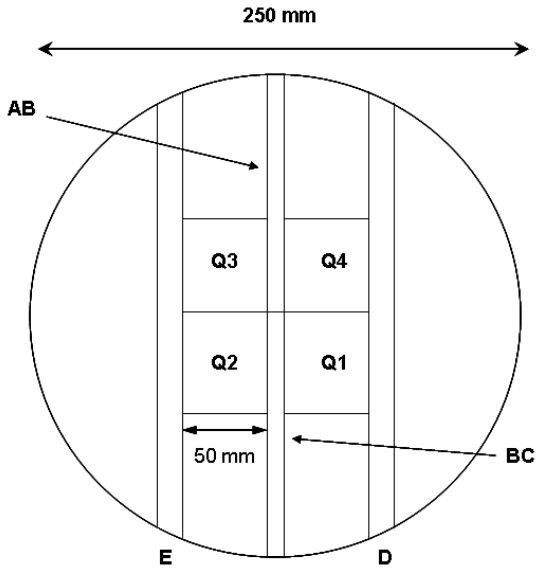

Figure 28: Outline of cutting plan for the cast ingot

Table 12 gives an overview of the parts of the ingots that were employed in the different characterization techniques as well as what sample preparation that were performed.

Table 12: An overview of which pieces of the ingot that were used for different characterizations

Sample	Characterization	Details	Sample preparation
Q1 (wafers)	Solar cell processing	Efficiency (η) Short circuit current (J_{SC}) Open circuit voltage (V_{OC})	Standard process
Q2	Resistivity GDMS	Conductivity Elemental analysis	Grinding
Q3 (wafers)	EBSD PV-Scan CDI EBIC/Auger	Grain orientation Dislocation density Minority Carrier Mapping Precipitation investigation	Polishing Polishing and Etching Etching and Passivation Polishing and Metal contacts
Q4	QSSPC	Minority Carrier Lifetime	Grinding
Slice E	μw-PCD ICP-MS/LECO	Minority Carrier Mapping Elemental analysis	Passivation -
Slice ABC	FTIR	C_s and O_i	Polishing

5.3 Sample preparation

The sample preparation techniques performed before characterization, are described in the following section.

5.3.1 Grinding

All samples characterized by GDMS and resistivity measurements were ground with 80, 320 and 500 grit SiC paper, while the block for QSSPC was ground with SiC paper down to 1200 grit to ensure a smooth surface.

5.3.2 Polishing

Mechanical polishing is necessary to remove further surface roughness. Samples were glued onto a circular steel disc with wax by heating the disc, remove it from the plate, and place the sample on the hot plate until reaching temperatures where the wax melts. A thin layer of wax is applied onto one side of the sample and then removed from the heat placing the warm disc on top, left to cool down.

A Pedemax-2 polishing instrument is used with polishing cloth, ethanol and spray containing diamond abrasives, conducting separate steps for each abrasive size; 9, 3 and 1 μm. The steps conducted for each abrasive size are as follows:

- Cloth is wetted with ethanol and diamond spray
- The disc with sample is mounted to the instrument
- The disc and polishing cloth are rotated counter-clockwise at a speed of approximately 300 rpm
- The cloth is wetted every 20th second with ethanol
- More diamond spray is applied after 1 ½ minute
- Total polishing time is 3 minutes
- Sample are cleaned in cold water and ethanol

A last step of chemical-mechanical polishing removed oxides from the surface. The same setup as in mechanical polishing was used. De-ionized water and Nalco 2350 slurry pre-mixed with water (1:7 slurry : de-ionized water) are dripped onto a pad for exactly 1 minute while polishing before washing with de-ionized water for 1 minute.

Samples are dismounted from the sample holder by exposing it to hot water, melting the wax. Then the samples are thoroughly washed with water and ethanol.

5.3.3 Etching

Wafers must, in addition to polishing, also be etched prior to PV-Scan characterization in order to reveal dislocations and grain boundaries as etch pits and v-shaped grooves, respectively. Etching will also remove saw damage from the wafering process.

Prior to etching, insoluble organic contaminations as well as the silicon dioxide film are removed from the surface in a two-step process as presented in Table 13, the third step being the actual etching.

Table 13: Steps for etching silicon samples

Step	Component	Composition	Time	Temperature
1	RCA Organic clean	$H_2O : H_2O_2 : NH_4OH$ 5 : 1 : 1	10 minutes	75 ºC
2	HF	5 % HF acid	3 minutes	25 ºC
3	Sopori [88]	$HF : CH_3COOH : HNO_3$ 36 : 15 : 2	25 seconds	25 ºC

After etching, step 1 (RCA) is repeated once more to remove organic residues. Between each step (except between 2 and 3) the wafers are rinsed in de-ionized water and cleaned in ethanol.

Wafers used for FeB and CrB characterization at Institute for Energy Technology (IFE in Oslo) were etched with CP5 etch prior to the passivation process given in the next section. Approximately 10 µm were etched away with CP5 etch according to the steps described in Table 14. Between each step the wafers are rinsed in de-ionized water.

Table 14: Details of the etching process performed at IFE

Step	Composition	Time
1	$HNO_3 : CH_3COOH : HF$ 10 : 5 : 2	70 seconds
2	5 % HF	3 minutes
3	$H_2SO_4 : H_2O_2$ 4 : 1	8 minutes
4	5 % HF	1 minute

5.3.4 Passivation process

After a CP5 etch the wafers for FeB and CrB pair characterization and gettering experiments must be passivated chemically. The passivation process reduces the surface

recombination to a minimum by terminating dangling and defective bonds at the surface of the wafers. The passivation, that was carried out at IFE, deposited a thin film of hydrogenated amorphous silicon (α-Si:H) with a Plasma Enhanced Chemical Vapor Deposition (PECVD) technique. The plasma operated in 720 seconds in total at a deposition rate of 6 nm/minute. The chamber temperature was 230 ºC.

Wafers passivated at Fraunhofer ISE are subjected to a CP133 etch and HF dip prior to the passivation process. Then a standard passivation layer of silicon nitride was applied to the wafers by the PECVD technique, like the process described above.

5.4 Characterization

Chapter 4 gives an overview of the principles of all the characterization techniques employed. This section, however, aims to describe some of the practical conditions and settings used specifically for the experiments conducted in this thesis.

5.4.1 EBSD

A Zeiss Supra 55 VP instrument was used for recording the grain orientation maps of wafers. There are two modes of scanning. In the first alternative a stationary electron beam scans the sample by moving the sample holder. The second mode operates by moving the beam while the sample is stationary. Due to the size of the scanning area (50x50 mm^2 wafer), the mode of scanning consisted of a combination between both stage and beam scan. Hence, the beam scans a small square area of about 100x100 µm, commonly referred to as the step size, while the stage with the sample holder is then moved in order to be able to scan the next square.

The sample should be tilted 70º in the measurement chamber for an optimal angle in proportion to the electron beam and detector location. However, due to the design of the chamber the stage can only be tilted to 65º. This is also the case for the working distance.

The measurements are performed with an accelerating voltage of 20 kV and a working distance of 38 mm.

5.4.2 PVScan

The mapping of dislocation density is done by a PVScan 6000 instrument from GT Solar. A stationary Helium-Neon (690 nm) laser scans the sample by moving the stage with the sample. Prior to the measurements the instrument is calibrated by measuring a small area of a standard multicrystalline wafer with known dislocation density. For 50x50 mm^2 wafers 1000 lines are scanned, which corresponds to a resolution of 50 µm.

The software is not able to discriminate twin boundaries, stains, scratches and etc. from defects in the sample and will interpret this as dislocation clusters. However, in most

cases it is possible to separate real dislocations from these effects by eye. An example of PVScan analysis is shown in Figure 29.

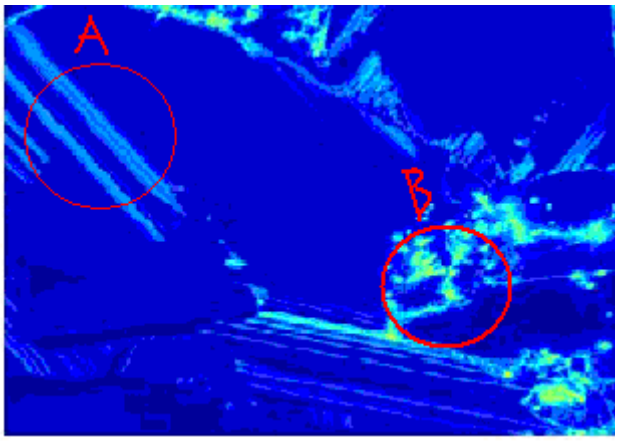

Figure 29: PV-Scan measurements of a wafer. Region A shows twin boundaries while area B is dislocation clusters. Of the two, only the dislocation clusters act as a recombination centre.

5.4.3 GDMS

When measuring the concentration of trace elements with a Finnigan Element GD from Thermo Fisher (Germany), the sample surface is pre-sputtered for approximately 10 minutes to eliminate surface contamination. Three parallel analyses are done on each measured spot, although only the last parallel is considered due to residual ions that can be left in the chamber from previous samples influencing the first two parallels.

Three different detection modes are available, namely Counting, Analog and Faraday. First the background spectrum is recorded, which will be extracted from the element spectrum later. Three resolutions are available, namely low (< 4000 counts), medium (4000-6000 counts) and high (> 6000 counts). In all measurements medium resolution was applied. The intensity of the mass peaks is measured in counts per second. [75]

The element concentration in ppbw is calculated by taking into consideration the number of counts, the isotope abundance and RSF (relative sensitivity factor, which is a correction factor). The equation is given below:

$$ppbwt = 10^9 \cdot \frac{\frac{Intensity(El)}{Abundance(El)}}{\frac{Intensity(Si)}{Abundance(Si)}} \cdot RSF \tag{5.1}$$

El refers to the element that is measured.

There has not been done enough statistical work in order to comment on the exact detection limits of the GDMS instrument.

5.4.4 FTIR

The interstitial oxygen and substitutional carbon are detected by a Nicolet 6700 FTIR instrument from Thermo Fisher. The measurements are corrected for H_2O, CO_2 and multiple reflection correction (MRC). Since the software assumes that the laser does not reflect within the sample such a correction is applied to account for the internal scatterings that occur. A resolution of 8 cm^{-1} is applied. [89]

The background is first recorded. Then the peaks can be collected from the absorbance of the laser due to vibration of the bonds. The absorbance for oxygen is converted to concentration (in ppma) by applying equation:

$$[O_i] = 6.28\alpha_O \tag{5.3}$$

Where α_o is defined as:

$$\alpha_O = \frac{-\left(\frac{\ln I}{\ln I_0}\right)}{d} \tag{5.4}$$

The thickness of the sample, d, is also measured by the laser. I_0 and Iare the intensity of the incident light (laser) and after passing through the sample, respectively.

5.4.5 μw-PCD

A Semilab WT-2000 μw-PCD instrument record lifetime maps of silicon samples. The laser beam used for generating carriers is approximately 1 mm in diameter providing a resolution of 500 μm. Each single point measured, which together makes up the image, is an average of 16 measurements. The injection level applied has not been exactly derermined, but is in the low range region.

5.4.6 Effective segregation coefficient

The effective segregation coefficient is calculated by the least squares method. The GDMS concentrations measured as a function of height and the expected concentration calculated from Scheil's equation are taken into account. The square of the difference between measured and calculated concentrations are added up for all heights. Then the "solver" function in ©Microsoft Office Excel 2003 is applied. By changing k_0 the closest approximation to the value of the squared sums are found. The value with closest approximation corresponds to a value of k which is then the effective segregation coefficient. For more details see Appendix A.

5.4.7 EBIC

Measurements were conducted with a GATAN Digiscan 2 EBIC instrument at room temperature. The voltage and current were individually changed to focus and reveal particles at different depths. Section 6.11.1 explains this in more detail. Resolution was 1 kV.

The samples were equipped with ohmic contacts covering the backside, and several Schottky contacts of approximately 6 mm^2 on the frontside. The ohmic contacts were prepared by evaporating 200 nm of Al and subsequent annealing at 500 ºC, while the Schottky contacts were made by evaporating 20 nm of either Al or Ti. Electrical connection to the sample was made by gluing gold wires with silver paste to the top contact, while the back contact was pressed towards an aluminum foil.

5.4.8 Auger spectroscopy

Particles located by EBIC were analyzed with a JEOL Jamp-9500F Field Emission Auger Microprobe instrument at room temperature. For the depth profiling, a Ar ion beam energy of 2000 eV, removing ~16.7 nm/min was applied. It was scanned for the following elements: B, Ca, O, Cr, Fe, Ti, Al and Si. Between each scan 1 minute of sputtering was applied. The measurements provide a plot of counts per second (CPS) as a function of kinetic energy. Each scan is repeated 4 times for every pre-set peak/kinetic energy. Peaks can be identified as specific elements by comparison with charts defined previously.

5.4.9 CDI

The lifetime mapping is performed with a CDI instrument. A cell size of 42x42 mm^2 was applied for the measurements. The wafers are heated up to 60 ºC on a hot plate. The instrument is operating with an integration time of 1600 µs and 10 000 measurement periods are conducted. For each period an image with the laser on and an image with the laser off are obtained.

The presetting also includes correction for non-uniformity, resistivity and wafer thickness.

5.5 Gettering experiments

Phosphorus gettering of wafers from 50, 85, 90 and 95 % height in MH2 was performed at IFE. Gettering is a standard applied process to wafers, however, this gettering was adapted to the gettering of chromium and the specific details are given below. Prior to gettering the wafers were passivated according to the process given in Section 5.3.4.

- Etching of the passivated wafers in a 5 % HF solution
- Liquid diffusion source was sprayed on both sides of the wafers
- The solvent was removed by evaporation at 200 ºC
- Phosphorus diffusion at 890 ºC for 19 minutes
- Lower temperature gettering going from 800 to 700 ºC
- The phosphorus rich layer was etched away with CP5 and Piranha etch and passivated again, the same process as given in Section 5.3.4.

5.6 Processing of solar cells

The processing of solar cells was carried out at International Solar energy research Centre (ISC) Konstanz. All wafers were subjected to the identical steps as described below in Table 15.

Table 15: Steps conducted to process solar cells from passivated wafers

Step	Process	Chemical	Temp. [° C]	Time [min.]
1	Saw damage etch	NaOH (20 %)	80	10
2	Cleaning	HCl (5 %)	RT	5
3	Hydrophobic wafers	HF (2 %) dip	RT	2
4	Creating pn-junction	$POCl_3$-diffusion	850	20
5	P-glass removal	HF (2 %) dip	RT	2
6	Anti-reflecting coating	PECVD SiN_x (thickness: 73-75 mm)	450	-
7	Screen printing and firing	o Ag paste front grid o Al paste for BSF and back contact	Drying: 130-200 Firing: 840	-
8	Edge isolation by laser cutting	-	-	-

RT: room temperature (25 ºC)
PECVD: Plasma Enhanced Chemical Vapor Deposition
BSF: back surface field

6 Results

This chapter will present results from the castings and characterization performed. Results from two reference castings are included in some sections. The complete results of the reference castings are presented by Modanese *et al.* [90]

Only a representative selection of maps from PVScan, EBSD, µw-PCD and CDI, enough to emphasize the properties of the material, are shown in this chapter. Additional maps from the PVScan and µw-PCD is given in appendices.

6.1 Castings

The two ingots (MH1 and MH2) were cast under same conditions. The melting time, solidification time and average growth rate are given in Table 16. Melting time includes an isothermal step (constant temperature) of one hour prior to solidification. Rotation of crucible was only applied to MH2.

Table 16: Solidification conditions including melting time, solidification time and average growth

Ingot	Melting time [h]	Solidification time [h]	Average growth rate [cm/h]
MH1	7.28	6.84	1.55
MH2	7.18	6.57	1.61

No wetting of coating or crucible from melt occurred, in other words no sticking was observed. A transition from directional solidification to dendritic growth occurs close to the top of both ingots, however MH1 show a larger region than MH2 with the latter growth type. The pedestal and crucible was not positioned correctly during casting of MH1 which resulted in a large dendritic region.

Pictures of the two ingots are shown in Figure 30. The circles on top of MH2 are due to rotation of the crucible during casting. Silicon nitride and silicon carbide precipitates were present at the surface on the outer circumference.

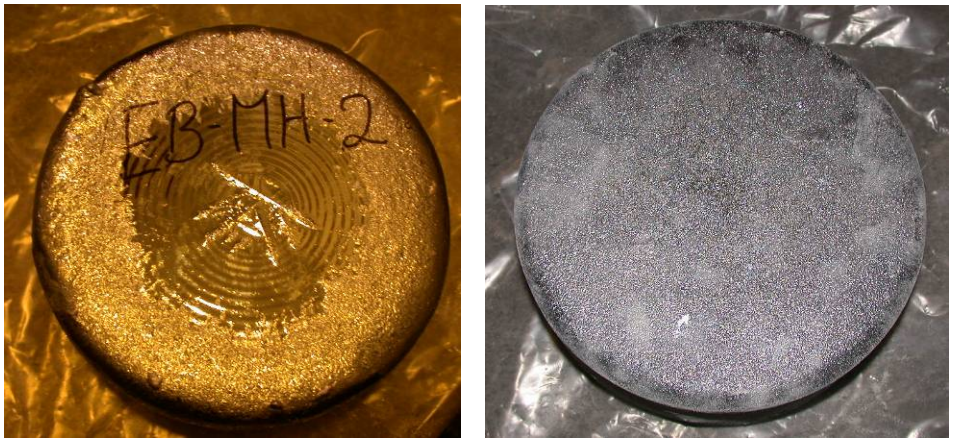

Figure 30: The surface of MH2 (left) and the bottom of MH1 (right) in as-cast ingots

A vertical cross-section revealed parallel and vertical grains, as Figure 31 shows.

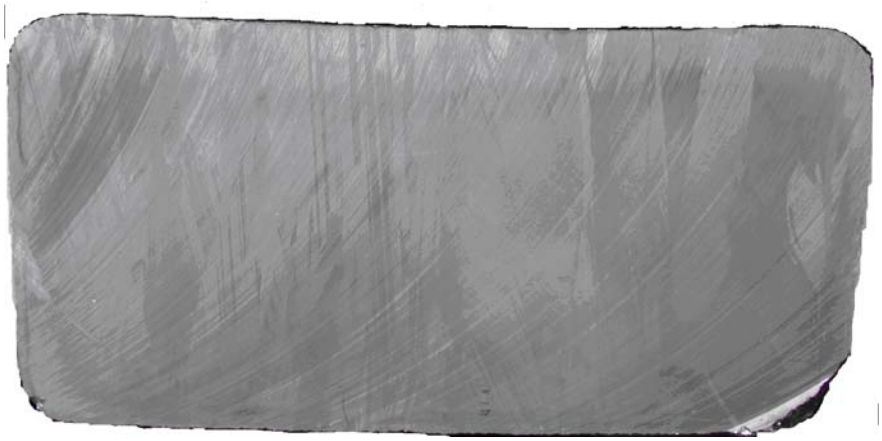

Figure 31: A cross-section picture of ingot MH2. The curved lines are from the cutting.

MH1 and MH2 have two parallel reference castings, ES1 and ES2, which have been cast under the same conditions and with same coating, crucible and Elkem Solar feedstock. ES1 and ES2 did not rotate during casting but should be somewhat comparable to MH1 and MH2.

6.2 Impurities and dopants

The total concentration of trace elements has been analyzed by GDMS. Measurements have been performed on several spots throughout the ingot height according to the illustration in Figure 32. Both bottom and top of each of the samples are analyzed.

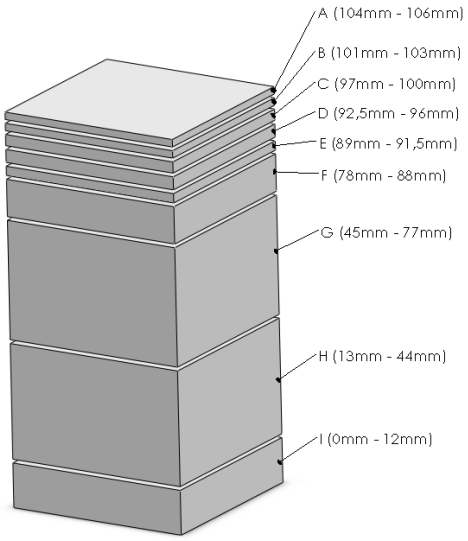

Figure 32: An example of samples for GDMS, shown here is block MH2-Q4. The samples are named A-I and the thickness of each piece are indicated in millimeter.

The concentration measured for each element is the sum of the dissolved and precipitated species. The analyses included aluminum, boron, calcium, chromium, copper, iron, molybdenum, nickel, phosphorus and titanium. However, nickel and molybdenum are present in concentrations below the detection limit of the instrument.

6.2.1 Aluminum

The aluminum concentration throughout the ingot is shown in Figure 33. An elevated level of aluminum is present in MH1 compared to the other ingots. However, the distribution in MH1 is quite consistent with what is expected; an increase towards the top due to segregation as well as back-diffusion from the very top after complete solidification. Only one other measurement can match the aluminum content of MH1, which is the measurement of ES1 almost at the top of the ingot. At this height, dendritic growth is dominating. The dendritic region contains segregation and particles rich of impurities. Thus, it should not be given too much attention.

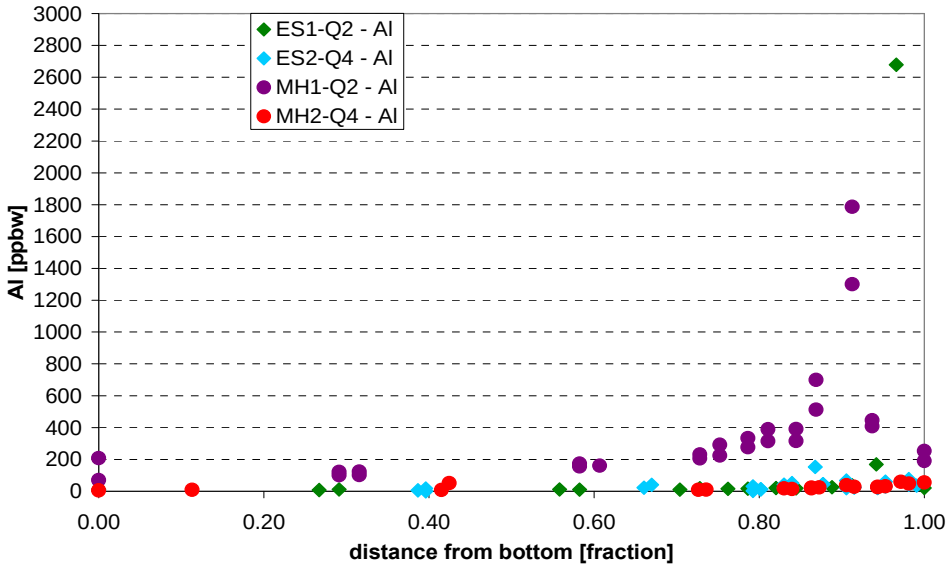

Figure 33: Aluminum concentration as a function of height. All points measured are included in this graph.

The distribution of aluminum in the three other ingots becomes more pronounced by decreasing the concentration range, as shown in Figure 34. ES1, ES2 and MH2 are not subjected to very significant segregation as the equilibrium distribution coefficient is equal to $2 \cdot 10^{-3}$. Moreover, the content and distribution in the three ingots are all in quite good agreement.

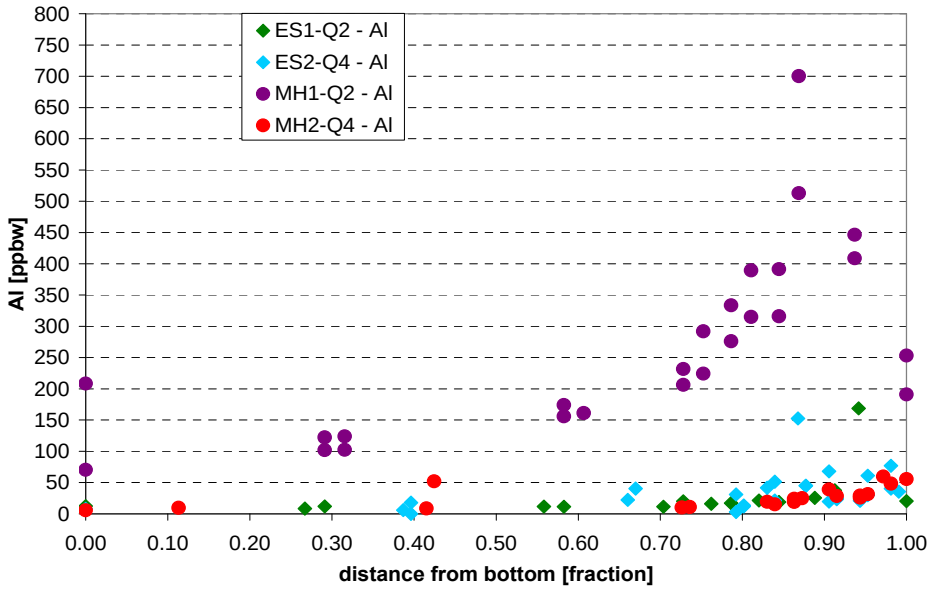

Figure 34: Aluminum concentration as a function of ingot height. A narrower concentration range than in Figure 33 is shown.

6.2.2 Boron

The concentration of boron is measured by GDMS and is shown in Figure 35. The Scheil distribution is also included in the figure and is calculated according to Equation (2.4). The initial concentration, C_0, is the concentration of boron in the feedstock as measured by the same GDMS instrument.

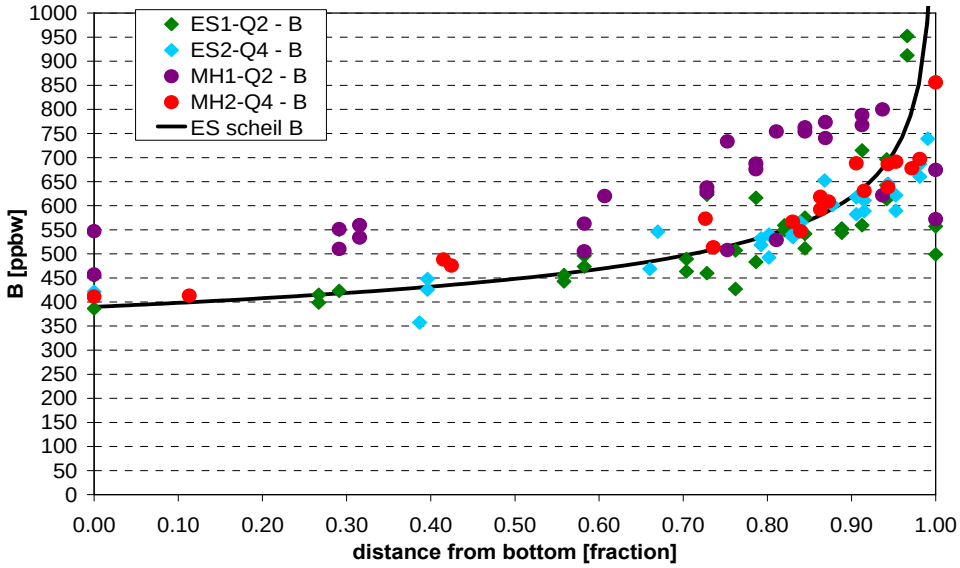

Figure 35: Boron concentration as a function of height. The Scheil distribution calculated from the initial concentration is also included in the figure.

MH1 does also contain higher concentrations of boron than the other ingots and have the least agreement with Scheil's equation. MH2 is in good agreement with Scheil's equation as well as the ES ingots.

The boron concentrations measured by ICP-MS are plotted below in Figure 36. Position 1 corresponds to the bottom of the ingot while position 5 represents the top. For complete ICP-MS results see Appendix B.

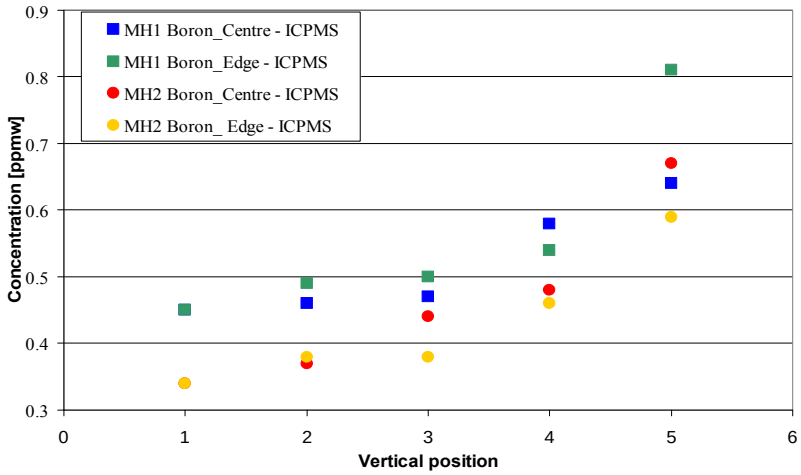

Figure 36: The boron concentration as given by ICP-MS as a function of height in the ingot. 1 represents the bottom of the ingot while 5 represent the top of the ingot

Boron concentrations are homogenously distributed in the lateral direction as the centre and edge for both ingots are consistent. Also apparent from Figure 36 is the slightly lower boron content of MH2 compared to MH1 as indicated by the GDMS measurements as well. Notice the exact overlap between centre and edge points at position 1 for the respective ingots.

6.2.3 Chromium

Figure 37 shows the chromium concentration as a function of the ingot height.

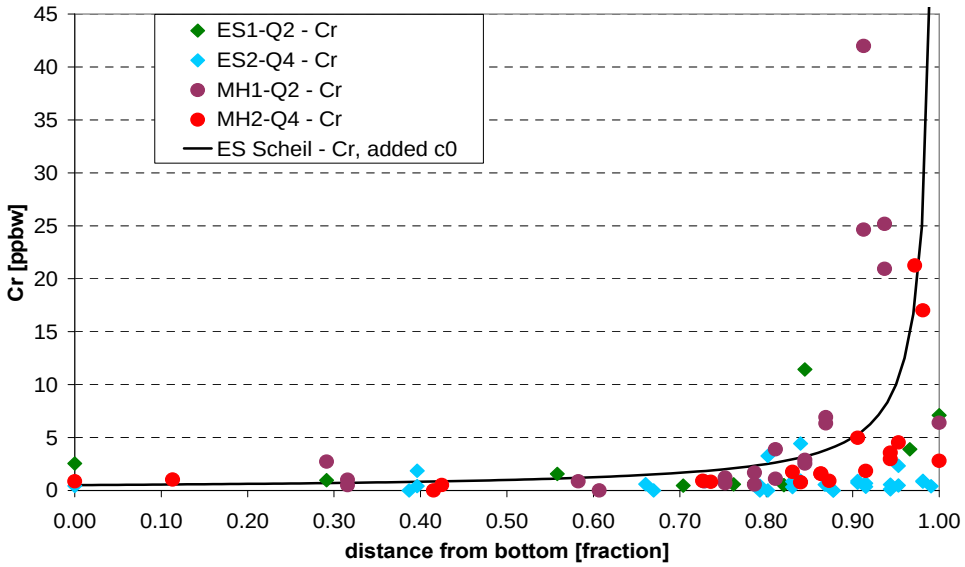

Figure 37: Chromium concentration throughout the ingot height. All spots measured are shown in this graph.

To show the differences between the ingots the concentration range in Figure 37 is decreased in Figure 38 excluding some measurements from MH1 and MH2 with very high concentrations of chromium.

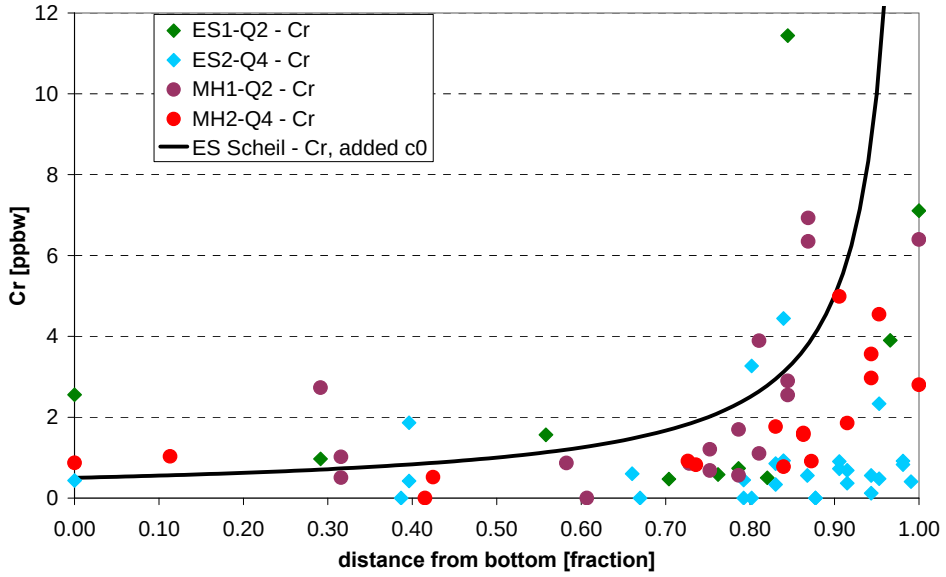

Figure 38: A more narrow range of chromium concentrations as a function of height than Figure 37

The chromium concentration in MH1 and MH2 is slightly higher than the reference castings, especially when approaching the top. The agreement with Scheil's equation is better for MH1 than MH2.

Concentrations around 3-4 ppbw or lower are on the detection limit of the instrument and it can be considered as upper limits (i.e. exact concentration might be a little lower). Only concentrations without significant background noise are plotted.

6.2.4 Iron

As shown in Figure 39, the iron concentration of all the castings is within the same concentration range except for three irregular spots.

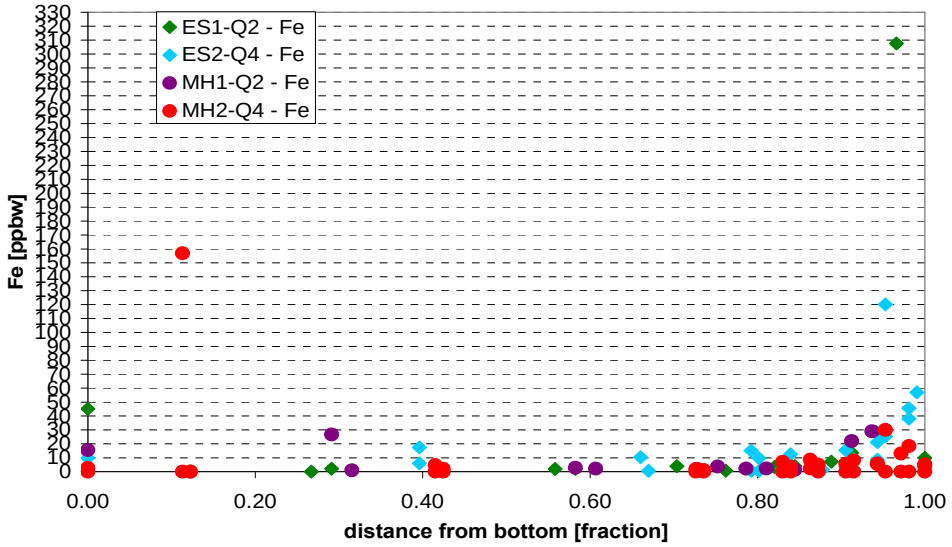

Figure 39: The concentration of iron plotted against the height of the ingot. The whole concentration range where measurements are performed is included.

The three spots with highest concentration of iron are excluded from the graph, and the result is shown in Figure 40.

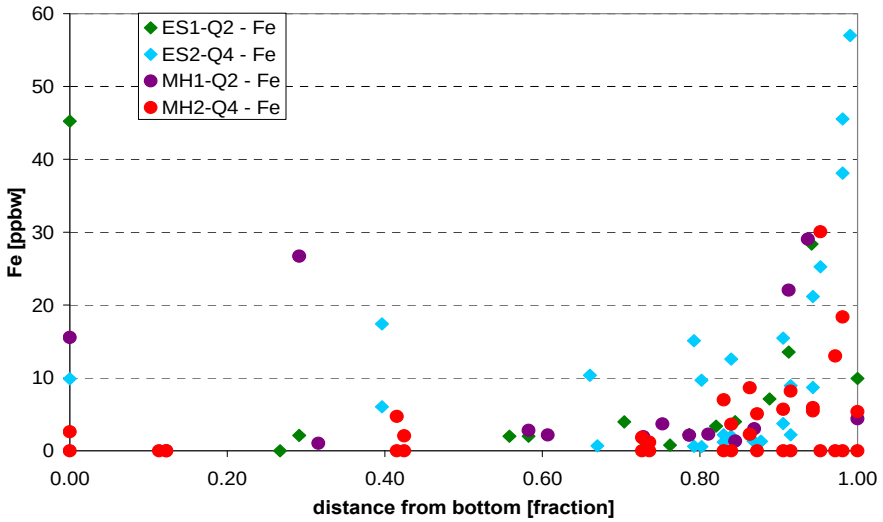

Figure 40: An extraction from the lower iron concentration region in Figure 39 plotted as a function of ingot height.

There is reasonable similarity between the distributions of iron corresponding to the four castings, ES2 is slightly more elevated. The high concentrations of iron present at the very bottom of the ingots are due to in-diffusion from coating and crucible after solidification. MH1 and MH2 contain relatively low concentrations of iron, similar to that observed in ES1. An accumulation of iron has occurred at the top of the ingot due to the segregation during solidification, exactly like chromium.

6.2.5 Phosphorus

The phosphorus concentration profile of MH2 shows good agreement with Scheil's equation, as shown in Figure 41, while the phosphorus concentration in MH1 is somewhat enhanced along the whole height of the ingot.

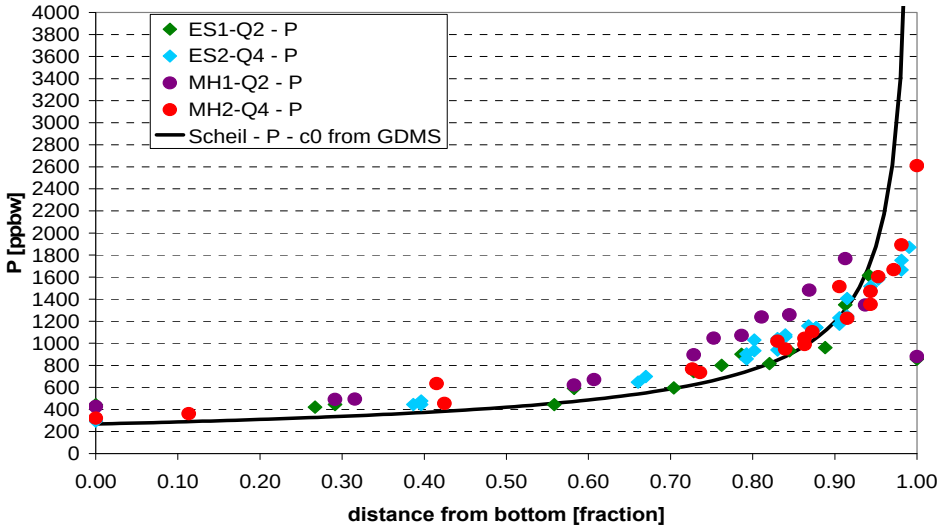

Figure 41: Phosphorus concentration as a function of the fraction solid, i.e. ingot height

6.2.6 Titanium

The concentration of titanium versus the ingot height is given in Figure 42.

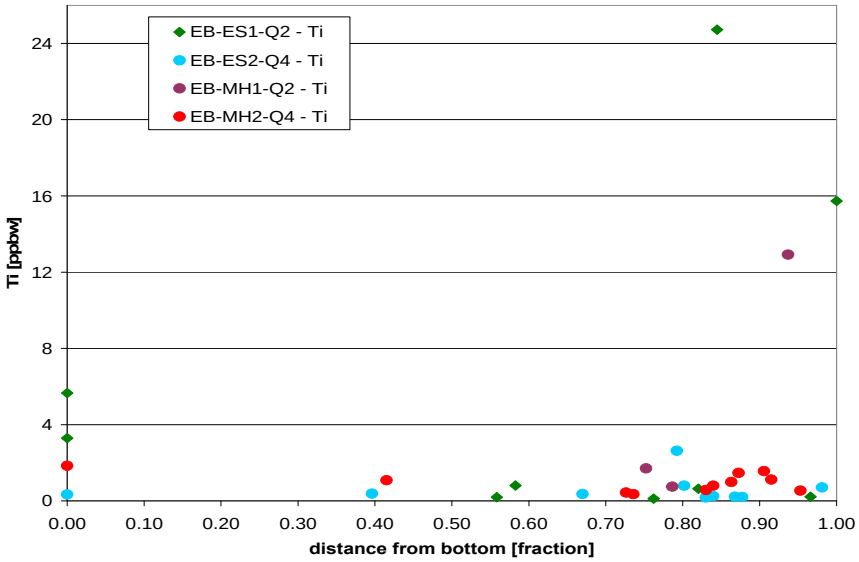

Figure 42: Concentration of titanium as a function of distance from the bottom of the ingot

There are very low concentrations (< 4 ppbw) of titanium throughout the ingot with peaks at the bottom and top. These concentrations can be considered as upper limits or

detection limits of the instrument for titanium. In-diffusion from crucible and coating can account for the enhanced titanium content at the bottom of the ingot.

Notice that points not included in the figure is either not detected or the signal was too noisy to extract something reasonable.

6.3 Effective segregation coefficient

The effective segregation coefficients have been calculated for five different impurities by the least-squares method. Only values for MH2 are included in the GDMS measurements which the calculations are based on.

Table 17 lists the calculated effective segregation coefficients for a selection of impurities as well as their equilibrium segregation coefficients. All elements, except for phosphorus, correlate well with their respective equilibrium values.

Table 17: A comparison between the equilibrium and the calculated effective segregation coefficient for a selection of impurities and dopants

Element	k_{eff}	k_0
Al	$4.5 \cdot 10^{-4}$	$2.0 \cdot 10^{-3}$
B	0.83	0.8
Cr	$4.1 \cdot 10^{-4}$	$1.1 \cdot 10^{-5}$
Fe	$9.4 \cdot 10^{-5}$	$8.0 \cdot 10^{-6}$
P	0.61	0.35

For boron and phosphorus the two top points are excluded from the calculations because they are in the dendritic region. When incorporated into the calculations, the k_{eff} of boron and phosphorus are 0.92 and 0.84 respectively.

6.4 Light elements

Substitutionally bonded carbon and interstitially bonded oxygen concentrations are measured with FTIR, while the total concentration of oxygen and carbon are characterized by LECO.

The measurements are done a cross-section slice according to the sketch shown in Figure 43. Both centre and edge of the slice are included in the measurements.

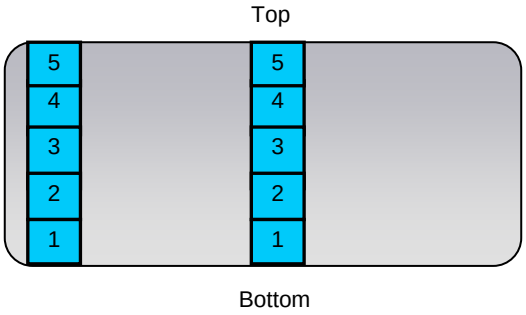

Figure 43: A vertical cross-section slice cut in smaller pieces, 1-5, for LECO analysis

LECO measurements are performed on the same slice as utilized for µw-PCD. It is assumed axial symmetry within the ingot and hence analyzing one edge of the slice is sufficient.

Three parallel measurements are carried out for each position, the average of the three are plotted in the following figures.

6.4.1 Oxygen

The concentration of oxygen measured by FTIR as a function of ingot height is presented in Figure 44.

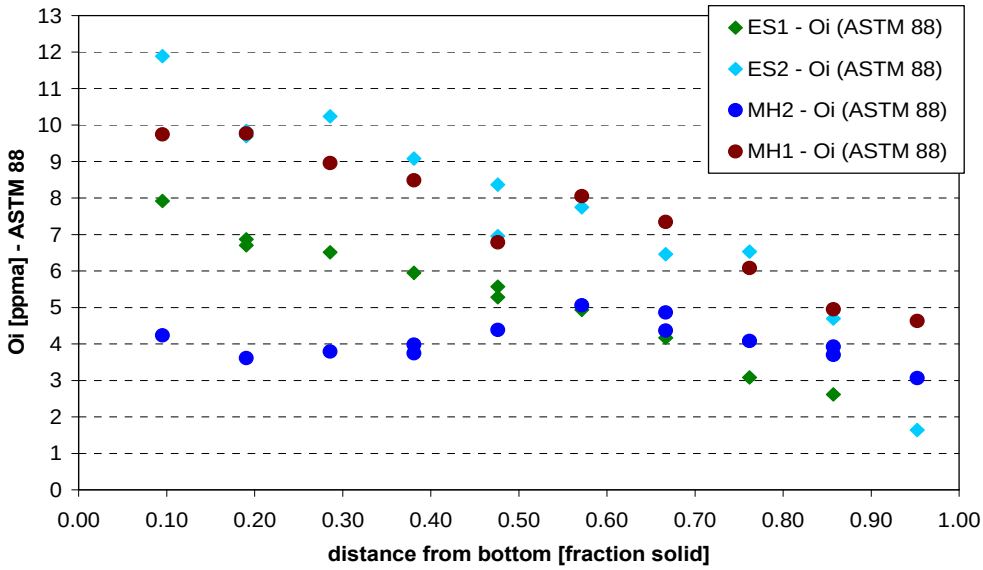

Figure 44: Oxygen concentration along the ingot height as measured by FTIR

MH1, ES1 and ES2 show a decreasing trend when moving towards the top, which is due to a segregation coefficient larger than 1 ($k_0 > 1$). The wave-like trend of MH2 around an average value of 4 ppma is different from the other ingots and such a distribution is normally not observed. Furthermore, the concentration of oxygen in MH2 is much lower than concentrations obtained in MH1 as well as ES1.

Figure 45 presents the oxygen concentration of MH1, as measured by LECO, as function of ingot height. Position 1 corresponds to the bottom while position 5 is the top according to Figure 43.

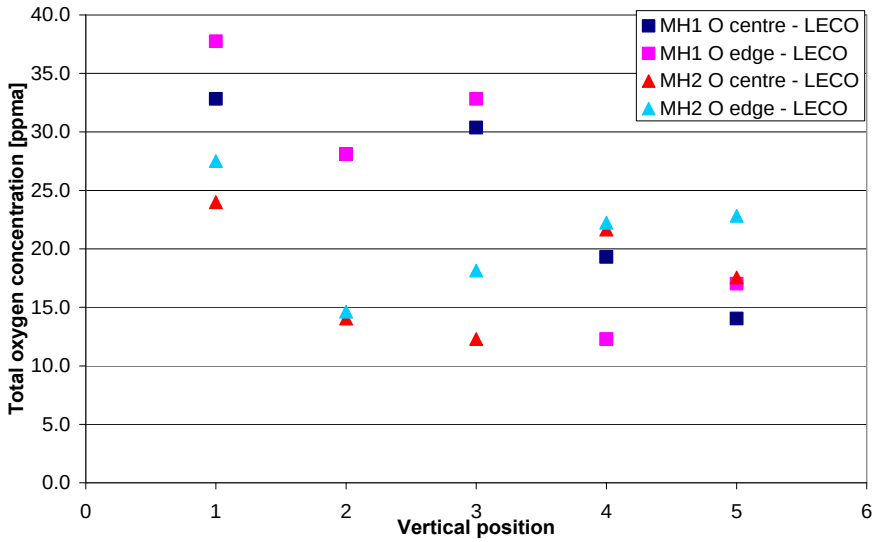

Figure 45: The total oxygen concentration as measured by LECO

Some variation in the total oxygen content between edge and centre is observed for both MH1 and MH2. The edge is exposed to diffusion from crucible and coating. As expected the oxygen concentration decreases toward the top of the ingot, which is also the case for the oxygen measurements by FTIR. However, as LECO measures the total oxygen concentration and FTIR only the interstitial concentration the residual oxygen must be found as precipitates or in connection with other complex states.

Notice that the edge and center concentration of MH1 at position 2 as well as the edge of MH1 and centre of MH2 completely overlaps at position 5.

6.4.2 Carbon

A low carbon concentration in the MH castings compared to the reference castings can be observed from the FTIR measurements presented in Figure 46. The distribution of MH1 and MH2 are in good accordance with each other and ES1.

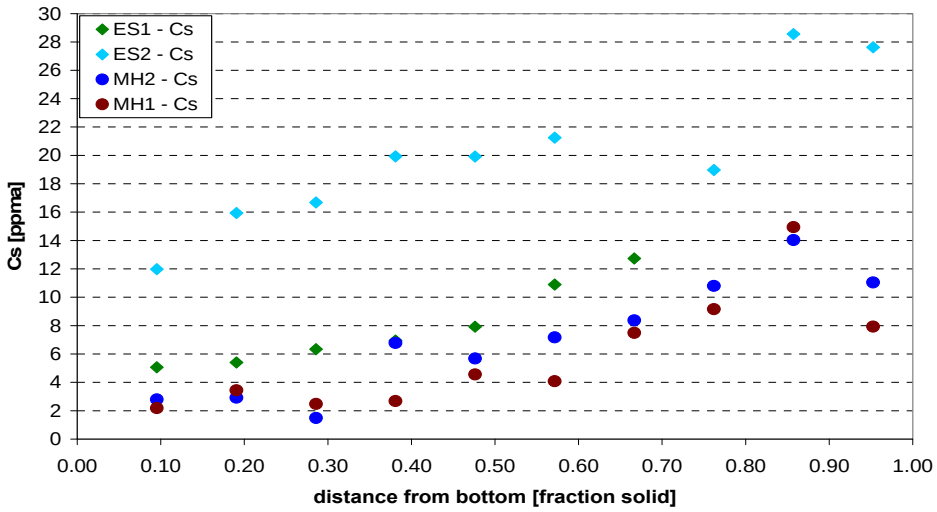

Figure 46: The carbon concentration by FTIR as a function of ingot height for both chromium doped (MH) and reference (ES) castings

The total carbon concentration quantified by LECO is given as a function of ingot position in Figure 47. As for the oxygen measurements, position 1 is at the bottom and position 5 corresponds to the top.

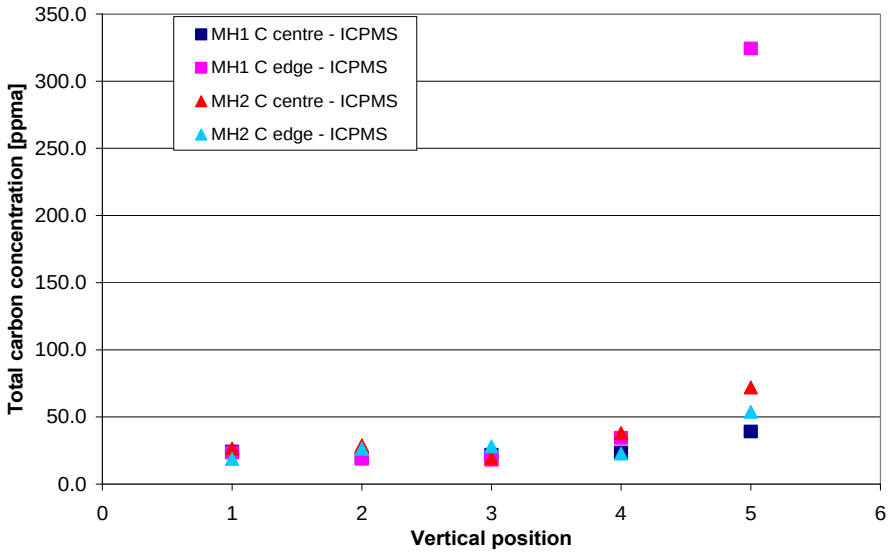

Figure 47: The total carbon concentration given by LECO

At position 5 MH1 shows very high concentrations of carbon. This spot is located in the dendritic region where segregation of impurities can be found as well as particles of silicon carbide. Otherwise, the ingots show consistent behavior and concentrations are overlapping for both ingots at position 1-4.

6.5 Minority carrier lifetime mapping

The mapping of minority carrier lifetime variations within the ingot was performed with µw-PCD. A cross-section map of MH1 is shown below in Figure 48.

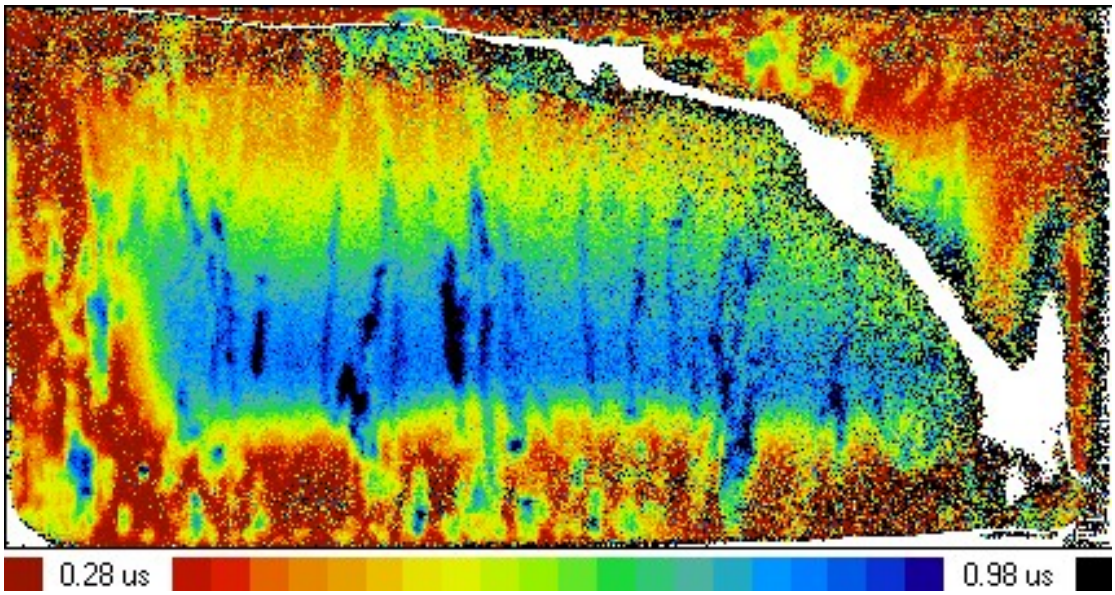

Figure 48: Minority carrier lifetime of a cross-section slice of ingot MH1

Even the maximum lifetimes recorded within the core of MH1 are below 1 µs. The red-zone is not as pronounced as observed in other ingots (e.g. reference castings), but at these low values the instrument is operating at its limit. The same observation also occurs for MH2, as can be seen in Figure 49. Lifetime are also very low for MH2.

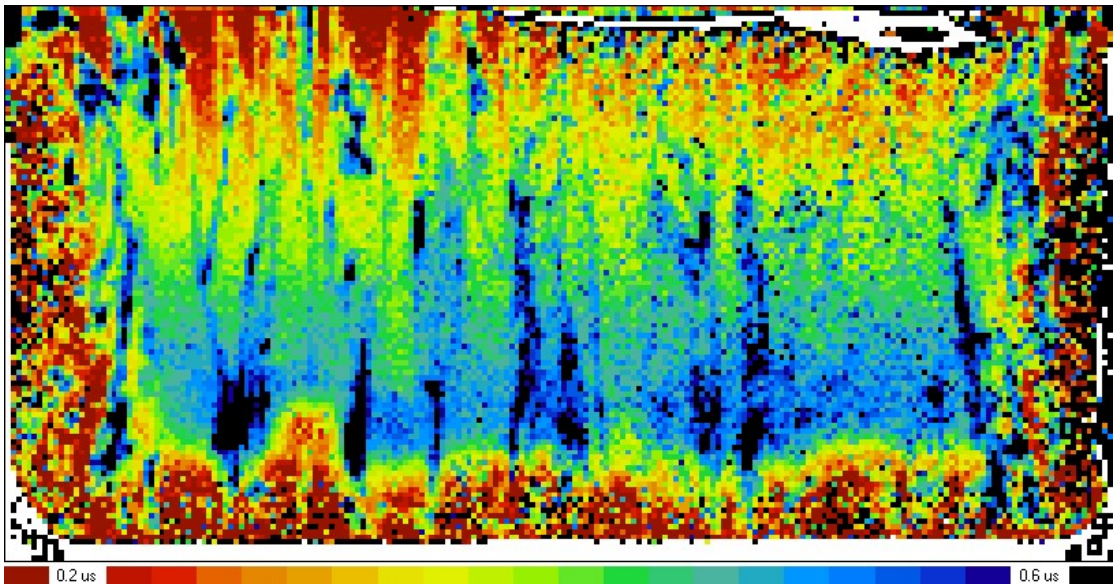

Figure 49: Minority carrier lifetime mapping of ingot MH2. The sample is a vertical cross-section cut through the ingot

Note that the colors scales of the images in Figure 48 and Figure 49 are not the same. The white areas within the images are regions which are out of range for the instrument to measure.

Table 18 presents the average lifetime of the four ingots. There is a significant difference between the reference ingots and the chromium doped ingots, where the MH ingots are one order of magnitude lower than the reference castings. ES2 possess only half the lifetime recorded in ES1.

Table 18: The average bulk lifetimes of the reference and chromium doped ingots

Ingot name	Lifetime [µs]
ES1	15
ES2	7
MH1	0.8
MH2	0.51

6.5.1 Lifetime based iron concentration calculations

Interstitial iron concentration can be calculated according to Equation (4.1) by measuring lifetime before and after light soaking, as explained in Section 4.4 (assuming that lifetime changes are only due to iron). The result from such calculations is shown in Table 19.

Table 19: Average interstitial iron concentration in the four ingots (based on bulk lifetimes given in Table 18)

Ingot name	$[Fe] \cdot 10^{10}$ [atoms/cm^{-3}] (ppbw)
ES1	> 1 ($> 4 \cdot 10^{-4}$)
ES2	708 (0.29)
MH1	180 (0.07)

Measurements were not performed on the slice from MH2. Compared to ES1, MH1 and ES2 contain much higher concentrations of interstitial iron, a difference of two orders of magnitude exists between the two ingots. However, the absolute concentration of interstitial iron is still very low for both ingots compared to the iron concentration measured by GDMS. These measurements imply that the additional iron is present as a precipitate. Complementary discussions of iron concentration calculations based on lifetime are given in a later section.

6.5.2 Comparison of lifetime mapping by µw-PCD and CDI

The lifetime maps of wafer MH1-113 and MH1-116 is recorded by CDI and µw-PCD respectively and is shown in Figure 50 with a topography map from CDI (bottom). The two lifetime maps are oriented as mirror images of each other and consequently the centre of the ingot coincide at the top corner of both images, right for MH1-116 (µw-PCD) and left for MH1-113 (CDI).

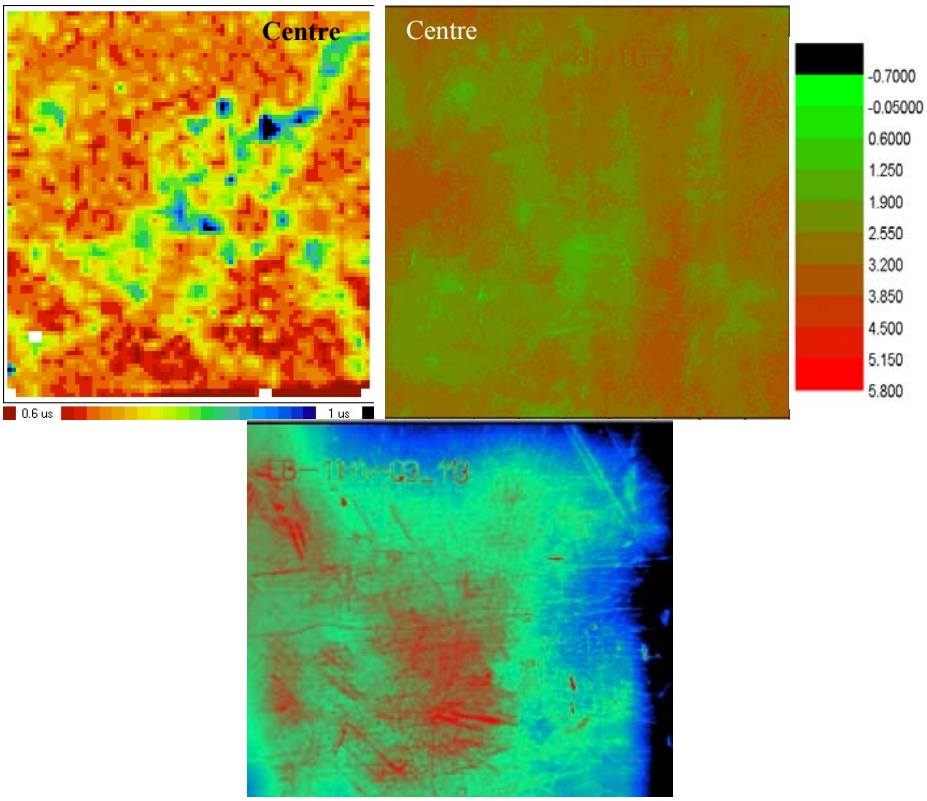

Figure 50: Lifetime maps recorded by µw-PCD and CDI of wafer MH1-116 (left) and MH1-113 (right), respectively, as well as a topography map of MH1-113 recorded by CDI. Notice that there is no scale in the topographic picture and the colors does not correspond to the lifetime map

Little correspondence is observed between the lifetime maps, neither for the scale of lifetimes nor the grain structure of the wafers. CDI could not be performed on wafers from MH2 because the rough surface structure caused too much interference.

6.6 FeB and CrB pairs

The detection of iron boron and chromium boron pairs and their effect on lifetime have been performed by a combination of heat treatment, light soaking and the characterization techniques QSSPC and µw-PCD.

Wafers included in this characterization are listed in Table 20 and have been passivated prior to the measurements (as described in Section 5.3.4).

Table 20: Wafer number and their respective ingot heights used for FeB and CrB pair characterization

Ingot	Wafer no.	Height in ingot [%]
MH1	116	51.3
	119	52.7
MH2	120	51.1
	121	51.5
	203	86.4
	204	86.8
	214	91.1
	215	91.5
	227	96.6

6.6.1 Iron boron and chromium boron pairs in MH1

Lifetime by QSSPC and lifetime map by µw-PCD was obtained prior to light soaking and heat treatment. The results from the initial measurements can be seen in Figure 51 and Table 21.

After light soaking of wafer MH1-116 the lifetime did not change from the constant value of 0.5 µs. QSSPC characterization was also performed after heat treating the same wafer (MH1-116). The lifetimes are listed in Table 21. Initial time indicates the measurement on the as-passivated wafer, while time equal to zero is the measurement conducted instantly after heat treatment. All lifetimes correspond to an injection level of 10^{14} cm^{-3}.

Table 21: Lifetimes characterized by QSSPC on wafer MH1-116 before (initial) and after heat treatment. Injection level (Δn) is equal to 10^{14} cm^{-3}.

Time [min]	Lifetime [µs]
Initial	0.5
0	0.54
15	0.57
30	0.55
60	0.52
180	0.51
> 18 [a]	0.52

[a] hours

No change in lifetime was observed for MH1-116. The heat treatment did not have any effect on lifetime, as can be seen in the lifetime maps from the same wafer in Figure 51. Please notice that the scale has been adjusted to the same range.

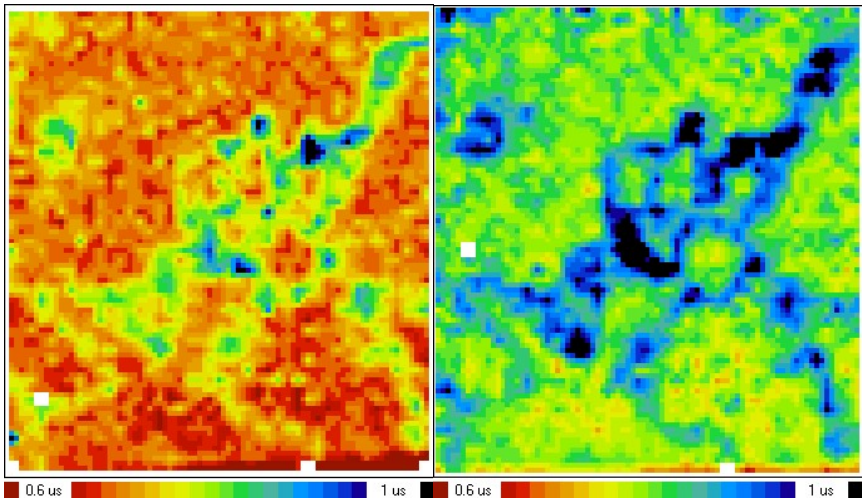

Figure 51: Initial (left) lifetime map from wafer MH1-116 as well as after 30 min. (right) after heat treatment

Even though the colors change drastically in the two images the lifetime recorded show only minor variations. Moreover, the wafer has very low lifetime and the instrument is operating close to its detection limit.

6.6.2 Iron boron and chromium boron pairs in MH2

The same procedure with light soaking and heat treatment was performed on three wafers from MH2. No change in lifetime occurred for any of these wafers, neither for light soaking nor heat treatment, the lifetimes are shown in Table 22. The lifetimes recorded correspond to an injection level of 10^{14} cm^{-3}. The lifetimes listed are measured 30 minutes after processing but are still representative values due to non-alternating lifetimes. Even 2 hours later the lifetime was still identical.

Table 22: Lifetimes measured on three wafers from MH2 before and after light soaking and after heat treatment. Injection level is 10^{14} cm^{-3}. Lifetimes after both processes were obtained as a function of time. However, since the lifetime did not change as a function of time, the lifetime recorded after 30 minutes is what is listed below.

Wafer name	Lifetime as-passivated [µs]	Lifetime after light soaking [µs]	Lifetime after heat treatment [µs]
MH2-120	0.28	0.27	0.31
MH2-203	0.17	0.18	0.19
MH2-214	0.15	0.14	0.17

The minor change in lifetime is probably not due to FeB or CrB pairs. Since the lifetime is very low initially, such small variations which are not due to the material itself can occur between the measurements.

6.6.3 Crossover point

Both light soaking and heat treatment was conducted on wafer MH1-119 followed by QSSPC measurements at different injection levels to determine the crossover point. Table 23 lists the lifetime on the as-passivated wafer as well as after light soaking and heat treatment.

Table 23: Injection level dependent lifetime measurements on wafer MH1-119 before and after light soaking and after heat treatment. Notice that it was not possible to conduct lifetimes for injection levels corresponding to 10^{15} and 10^{16} cm^{-3}.

Injection level [cm^3]	Lifetime as-passivated [µs]	Lifetime after light soaking [µs]	Lifetime after heat treatment [µs]	Lifetime after 2nd light soaking [µs]
10^{13}	0.22	0.21	0.24	0.22
10^{14}	0.41	0.41	0.43	0.40

No change in lifetime occurred for this wafer as with MH1-116, for any type of processing. Consequently, a crossover point could not be located.

6.6.4 Interstitial iron concentration

The interstitial iron concentration can be deducted from lifetimes measured by µw-PCD before and after exposing the samples to light flashing. The difference in lifetime constitutes, together with a constant, the basis for calculating the iron content. The formula for calculating the interstitial iron content is given in Equation (4.1).

The average bulk concentration of interstitially bonded iron was found in four wafers from MH2 and one wafer from MH1, the results are shown below in Table 24.

Table 24: The bulk concentration of interstitially bonded iron for wafers from ingot MH2

Wafer name	Average Fe-concentration [cm^{-3}]	Average Fe-concentration [ppbw]
MH2-121	$3.87 \cdot 10^{12}$	0.156
MH2-204	$8.0 \cdot 10^{12}$	0.323
MH2-215	$1.10 \cdot 10^{13}$	0.444
MH2-227	$1.38 \cdot 10^{13}$	0.556
MH1-121	$1.40 \cdot 10^{12}$	0.056

The low concentrations of interstitial iron are in good agreement with the average bulk value recorded for the slice, given in Table 19. Two iron concentration maps are included as examples in Figure 52. The corresponding lifetime maps are shown in Figure 53. Due to a failure the lifetime image of MH2-227 was not recorded. The lifetime image

of wafer MH2-226 is shown instead. The grain structure should, however, correspond very well to each other.

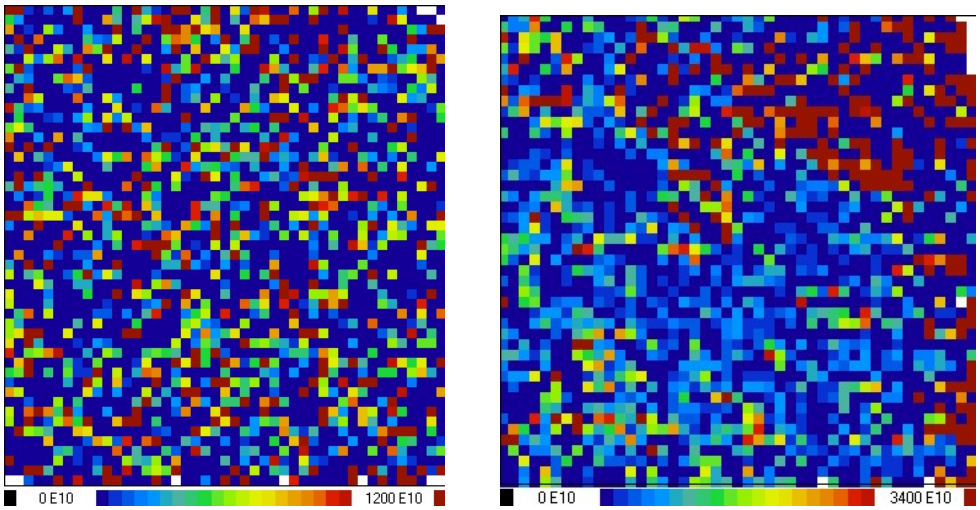

Figure 52: Maps displaying the iron concentration of wafer MH2-121 (left) and MH2-227 (right)

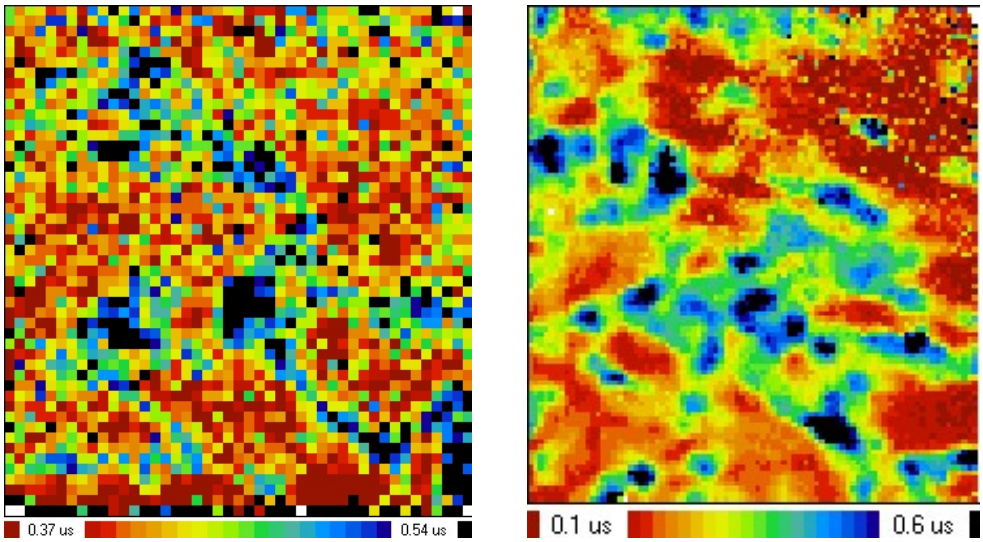

Figure 53: Lifetime maps corresponding to the iron concentration maps. Left map; MH2-121, right map; MH2-226. Due to some failure during the measurements on 227 the lifetime map from the parallel wafer 226 is shown.

The features in the lifetime maps are clearly corresponding to features in the interstitial iron concentration maps. Nonetheless, care must be taken when considering the interstitial iron calculated by such a method due to several sources of error. This is discussed in the next chapter.

6.7 Resistivity

The resistivity is measured by a four point probe on the same samples as for the GDMS analysis. The results are shown in Figure 54.

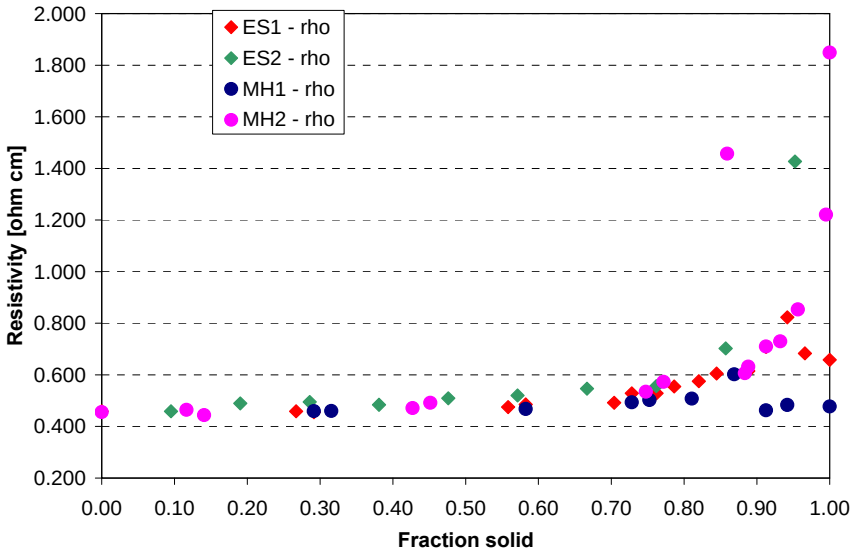

Figure 54: Resistivity measured as a function of ingot height in the four castings

MH1 indicates almost a constant resistivity. Even towards the top of the ingot, where there is a larger scatter between measurements, resistivity is quite steady at ~0.5 ohm·cm. The trend for MH2 is very different from MH1 showing an exponential behavior above ~80 cm ingot height. One measurement located at 90 cm ingot height deviates from the resistivity profile of MH2. This might be caused by a grain boundary, which demonstrates a much lower conductivity than grains, or it is due to other non-electrical particles located exactly in the area measured. It should not be given too much attention.

For measurements close to the top, in the dendritic region, a variation of up to ± 29 % must be taken into account, while an error of ± 8 % applies to the other ingot heights.

6.7.1 Majority carrier type transition

A transition from p- to n-type material, which can occur for compensated material, was investigated by the GDMS concentration measured for donor (P) and acceptor (B+Al) species, the predicted concentrations for the abovementioned species are given by Scheil's equation.

With an initial boron concentration, [B], of 1265.5 ppba and an initial phosphorus concentration, [P], of 693.9 ppba, measured on feedstock material, Scheil's equation predicts the following results, presented in Figure 55.

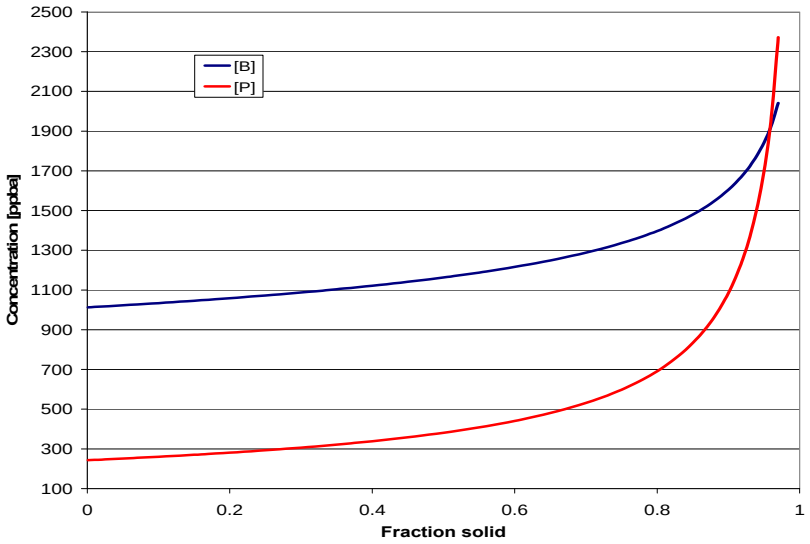

Figure 55: The calculated boron and phosphorus concentrations given by Scheil's equation along the height of the ingot

The transition should be happening between 0.95 and 0.96 fractions solid. The real distribution of boron and phosphorus quantified by GDMS for MH1 and MH2 is shown in Figure 56 below.

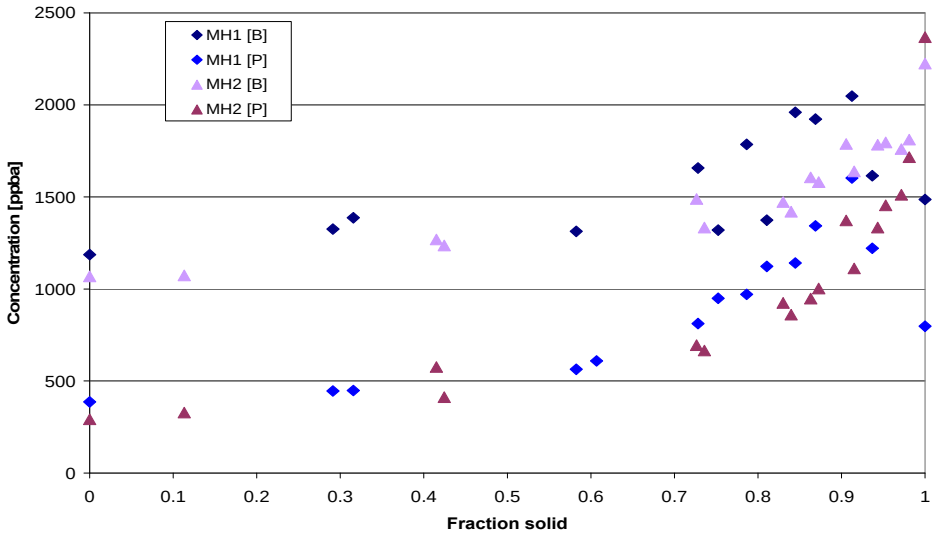

Figure 56: The boron and phosphor concentration plotted as a function of the fraction solid for MH1 and MH2 respectively

No transition in majority carrier type occurred for either of the two ingots since [B] is constantly higher than [P] throughout the ingot height. A transition is almost occurring at the very top of the ingot in MH2. However, this is in the dendritic region where large variations arise.

Also a hot probe technique was applied to the Q3 block of MH1. The hot probe is based on the Seebeck effect where voltage is generated by a temperature gradient. The voltage difference, ΔV, between the probes is either positive or negative to indicate n-type or p-type material, respectively. Throughout the block of MH1, also including the dendritic region, the hot probe gave a negative voltage difference. Thus, the silicon is exclusively p-type. This corresponds to the concentrations from the GDMS analysis, shown in Figure 56.

6.8 Grain orientation mapping

The EBSD maps were conducted with a Zeiss Supra 55 VP instrument at samples from the bottom (~ 10 %), middle (~ 50 %) and top (~ 90 %) of the ingot.

The inverse pole figure included in each figure refers to the growth direction of the ingot; hence maps are normally orientated with respect to grain alignment.

Figure 57 and Figure 58 display the grain orientation maps from 9.7% and 49.6 % height, respectively.

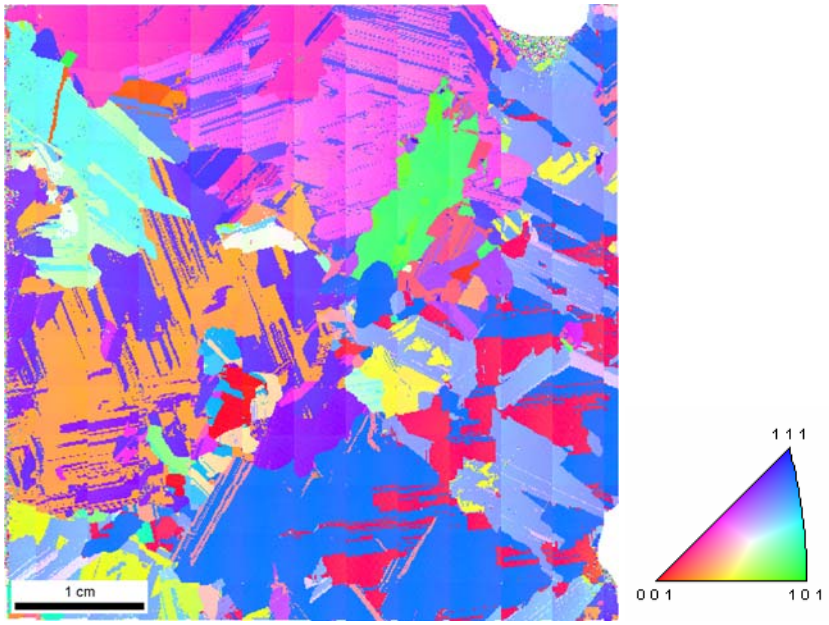

Figure 57: Grain orientation mapping of wafer MH1-22 (9.7 % height), the inverse pole figure is shown to the right. The bottom right of the image is closest to the centre of the ingot.

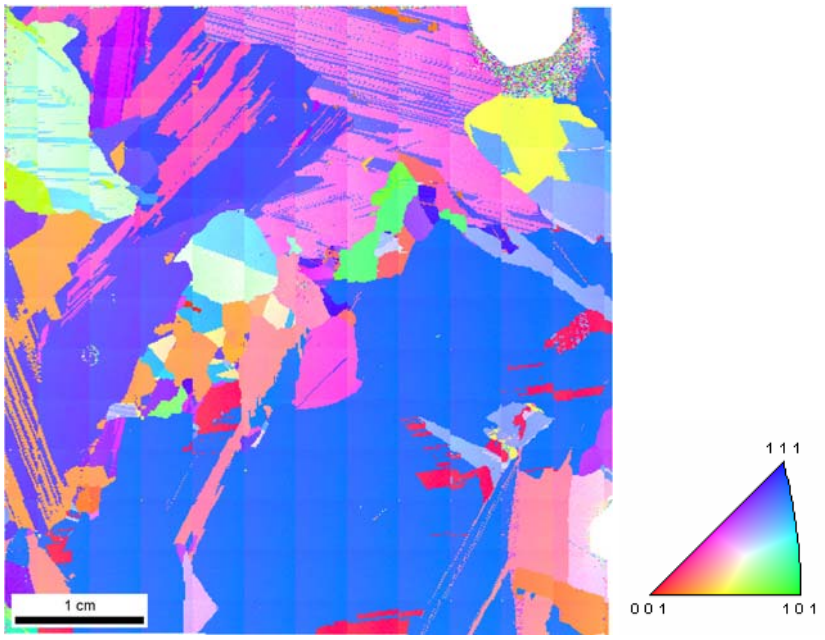

Figure 58: Grain orientation mapping of wafer MH1-112 (49.6 % height), the inverse pole figure is shown to the right. The bottom right of the image is closest to the centre of the ingot.

At the bottom wafer (Figure 57) several small grains are present, but as the growth precede the number of grains decrease, as shown in Figure 58. In addition, the number of twin boundaries is enhanced.

The white semicircle up in the top right and bottom right corner of sample 22 and 112, respectively, is due to the sample holder. This is also present at another orientation in wafer 202, shown in Figure 59. Wafer 202 corresponds to 89.4 % height in the ingot.

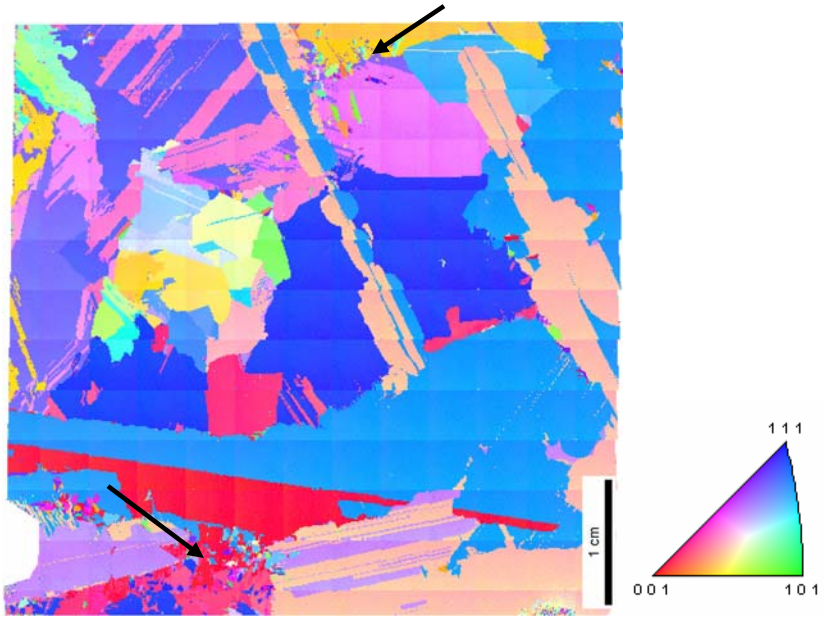

Figure 59: Grain orientation mapping of wafer MH1-202 (89.4 % height), the inverse pole figure is shown to the right. The bottom right of the image is closest to the centre of the ingot. Arrows indicate regions were dendritic growth is starting to develop.

Towards the top (Figure 59) the grain structure is again more disordered and some areas of the wafer are at the edge of breaking into dendritic growth (see black arrows).

No maps were recorded for MH2 due to problems with the EBSD instrument. However, an optical image of a wafer from ~50 % height is included due to its relevance for further discussions. It is shown below in Figure 60.

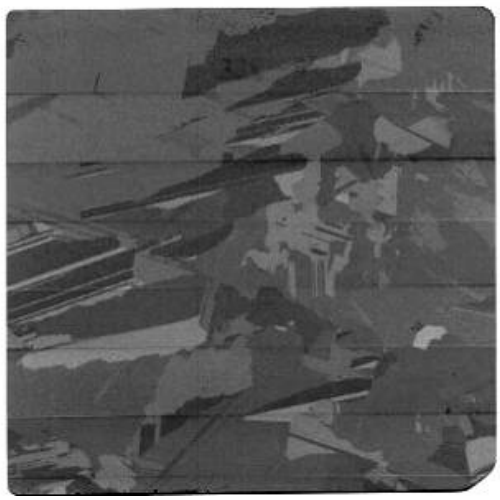

Figure 60: An optical image of wafer no. MH2-125, the centre of the ingot is located in the top left corner

Notice the almost half and half division of the grain structure where the left hand side is covered by mostly twin boundaries and large grains, while the right hand side is much more disordered containing many small grains with different orientation.

6.9 Dislocation Density

The dislocation density was recorded for a total of 9 positions in the ingot with a PVScan 6000 instrument, and is shown in Figure 61 and Figure 62. Due to preparation effects from the polishing and etching the maps from MH2 have poorer quality than MH1. Notice that maps from MH1 and MH2 all correspond to the same scale.

In the bottom, here represented by MH1-33, several small severely twinned areas occur. The microstructure of the wafer is highly disordered, but with few dislocation clusters. Large grains and some larger dislocation clusters are found in MH1-112. Several lines due to what looked like a preparation effect are shown as straight lines interfering with the grain structure. At the top the dislocation clusters have multiplied and grown, as shown in the bottom images in Figure 61.

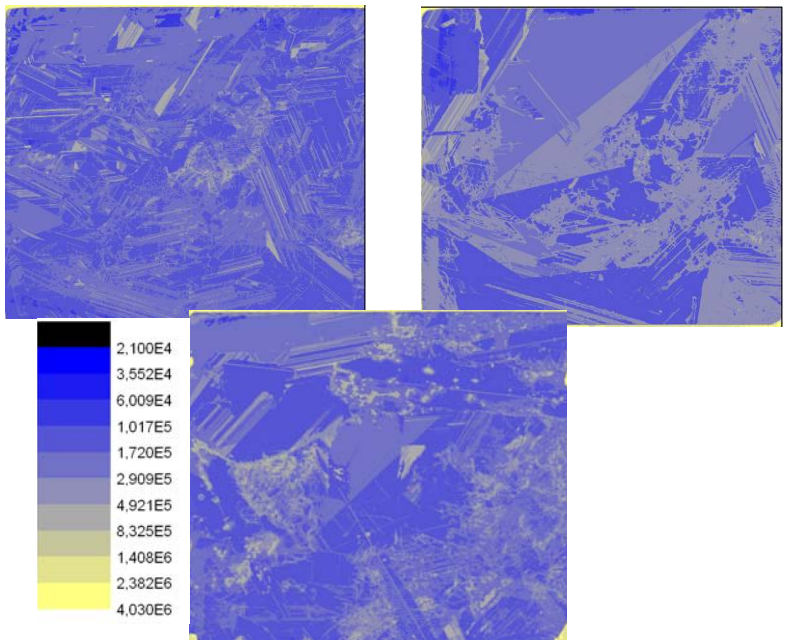

Figure 61: Dislocation density maps of wafer MH1-33 (top left), MH1-112 (top right) and MH1-201 (bottom)

Dislocation density maps for wafers close to the top (MH2-210), close to the bottom (MH2-33) and approximately from the middle of the ingot (MH2-116) are given below in Figure 62. The scale bar included in the figure is common for all three maps.

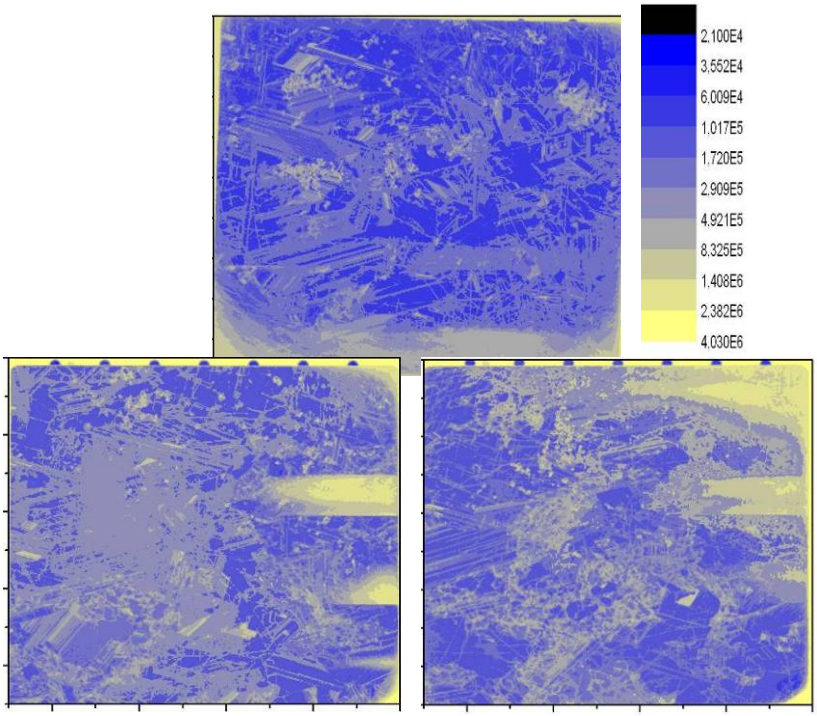

Figure 62: PVScan dislocation density map of wafer MH2-33 (top) MH2-116 (bottom left) and MH2-210 (bottom right). A common scale is applied for all three maps.

Several twinned areas are present in MH2-33 and MH2-116. In MH2-210, however, there is almost exclusively large dislocation clusters with two small regions consisting of twins. The dislocation clusters are small and separated by a larger distance in MH2-33. As the solidification front has progressed the dislocation clusters have grown and new clusters have formed, as can clearly be seen in wafer MH2-116 in Figure 62.

Furthermore, larger grains are observed in MH2-116 compared to MH1-33. It is clear that the nucleation of many, small grains initially have developed into large grains along the height of the ingot. Similar observations are done in the MH1 ingot, as seen from the EBSD maps in Figure 57, Figure 58 and Figure 59.

A complete collection of dislocation maps are given in Appendix D.

6.10 Precipitation investigations by microprobe

Four etched wafers from MH1 close to the top of the ingot were investigated with a microprobe to locate possible precipitates in MH1. Several precipitates, all with a rod or needle-like shape, were found in all 4 wafers. Figure 63 shows an example of an area with three precipitates, each marked with an arrow.

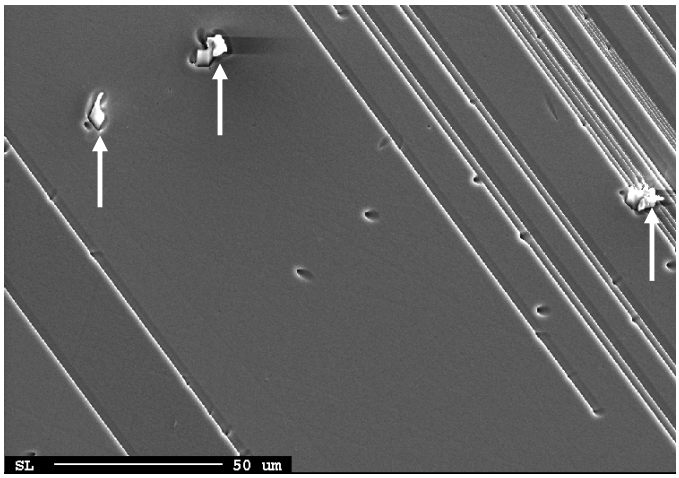

Figure 63: An area of wafer 201 showing three precipitates each marked with a white arrow

Figure 64 shows a magnification of one single precipitatied rod located at 88.9 % height. Each precipitate consisted of one or several rods in clusters. A qualitative analysis revealed that the precipitate consisted of silicon nitride and silicon carbide decorated with traces of aluminum and oxygen.

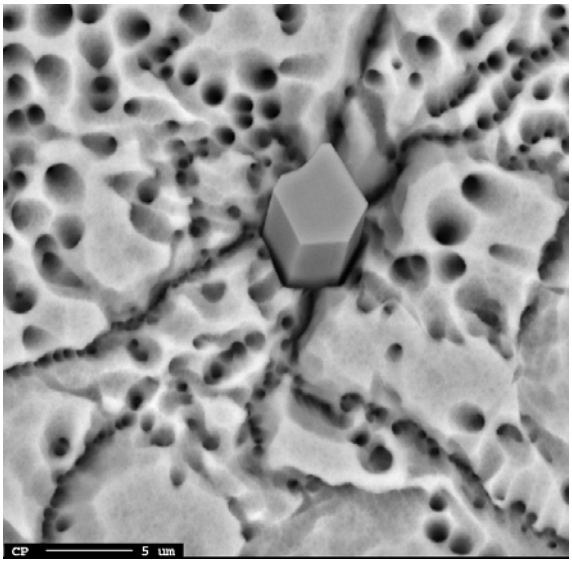

Figure 64: One of the precipitates found at 88.9 % height in a wafer from 201

A bulk analysis of an area covering about 50 µm in diameter was also performed in other regions than shown in Figure 63 and Figure 64. Silicon nitride and silicon carbide precipitates were not detected. Neither was any precipitates consisting of aluminum or transition metals.

Tables with atomic and weight percent are not included because they can only be used for qualitative analysis and for the indication of concentrations relative to each other.

6.11 Precipitation location and characterization

Investigations of precipitates included the characterization with EBIC and Auger spectroscopy.

6.11.1 EBIC

Particles or precipitates in our ingot were investigated by means of EBIC characterization in regions of the wafer with grain- and twin boundaries. We did not succeed in finding high dislocation density regions for mapping any precipitates that may be located there.

Wafer MH1-201 as well as MH2-208 was investigated, the former functioned as a "try-out" sample, while the real investigations were performed on the latter. MH1-201 and MH2-208 corresponds to 88.5 % height from the bottom of the ingot. The results from MH1-201 are not included in the thesis because the sample was exclusively employed to test EBIC and Auger as possible future characterization techniques. Furthermore, it does not give additional information that sample MH2-208 could not provide.

Due to restrictions of sample size, the wafer (MH2-208) was cut according to Figure 65, where the centre of the ingot is the top right corner opposite of the chamfered corner.

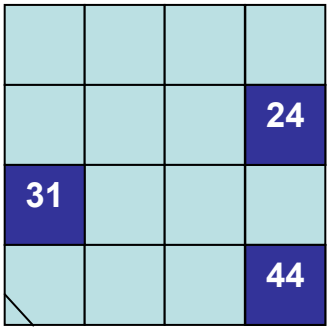

Figure 65: Illustration of the areas cut and investigated with EBIC and Auger spectroscopy from wafer number MH2-201

An overview picture of a region from wafer 208, sample 31, is shown below in Figure 66. The bright area is the top contact, while the dark spot on the right side of the contact is the silver paste used to make an electric connection to the contact. Samples 24 and 44 were also investigated, but the results are not included here because they gave the same results as with sample 31.

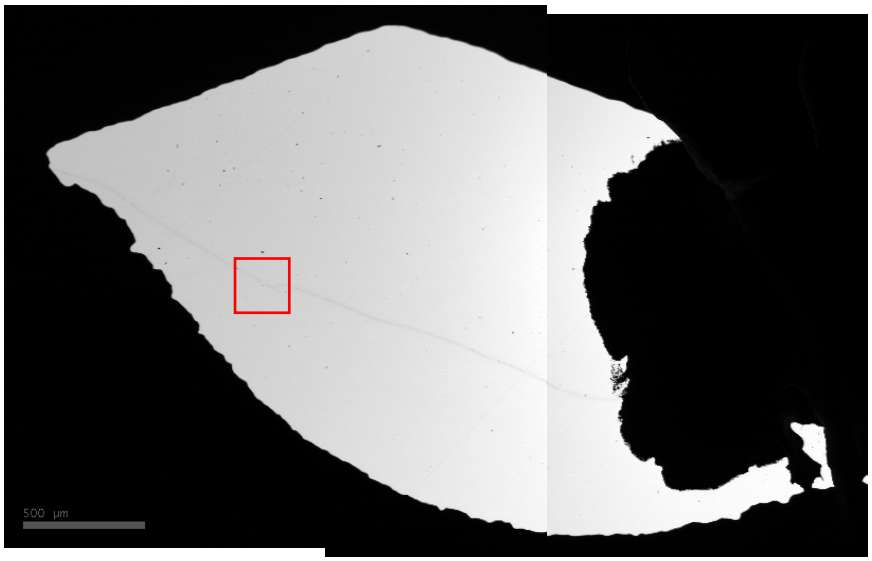

Figure 66: An overview picture of a small region covered by metal contacts in wafer 208. The red square indicates parts of the grain boundary enlarged in later pictures in order to look for particles. The scale in the bottom left correspond to 500 µm.

In order to view the whole area overlapping of two pictures were necessary. The scale in the bottom left corner displays 500 micrometers. The red square indicates the part of the grain boundary investigated further. A gradual magnification of this area is shown in the following pictures in Figure 67.

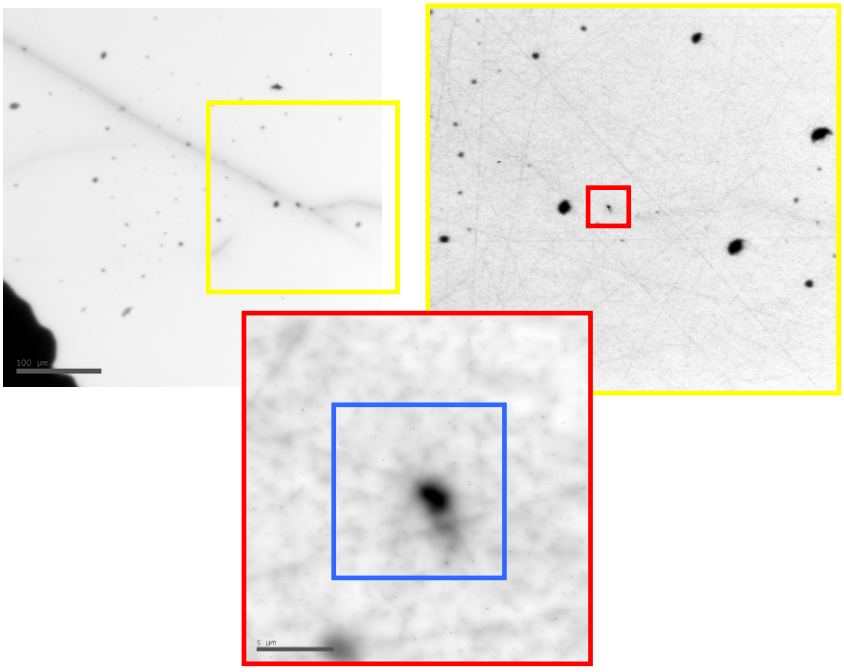

Figure 67: A gradual magnification from the top left, right and down of an area of the grain boundary. The particle seen in the bottom picture is further investigated. The scale bar in the bottom left of the picture is 100, 50 and 5 µm of the top left, top right and bottom picture respectively.

It can clearly be seen that particles or precipitates are located on the grain boundary. However, several other black dots, also resembling the particles, are distributed throughout the image. This is due to unavoidable contamination on the surface. To identify what really are particles on the grain boundary, a "depth analysis" was performed. Figure 68 displays four different depths throughout the wafer, the shallowest being 2 kV. Both SEM and EBIC pictures are included. More insight into the nature of the defects can be obtained by comparing the response at different acceleration voltages, and hence different probing depths.

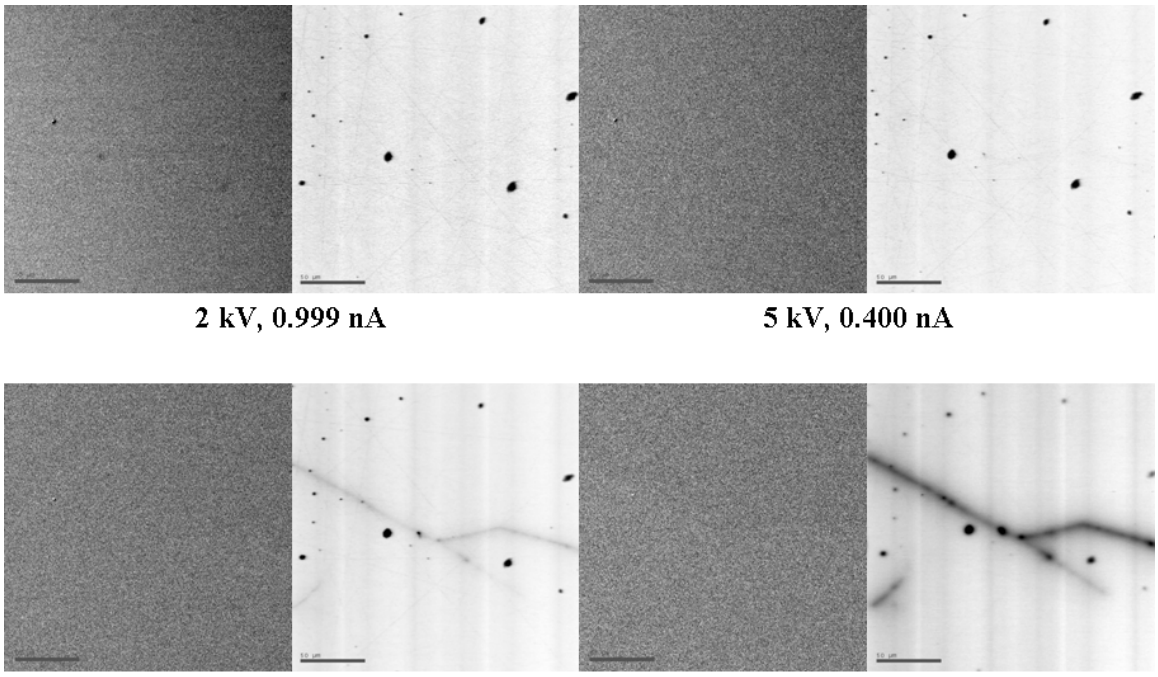

Figure 68: Depth analysis of a certain area by increasing the electron energy, displaying more features of the wafer further from the surface. The product of the current and kinetic energy are held constant. All scale bars correspond to 50 µm.

The grain boundary cannot be seen at 2 and 5 kV, and neither can the particles on the grain boundaries. At these acceleration voltages the penetration depth, based on the Grün length, is less than 300 nm. When proceeding deeper into the sample the grain boundary and some of the particles appear at 10 kV, while at 20 kV several particles can clearly be located. Operating depths at 10 and 20 kV are approximately 1 and 3 µm, respectively. The particles located on the grain boundary, which could not be observed at lower voltages, must therefore be located inside the wafer.

Repeated vertical stripes seen in the EBIC images are electrical mains noise. Furthermore, scratches in the wafer from handling and preparation are also apparent.

6.11.2 Auger spectroscopy

A characterization of the particle imaged in Figure 67 was performed in order to uncover which elements the precipitation consisted of. In total three spots were analyzed two at the particle and one outside in the grain, approximate locations are shown in Figure 69.

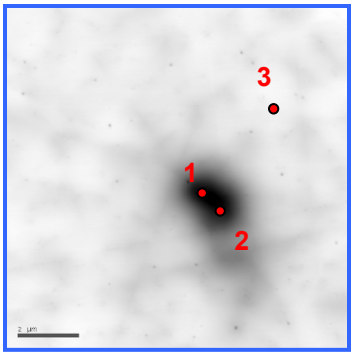

Figure 69: Displaying the three spots analyzed on and outside the particle

The full spectrum depth analysis obtained from the Auger analysis is shown below in Figure 70. A total of 46 cycles were recorded. For each cycle a thin layer (6.3 nm) is sputtered off the sample.

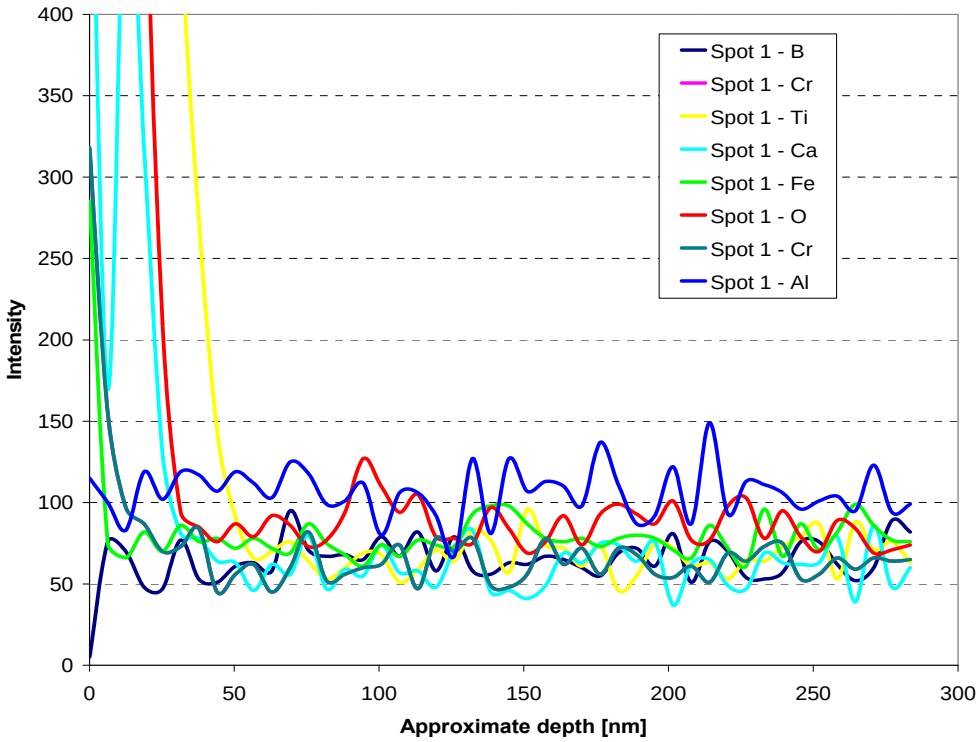

Figure 70: Auger spectrum for spot 1 showing intensity signals for each element versus the approximate depth

The kinetic energy range, where scanning occurs, is only set for certain periods corresponding to where peaks should appear from the pre-set selection of elements. It is not possible to sort out peaks when all the kinetic energies are displayed at once. Nevertheless, when magnifying a smaller range of kinetic energies and counts per second (CPS) the peaks start to appear and differences between specific depths are emphasized.

An overview of kinetic energies of peaks corresponding to specific elements is compared with the obtained spectrum. When looking closer at Figure 70 it is clear that no peaks appeared for neither of the elements chromium, aluminum, titanium and calcium. The exception is titanium contacts at the surface giving signal at shallow depths. Oxygen appeared from surface oxidation. Silicon was naturally detected at all depths, the spectrum is shown in Figure 71. Each silicon peak can be identified according to the chart incorporated in the same figure corresponding to the sole print of silicon. Peaks occurring at much lower energies can also identify silicon, but such energies are not applied in these experiments.

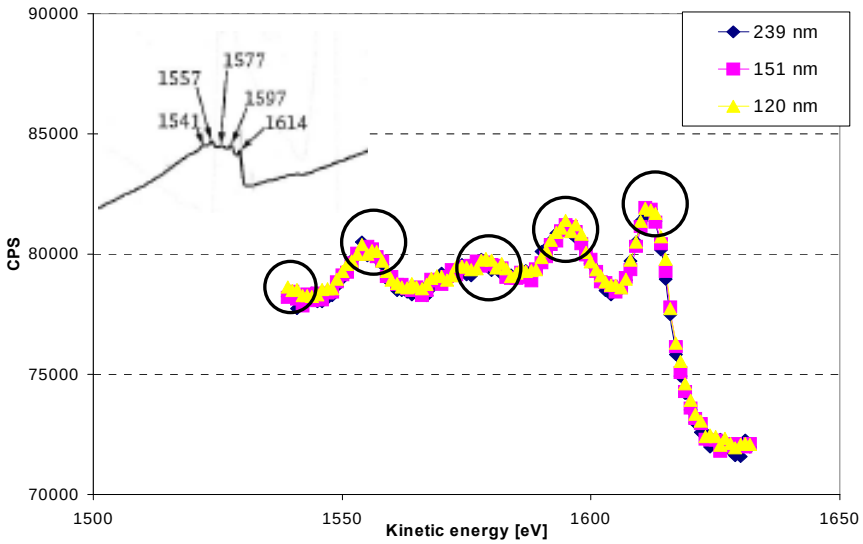

Figure 71: Identification of silicon by comparing detected peaks to a chart of kinetic energies, one for each element

For each of the three spots analyzed, given by Figure 69, spot 3 exclusively gave signal in the energy ranges considered for boron and iron, however, only for certain depths.
As seen in Figure 72, a peak appears at 221 nm with a peak energy of 160 eV, then increases in strength and shifts to a higher energy with increasing depth. This peak is tentatively identified as originating from boron, which is found at 172 eV. The boron peak drifts when going deeper into the sample. This is due to the different states boron can appear in, e.g. pure boron vs. boron oxide.

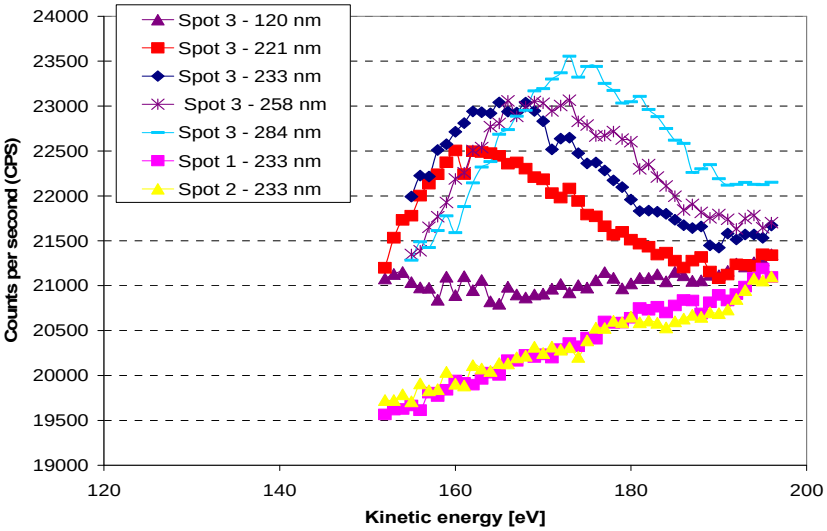

Figure 72: The boron peak for several depths at spot 3. Also included is a depth of 233 nm from spot 1 and 2

Together with boron, a "shoulder" appearing at ~600 eV is identified as iron. Iron was found at the same depths as boron and exclusively at spot 3 (comparison between the three spots are not shown) implying that a complex of boron and iron is present in the sample. The results are plotted below in Figure 73.

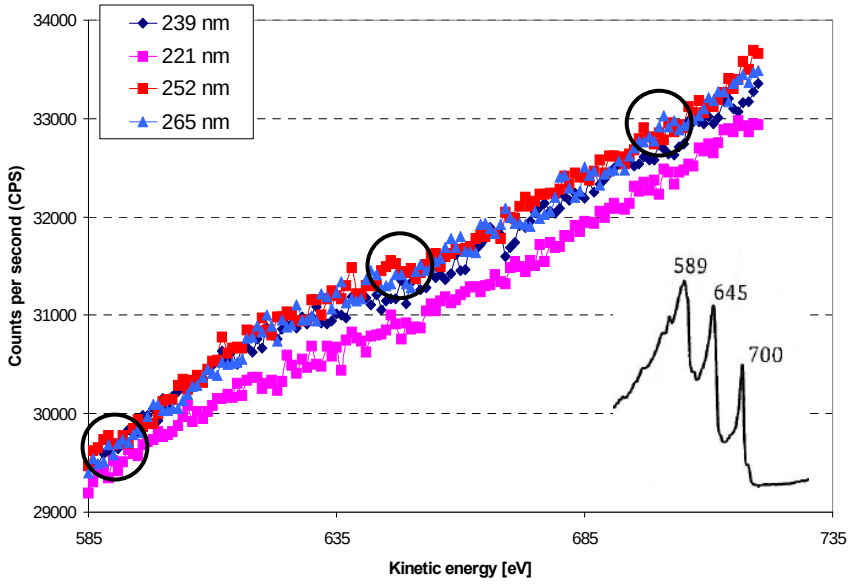

Figure 73: Indication of iron peaks as well as a large "shoulder" for spot 3

A large "shoulder" is present at 239, 252 and 265 nm, while at 221 nm no "shoulder" could be identified. Vague peaks in accordance with the chart incorporated in the bottom right corner were found, however, the "shoulder" is a stronger indication of the iron present in the sample.

6.12 Gettering

The gettering process was performed on four wafers taken from ~50, ~85, ~90 and ~95 % height in MH2 and ES2. Table 25 gives the lifetime before and after gettering. Lifetime of MH2 before gettering is measured without passivating the surface. However, because of the very low lifetimes the surface recombination does not have a major effect. The dominating factor is the bulk lifetime of the wafer.

Table 25: The average bulk lifetime before and after gettering of wafers from four different ingot heights

Wafer name	Ingot height [%]	Lifetime before [µs]	Lifetime after [µs]
MH2-122	51.9	0.31	50
MH2-205	87.2	0.18	36
MH2-216	91.9	0.26	22
MH2-228	97	0.23	3.8
ES2-200	~50 %	8.54	30

The gettering process improved the lifetimes significantly for three of the four wafers, the top wafer (at 97 % height) to a lesser extent than the others. Notice that the enhancement of lifetime in ES2 is less than for MH2 at the same ingot height.

Great improvement in lifetime is also demonstrated by lifetime maps, an example is shown in Figure 74 while the other maps are presented in Appendix C. Lifetime maps are recorded with µw-PCD.

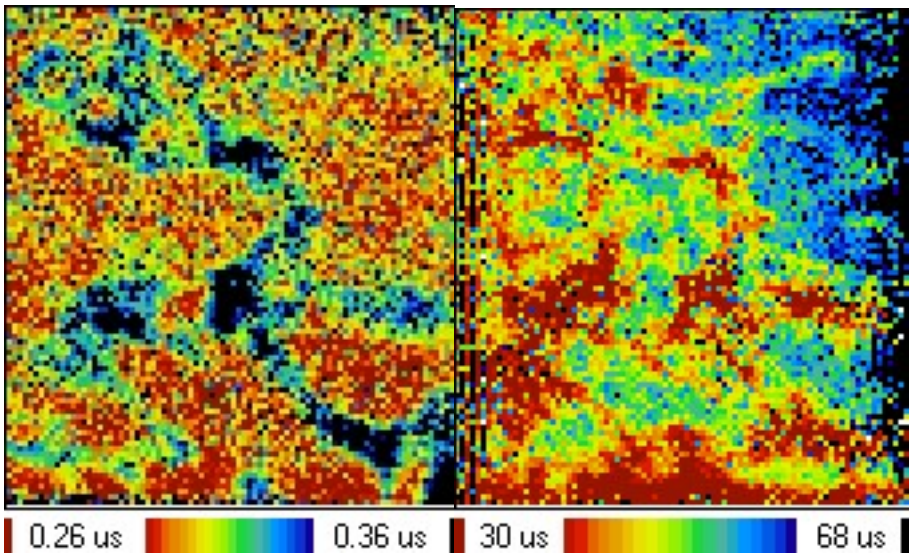

Figure 74: Lifetime maps before (left) and after (right) performing a gettering process on a wafer from ~50 % height in the ingot

As observed from Figure 74 the wafers have been subjected to a lifetime inversion after the gettering process with the best areas turning to the worst. The top right corner of the wafer provides an excellent example.

6.13 Solar cells

Solar cells were processed under standard processing conditions followed by characteristic measurements for solar cells including fill factor (FF), open circuit voltage (V_{OC}), short circuit current density (J_{SC}) and efficiency (η).

All properties are plotted as a function of cell number, where 1 is the bottom wafer of the ingot and 226 is the very top. However, cells have not been processed from all positions, but have been subjected to a selection throughout the ingot height.

The reference castings, R5 and R6, investigated by Modanese *et al.* [90] are also functioning as references for the MH castings due to a non-stable cell processing of ES1/2. The complete cell results for R5 and R6 are not provided here, but the average solar cell property for each reference is given.

Identical casting procedures to ES1/2 and MH1/2 as well as crucible and coating has been applied to R5 and R6, with the exception of crucible rotation for MH2, R6 and R5. The references has been cut to the same size and processed under the same conditions as the MH cells.

An emitter thickness of 55 ohm/sq is applied to all the cells.

6.13.1 Open circuit voltage

Below in Figure 75 the open circuit voltage (V_{OC}) is plotted as function of cell number where cell number 1 corresponds to the bottom and cell number 226 corresponds to the very top.

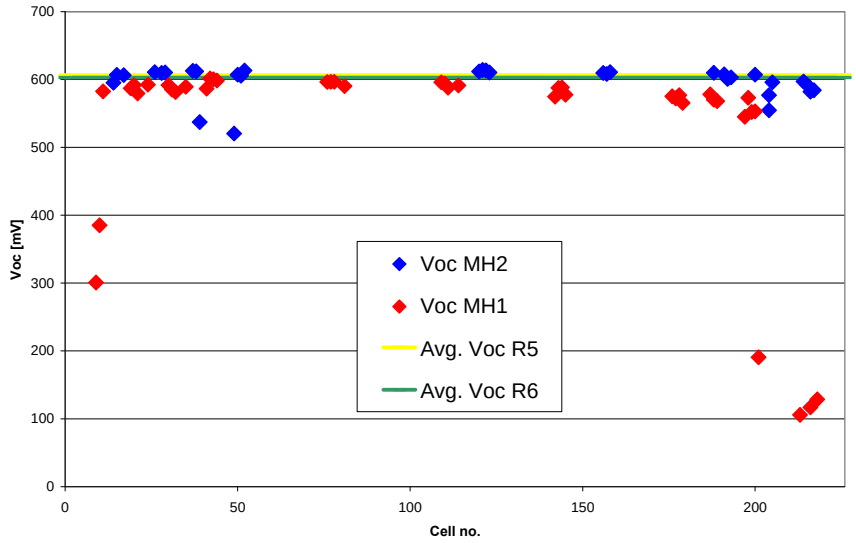

Figure 75: Open circuit voltage as a function of the cell number.

Cells close to the top and bottom of the ingot show very low V_{OC}. Almost all the cells from MH1 are located below the references. Notice the slightly overlap between R5 and R6. MH2 match the reference cells quite good throughout the ingot height and demonstrate better current densities than its equivalent ingot, MH1.

6.13.2 Short circuit current density

Figure 76 presents the data for the short circuit current density (J_{SC}) of MH1/2 and R5/6.

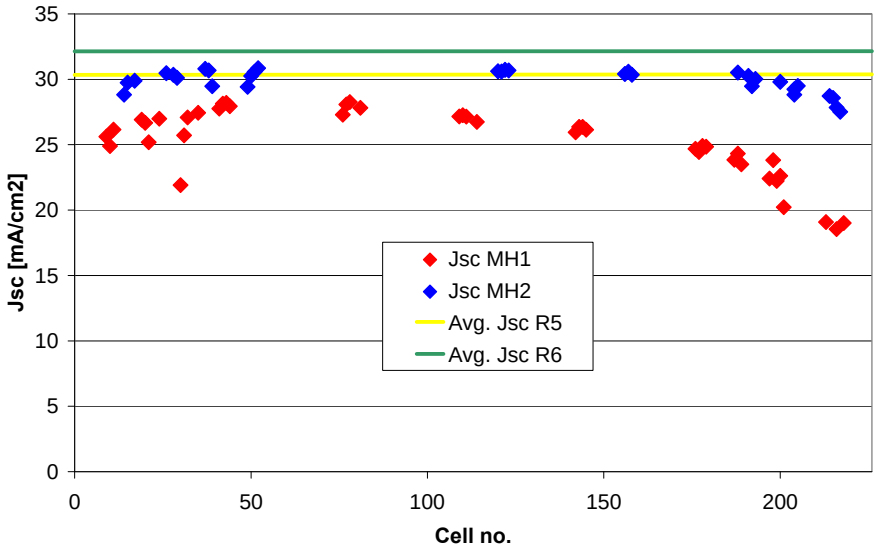

Figure 76: Short circuit current density as a function of the cell number

MH1 does also show a lower short circuit current density than MH2 along the whole height of the ingot, the deviation is even larger than observed for V_{OC}. An average short circuit current density of 32.13 and 30.13 mA/cm^2 was obtained for R6 and R5 respectively, which is far above any J_{SC} measured in MH1. J_{SC} of MH2 is significantly higher than MH1 as well as being comparable to R5.

6.13.3 Fill factor

The fill factor is a function of V_{OC} and J_{SC} and will consequently follow their trend. Figure 77 shows the fill factor throughout the ingot height.

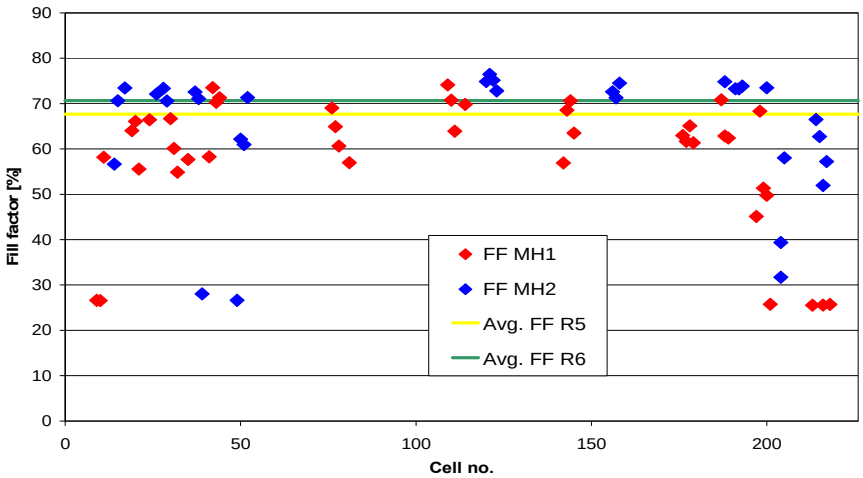

Figure 77: Fill factor as a function of cell number

MH1 can to some extent match the references. However, the fill factors of neighboring wafers of MH1 are significantly scattered. The solar cell results of MH1 are consequently unreliable. MH2 shows the same behavior at the top but otherwise a good correspondence exists between parallel cells. The fill factor of MH2 is overall higher than R5 and R6.

6.13.4 Efficiency

The graph in Figure 78 presents the efficiency obtained for the four ingots.

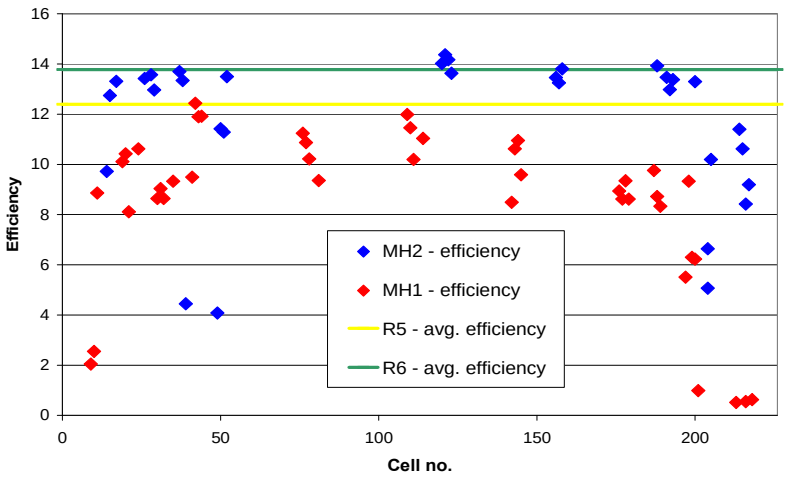

Figure 78: Solar cell efficiency of cells along the height of the ingot. Notice that R5 and R6 are overlapping

The efficiency of a solar cell is defined as the ratio of electrical output to the incident solar power utilized. The cells from the MH and reference castings have not been subjected to real sunlight, but to lamps corresponding to 1 sun. Cells at the bottom and top recorded low efficiencies. The efficiency is dependent upon all the three preceding characteristics (J_{SC}, V_{OC} and FF) and will consequently reflect their values.

Also some scattering in the efficiency occurs for MH1 and the efficiencies obtained are generally lower than both the references and MH2. MH2 demonstrates much better cell quality and good efficiencies. However, the cell processing has not been stable as mentioned in the introduction of this chapter. Discussions regarding the cell processing is given in Chapter 7. Efficiencies higher than or equal to R5/6 is observed for the cells originating from MH2.

7 Discussion

All the results presented in the previous chapter will be discussed in detail here. Possible explanations for unexpected results, differences compared to the reference ingots (ES1, ES2) and challenges with the characterization will also be included.

The two main factors contributing to degradation of the electronic properties in silicon is impurities and defects. This section provides discussions around both these aspects where the distribution of impurities is considered first followed by discussions regarding the microstructure. At last, the properties of the silicon ingots are considered with respect to the two previous mentioned factors.

7.1 Distribution of impurities

GDMS

Scale bars which show the range of error are not included in any of the graphs from the GDMS measurements. There is not done any statistical work to map the range of error for each element. However, parallel control measurements of some heights were repeated after time in both MH and ES ingots. A good reproducibility for the parallels was demonstrated within a range of ±10 %. The parallels are however not included in the figures. As the measured concentration approaches the detection limit the source of error will be greater than when measuring a concentration well into the ppm region.

Generally, very low concentrations measured by GDMS can be considered as upper limits or detection limits; hence the real content may be somewhat lower. For all GDMS measurements the background spectrum has been subtracted and peaks with large interferences in the signal have been excluded. Hence, graps should show the genuine element content in the ingot.

The conditions assumed with Scheil's equation are far from the operating conditions during solidification. Despite this, Scheil's equation gives a pointer of the distribution that can be expected. More discussions around Scheil's equation are found later.

For MH1 and ES1 block Q2 is utilized, while in MH2 and ES2 block Q4 are characterized by GDMS. Assuming that axial symmetry about the centre of the ingot occurs, should then give the same lateral distribution in Q2 as Q4.

FTIR and LECO

Several parallel measurements were performed with the FTIR and LECO techniques to identify the reproducibility. Three spots were re-measured with FTIR for all four ingots and they all demonstrated good reproducibility, with standard deviations within ±10 % for oxygen and ±25 % for carbon. The LECO instrument shows larger variation between parallels than the FTIR instrument. However, the LECO analyze a bigger cross-section area than FTIR and consequently there is room for larger fluctuations.

Notice that the LECO characterization is not performed on the same slice as FTIR (see Table 12) and might contain some extra substitutional and interstitial carbon and oxygen, respectively. It should also be noted that the carbon peak in the FTIR spectrum has more background noise and signal disturbance than the oxygen peak.

7.1.2 Donors and Acceptors

Aluminum

MH1 showed very high aluminum concentrations compared to the other ingots. The elevated concentration is present throughout the whole ingot height and is not a phenomenon occurring exclusively at the top, as shown in Figure 33.

The charge material is received in blocks from an industrial scale directionally solidified feedstock ingot produced at Elkem Solar. The blocks are crushed and put in containers with no control of which pieces are from the bottom, middle or top of the industrial ingot. Since also boron and phosphorus were present in higher concentrations in MH1 compared to MH2, the charge material used in the MH1 casting might preferably contain pieces originating from close to the top of the industrial feedstock ingot where impurities are expected to be present in higher amounts due to segregation. Alternatively, the charge material might contain aluminum rich particles or aluminum rich regions despite that the Elkem Solar process has no likely sources of this and it has not been observed in other ingots which have been subjected to the same process.

The contamination can also come from a furnace part made out of Al_2O_3. At a later time it was realized that the crucible rotation device and pedestal was broken and the crucible has been positioned closer to the top of the chamber than expected. Furthermore, plenty of aluminum can found in the crucible as aluminum oxide, as seen in Table 11. Even though no sticking was observed on the ingot it cannot be completely ruled out as possible explanation.

Aluminum is bonded substitutionally in the silicon lattice and hence does not getter as easy as the transition elements. Silicon should have a lower tolerance for aluminum than chromium and iron due to its slow diffusing properties. Hence, aluminum would probably not account for such an improvement after gettering as indicated in Table 25. Moreover, the solid solubility of aluminum has not been exceeded, even though the concentrations in MH1 approached ~10^{17} atoms/cm^3 at certain ingot heights.

According to Davis *et al.* [4] concentrations exceeding 10^{15} atoms/cm^3 will influence the solar cell efficiency. $7.65 \cdot 10^{15}$ and $1.54 \cdot 10^{15}$ atoms/cm^3 of aluminum are present at ~45 % height in MH1 and MH2, respectively. At these concentrations aluminum should have an impact on minority carrier lifetime. However, the lifetime, as seen in Figure 49, did not improve for MH2 despite lower aluminum content. This implies that aluminum does not affect the minority carriers considerably in the chromium-doped ingots.

Boron

Boron concentration is higher in MH1, while MH2 is more "normally" distributed compared to the ES reference castings and according to the calculated Scheil distribution. Compensated silicon contains in general higher concentrations of dopants. The concentration of boron in compensated SoG-silicon investigated by Dubois *et al.* [11] ($3.1 \cdot 10^{17}$ atoms/cm^3) is higher compared to the average concentration of each of the MH castings (~$7 \cdot 10^{16}$ atoms/cm^3 at 57 % height). This is in accordance with what is reported by others [8, 26]. However, the Elkem Solar feedstock must classified as a compensated material as mc-silicon contain boron concentrations typically in the order of 10^{15} atoms/cm^3 [47].

The boron concentration measured by ICP-MS is generally slightly lower than the concentration measured by GDMS. There can be several reasons for this. Variations will occur throughout the material and it depends among other factors on the dislocation density and the number of grain boundaries/grains in the crystal structure. Furthermore, the area analyzed by the two techniques is different.

An enhanced boron concentration in silicon can lead to an increasing frequency of boron-complexes, e.g. boron-oxygen, chromium-boron and iron-boron pairs. However, depending obviously on the concentration of the other element(s) involved, these complexes might already have reached a point of saturation. Hence, increasing the boron concentration might not affect the recombination activity in the material.

The position of the quasi-Fermi level is affected by the level of compensation. In compensated material the recombination strength of the B-O complexes are reduced due to the annihilation of the dopants. When the quasi-Fermi level is shifted above the defect level of oxygen, the complex is unable to form due to lack of Coloumbic forces. This is also the case for chromium- and iron-boron pairs. In MH2 annihilation of dopants is most likely occurring, while in MH1 high concentrations of aluminum will provide an excess of acceptors (boron and aluminum) compared to donors (phosphorus).

Phosphorus

The reference ingots and MH2 show lower concentrations of phosphorus compared to MH1. None of the ingots are in very good agreement with Scheil's equation. Higher

phosphorus content in the material will lead to an increased level of compensation throughout the ingot height.

7.1.3 Transition elements

Chromium

Because of excellent segregation properties most of the chromium added to the melt is found above 80 % height, as can be seen in Figure 38. For MH2 the consistency with Scheil's equation is poor, while MH1 are in quite good agreement when the dendritic region is not taken into account.

The solid solubility of chromium is $1.0 \cdot 10^{14}$ atoms/cm^3 (1200 ºC), is very close to the average concentration measured by GDMS. Precipitates should be expected to occur towards the top of the ingot.

Macdonald *et al.* [40] and Istratov *et al.* [39] reported chromium concentrations in the order of 10^{13} atoms/cm^3 in multicrystalline silicon, as shown in Table 5, while Davis *et al.* [4] claimed that chromium concentrations above 10^{14} atoms/cm^3 will have a negative impact on the efficiency. The chromium-doped castings investigated in this thesis have concentrations of 10^{14} atoms/cm^3 and higher. The chromium added to MH1 and MH2 should consequently have some impact on minority carrier lifetimes.

Iron

MH1 and MH2 contain relatively low concentrations of iron, similar to that observed in ES1. The segregation behavior of iron is not very pronounced in Figure 39 due to the concentration scale applied. It is, however, observed that most of the iron has accumulated at the top, exactly like chromium. Higher iron contents than chromium can be dissolved before super saturation and precipitation take place. The average iron concentration of ~10^{14} atoms/cm^3 is far from the solid solubility limit on the order of 10^{16} atoms/cm^3 and substantial precipitation of iron should not occur. Exceptions are close to the top.

Iron levels in the compensated SoG-silicon investigated here are comparable to the iron content in standard multicrystalline silicon given by Macdonald *et al.* [40] and Istratov *et al.* [39] in Table 5. The same tolerance as reported for chromium by Davis *et al.* [4] is also applicable to iron. The compensated material has a concentration of iron in the range where it starts being detrimental to solar cell efficiency.

Iron concentration calculations based on lifetime

The average iron concentration was calculated from the lifetime maps obtained before and after flashing (light soaking) for the slice of MH1 and ES1 in addition to a selection

of wafers. The calculations are based on distinctive lifetime characteristics originating from the electronic states of iron.

The results indicate that the slice of MH1 contain additional iron compared to ES1, even though the GDMS concentrations showed otherwise. The absolute concentrations do not correspond to the measured GDMS concentrations, which indicate that only a fraction of the total iron content is present as an interstitially specie contra precipitates. However, we did not succeed in finding any clear relation between the amount of interstitial iron contra precipitated iron in the ingots investigated. The average bulk iron content of wafers from MH2 was within the same order of magnitude as measured on the slice of MH1 (the slice of MH2 was not measured). Areas containing the highest concentrations of interstitial iron corresponded to areas with lowest obtained lifetime, a well known phenomenon observed by others [25, 54, 91].

Moreover, when recording GDMS spectra the peak estimation for iron can give concentrations considered as upper limits, as discussed previously. The average lifetime of the slice will also depend on the red zone, which contains more iron than in the bulk. In addition, other factors and/or impurity elements can be involved and affect the lifetime of the sample, hence it must be taken into consideration. Consequently this results in what the instrument register as a higher iron concentration. Particularly in SoG-silicon, where high concentration of dopants and impurities are present, the contribution from defects not related to iron can constitute some error. Thus the method might not be applicable for highly contaminated material. In cleaner silicon materials, however, this technique can suggest more realistic iron concentrations.

Iron boron and chromium boron pairs

For both MH ingots no response was observed for neither light soaking nor heat treatment, not even for a time interval up to 18 hours after processing. The reference ingots (ES) showed the same behavior and did not respond very well to neither light soaking nor heat treatment. Only some characteristic decay in lifetime was observed for ES1 and ES2 after heat treatment, however exclusively at ~50 % height. The FeB pairs can certainly be the reason for such an observation, but then it should also occur for light soaking according to literature [68, 92]. The minor change in lifetime in MH ingots is probably not due to FeB or CrB pairs. Since the lifetime is very low initially, small variations can occur between measurements which are not due to the material itself. Several factors contributing to errors in the detection of iron are considered in the previous section. Additionally, a greater chromium-iron ratio could be helpful in order to examine the boron pairs.

No difference in lifetime occurred for wafers from different heights of the ingot, in total wafers from 50, 60, 85, 90 and 95 % height were tested from the chromium doped ingots. Hence, no significant precipitation has occurred and/or the precipitates of iron and chromium are not the factor contributing to the outcome of these experiments.

Since the lifetime is very low initially the different recombination properties of the interstitial chromium/iron and their respective boron pairs may not lead to sufficient lifetime changes. Thus, the detection of chromium and iron through boron complexes cannot be performed. Alternatively, the compensation of the material has excited the quasi-Fermi level to above the donor level of interstitial iron/chromium and no Coulombic attraction occur.

Cross over point

Since no variation in lifetime was observed, the crossover point could consequently not be located for neither FeB nor CrB pairs. There are practical challenges with determining the crossover point. Lifetimes for very high (10^{16}) and very low (10^{12}) injection levels constitutes difficulties and the crossover point can thus fall outside the range of injection levels.

Several experiments reported in literature and quoted in the theoretical section of this thesis obtained results in the detection of a crossover point as well as iron and chromium-boron pairs. Even though identical experiments to those reported in the literature were performed, no results were obtained.

As already discussed, a concurrent effect from other impurities can also create difficulties with locating cross over points since several elements will interact with and disturb the diffusion of chromium/iron. Furthermore, the chromium or iron is in some cases introduced by ion implantation in amounts that are considerably lower than what is introduced into the melt of the MH castings, and thus give a higher minority carrier lifetime. In order to be able to conduct the experiments, sufficient concentrations of chromium and/or iron must be present, however without lowering the lifetime too much. A compromise between the two factors (concentration and lifetime) has to be determined in order to possibly observe any significant chromium/iron related lifetime change. Despite the low concentrations of chromium and iron, even at 50 % height, the detrimental properties of the interstitial state and the boron pair can be comparable and hence the lifetime will not vary between the respective electronic state.

The degradation of the passivation layer, which can occur at temperatures above 400 ºC, if kept there for more than 10-15 minutes, is unlikely because both times and temperatures applied in the heat treatment are not close enough.

Titanium

The concentrations of titanium detected in all four ingots are very low, with a value of 1.3 ppbw, or $3.8 \cdot 10^{13}$ atoms/cm^3 at 90 % height. However, considering at which concentration titanium starts degrading the minority carrier lifetime according to Rohatgi *et al.* [73], the concentration measured here are well above what can be tolerated.

According to Buonassisi *et al.* [74] who studied titanium-doped silicon, concentrations lower than the detection limit (of µ-XRF) demonstrated crucial degradation characteristics. If titanium were to be detrimental to minority carrier lifetime at these concentrations the ES castings would also be implicated as the MH castings. Based on this, titanium can only partly contribute to the reduction in minority carrier lifetime of the ingots.

7.1.4 Light elements

Oxygen

MH1 and ES2 contain similar, but high, concentrations of interstitial oxygen. Furthermore, the distribution of oxygen corresponds to an effective segregation coefficient larger than 1 in each and all ingots, as is also seen in other castings from the same furnace.

The similar trend of interstitial oxygen content in MH2 is observed by Kvande [25] in a polycrystalline silicon ingot cast in a high purity silica crucible. The somewhat peculiar result can be explained as a combination of diffusion from the crucible, evaporation of oxygen from the surface and the incorporation of oxygen from the atmosphere into the melt.

A graph containing all the concentrations of oxygen, both by LECO and FTIR, is shown in Figure 79.

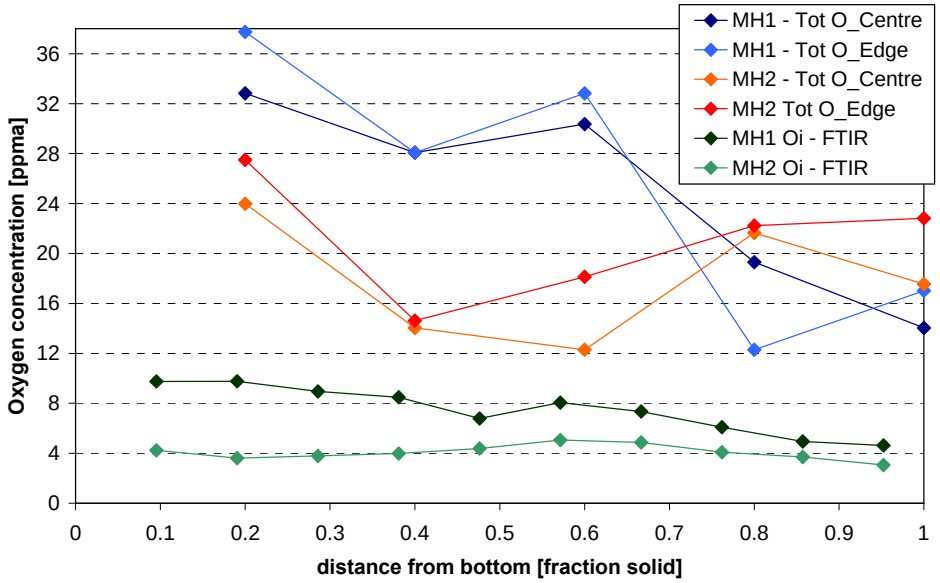

Figure 79: A collection of all the measured oxygen concentrations by FTIR and LECO of MH ingots

MH2 deviates from MH1 in that not only is the interstitial oxygen concentration substantially lower but also shows a completely different distribution. MH2 varies around an average concentration of 4 ppma. The effective segregation coefficient in MH2 is

probably closer to 1 than MH1. This diverse segregation behavior of oxygen from casting to casting is reported by several authors [22, 25, 91, 93].

LECO measures the total oxygen concentration in the silicon material. The edge and center corresponds quite well with each other along the ingot height of MH1 and MH2 in Figure 79. Furthermore, it is surprising that the edge only contains slightly higher concentrations of oxygen at several positions, as it includes the red zone where diffusion from the crucible should be more significant than at the centre. This indicates that oxygen diffusion from the crucible is not a significant phenomenon or alternatively the oxygen is heterogeneously distributed along the ingot height. The same observation is done in the project work of Nærland. [91]

If considering exclusively the interstitial oxygen concentration from the centre of the ingot, MH1 contains twice the amount of MH2. Distinctions between the total and interstitial oxygen is significant and indicates that oxygen consists in other electronic states as well as an interstitial element. Since MH2 has such low interstitial oxygen content compared to MH1, it can be assumed that more oxygen is present as precipitates in MH2. However, since also the total oxygen concentration, shown in Figure 79, is lower than in MH1 this cannot be the case. Furthermore, the solubility limit of oxygen (20 ppma [94]), is barely exceeded in MH2 and oxygen precipitation should not be extensive.

Interstitial oxygen atoms dissolved in the crystal lattice do not influence the electrical properties of silicon considerably. However, if present as oxygen precipitates the detrimental effect is considerably greater [93]. Large differences occur in MH1 for interstitial and total oxygen content, thus oxygen might have a substantial impact on the electrical properties in this ingot.

Moreover, the difference in interstitial and total oxygen concentration can be a result of the ingot region analyzed, as mentioned previously. FTIR measurements are obtained from the central slice of the ingot while the LECO analyses are performed on slice E cut further towards the edge (see Figure 28). It is expected that higher oxygen concentration is found in the edge regions. However, this alone cannot account for the difference between interstitial and total oxygen content.

Carbon

The distributions and concentration ranges of substitutional carbon are almost identical for MH1 and MH2. Furthermore, the chromium-doped MH castings are lower in substitutional carbon than both the reference ingots (ES), as shown in Figure 46. Back diffusion occurs at the top of the ingots. Figure 80, below, included all the carbon concentration measurements from FTIR and LECO.

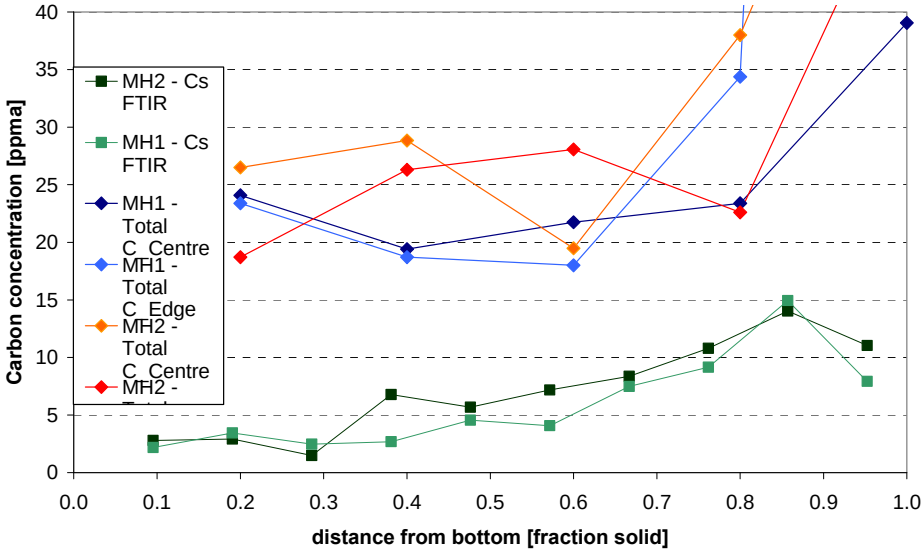

Figure 80: A collection of all carbon concentrations measured by FTIR and LECO

There is fairly more carbon in the samples than the substitutionally bonded specie. In the middle (fraction solid equal to 0.5) of MH1 the corresponding total carbon and substitutional carbon concentration is 21.7 ppma and 4.5 ppma, respectively. The excess carbon must be found as precipitates or complexes. As mentioned in the previous section about oxygen, the FTIR and LECO samples are taken from different parts of the ingot. This can thus contribute some to the difference between the substitutional and total carbon content.

An excellent agreement exists between both MH ingots in the LECO characterization, which were also the case for the FTIR concentrations. Increasing deviation between centre and edge occurs when moving towards the top of the ingot. At the top of the ingot the carbon concentration of the edge is substantially higher than in the centre. The silicon carbide precipitates detected at the surface of the ingot is probably the main contributor to this.

Furnace environment will have a great impact on the substitutional carbon concentrations in the melt. Several furnace parts are made of graphite which reacts with SiO to form CO-gas [94]. The CO-gas can be incorporated into the melt enhancing the oxygen and carbon content. However, since low carbon concentrations are present despite the high oxygen concentration in MH1, the environmental atmosphere impact seems to be insignificant.

7.1.5 Segregation behavior

The three factors contributing most to the shape of the segregation profile for a given element during casting are the type of growth (dendritic or directional), the growth rate and the crystallization time. The effective segregation coefficients calculated are within

one order of magnitude from the equilibrium coefficient, the exception is phosphorus. Smaller deviations occurring for the other elements can also be reflected in their respective distribution through the ingot height.

The concentrations measured in MH2 were the basis for the calculated effective segregation coefficients. This is due to the fact that there is generally a higher concentration of boron, phosphorus and aluminum present in MH1, which are not distributed somewhat like expected, i.e. the segregation behavior deviates from the other ingots as well as Scheil's equation. In addition MH1 have a larger dendritic region where concentrations can deviate significantly from what is calculated by Scheil's equation as well as no crucible rotation which may influence the convection of the liquid phase.

Kvande [25] reported an effective segregation coefficient for iron equal to $2 \cdot 10^{-5}$. The calculated k_{eff} for iron in the chromium-doped castings is in agreement (same order of magnitude) with this value. Geerligs *et al.* [41] estimated the effective segregation coefficient of aluminum and boron to 0.007 and 0.83 respectively. For aluminum this differs by one order of magnitude compared to what was calculated for MH2, while k_{eff} for boron is the same. The calculations performed for k_{eff} of boron and phosphorus in this thesis did not include the two top points in the dendritic region, due to non-representative segregation behavior.

The calculated effective segregation coefficient for phosphorus is far off its equilibrium value. For phosphorus, k_{eff} is larger than k_0 and more phosphorus must be left in the solid phase than predicted by Scheil's equation (Figure 41). For ES1 and ES2 the same segregation behavior occurs. During solidification local supersaturations might have occurred making some phosphorus precipitate delicately. Alternatively, complexing of phosphorus with other elements has prevented its segregation. It is impossible to designate the incongruous segregation behavior to one specific feature since so many factors are involved.

When calculating the equilibrium Scheil distribution for each element, the equilibrium segregation coefficient constitutes parts of the expression; the complete equation is given in Chapter 2.3. Several assumptions are taken into account when applying the equation; complete miscibility in the liquid phase and no diffusion in the solid state being the most important ones. Neither of these are assumptions are applicable to real castings. The miscibility is most likely not complete and can vary from casting to casting depending on crucible rotation/stirring and convection in the melt. There is a significant solid-state diffusion from the crucible and coating as well as back-diffusion from the top of the ingot back into the bulk. In addition, k_0 is based on the fact that only two elements, silicon and an impurity, are present, as shown in Figure 3 in Section 2.3. Of course in reality, and especially in SoG-silicon, this is not true. Several impurities and dopants in high concentrations will affect the situation, and some deviation from Scheil's equation is consequently not surprising. In reality the growth rate and melt flow conditions will also change and thus the effective segregation coefficient will vary during the solidification.

The vertical position of the sample in the ingot can have a variation of about ±0.5 mm due to grinding and sputtering of the sample after measuring height prior to characterization. However, it cannot contribute to incorrect calculations.

The chromium, iron and aluminum content in MH2 are very low below 60 % height, and at least for iron and chromium the measured content can be considered as the detection limit. Including all heights in the calculations can contribute to source of errors. However, when calculations incorporated concentrations exclusively above 60 % height, the results are identical to calculations also including concentrations below 60 % height. Consequently, this factor does not constitute significantly errors.

7.1.6 Majority carrier type transition and compensation level

Due to the different segregation coefficients the level of compensation along the ingot height will not be constant. A majority carrier type transition, i.e. from p- to n-type, is dependent upon the initial concentrations of all donor and acceptor species [10]. The transition from p-type to n-type silicon was predicted to occur around a solid fraction of 0.95 based on the initial concentrations measured on feedstock and Scheil's equation. However, the true situation, based on the GDMS measurements of boron and phosphorus content, did not coincide with the one predicted by Scheil and no transition occurred in any of the MH ingots. There can be several explanations for this.

First, the sufficient concentrations for a transition might not be present in the feedstock material. However, since the castings of ES1 and ES2, with same feedstock material, obtained a transition, there should be satisfactory dopant content. The equilibrium segregation coefficients applied in Scheil's equation take several assumptions into account that are not fulfilled during solidification. Hence, the effective segregation coefficients are not equivalent to the equilibrium value, as seen in Table 17. Especially for phosphorus some deviation occurs between k_{eff} and k_0, as discussed in Section 7.1.5, which lead to a less steep segregation and no transition in MH2. High concentrations of aluminum in MH1 contribute significantly to the total acceptor concentration and hence the compensation level consists of the concentration of boron plus aluminum minus phosphorus ([B]+[Al]-[P]).

Notice that samples measured by GDMS covers only a small area and certain heights of the total ingot and local transitions are thus not detected. Furthermore, since dendritic growth is occurring at the top of the ingot the GDMS concentrations of boron and phosphorus at this ingot height can be subjected to large errors that do not reveal possible p- to n-type transitions.

7.1.7 Precipitates

Microprobe analysis

Large precipitates consisting of mostly silicon nitride were detected by a microprobe. The precipitates were located both in bulk phase and at defects. Silicon nitride precipitates are commonly observed in silicon ingots due to the dissolution and diffusion of silicon nitride coating during the casting process. At the ingot height where the wafers were taken several types of particles and precipitates consisting of transition elements and aluminum were expected to be present, at least at grain boundaries. Such precipitates could, however, not be observed. It was not possible to distinguish any particles at the grain boundary from the grain boundary itself. In addition, the detection limit of the EPMA instrument was much higher than what was expected to be found for the respective impurities, the detection limit are as follows:

- Al: 117 ppm
- Cr: 33 ppm
- Fe: 26 ppm

EBIC

The extent and distribution of particles was to be compared in regions with three different crystal structure features; grain boundaries, twin boundaries and areas with high dislocation density. However, areas with high dislocation density could neither be seen in SEM nor EBIC images. There could be several explanations. The area investigated (sample 31 of wafer MH2-208) does not contain any high dislocation areas, as can be seen from the dislocation density map of MH2-210 (Figure 62). Otherwise, if an area with many dislocations is present in the sample investigated, the metal contacts have to be applied exactly on the specific area in order to image it. Temperature will also influence the displayed image and by executing the experiments at low temperature the dislocations can be revealed easier.

Precipitates or particles with high recombination activity can be clearly seen from several EBIC images. By increasing the electron beam energy gradually several more particles appear, which supports the hypothesis that this is actual structural characteristics in the wafer. The less electric active areas could have been point dislocations, but it is less likely that only very few are present in the same area and that they appear exclusively on grain boundaries.

Different contacts have been applied to sample 24, 44 and 31, the two former ones having aluminum contacts while the latter had titanium contacts. The aluminum contacts formed a better diode than the titanium contacts, with a larger recombination current on the sample with titanium contacts. This can be due to differences in the contacts, or it can be related to more defects in the areas covered with titanium contacts. As of yet we do not have enough statistics to tell. Larger recombination close to the surface (not surface recombination) was observed on the samples with titanium contacts. This might be due to the diffusion of aluminum extending deeper into the wafer than titanium.

The diffusion of other elements into the wafer must also be taken into consideration. When cutting the wafer into smaller samples with a metal blade saw, fine-grained dust originating from the blade might be left on the wafer surface. When applying metal contacts the metal atoms can diffuse into the material during firing in addition to the metal atoms from the cutting blade. The extent of such diffusion is not known and since the firing process has a very slow cool-down time the atoms can diffuse far into the material. Consequently, it will not be possible to discriminate between precipitates originating from the casting process and precipitates induced later in the process.

Auger

No traces of titanium (other than the contact), aluminum, calcium or chromium was observed at any of three spots analyzed. Since neither aluminum nor titanium is detected except than close to the surface, the diffusion from the metal contacts into the sample is probably not critical for the measurements.

Oxygen was detected at all three spots. However, the oxygen is a result of the environment oxidizing the surface and it is impossible to differentiate between oxygen actually present in the bulk of the sample versus oxygen at the surface. Strong indications supporting these observations were seen in the Auger spectra where oxygen do not appear for spot 1 instantly after sputtering, but can to some extent be detected in spot 2 and even more in spot 3.

Boron was present exclusively at spot 3 and at depths as far down in the sample as analyzed, as shown in Figure 72. Several elements have peak energies in the same range as boron, among them Cl, Mo, and heavier elements. One extrinsic source could be the gold wire used to connect the sample. During sputtering, gold could be deposited on the sample surface. However, the peak was only found at one location and seems to increase with sputtering time. This is unlikely because the extension of the area analyzed is very small compared to the gold thread. Thus, the gold would interfere at all three locations. Other heavier metals can also interfere with the boron peak.

Iron was also identified, however, only at depths also containing boron. A magnified spectrum of the kinetic energies where iron peaks appear are shown in Figure 73. For depths corresponding to 239, 252 and 265 nm contours of iron peaks are obtained in the Auger spectrum in addition to a larger “shoulder” extending over ~30 eV. At 221 nm on the other hand, no iron peaks or “shoulder” was detected. There are quite clear indications of the existence of a boron-iron complex, e.g. FeB pairs. Not only do they appear in the same spot, but also exclusively at the same depths in the sample.

No signal from the transition elements was expected from spot 3, since it is located outside the particle that was analyzed. Some explanations can be provided to account for the observation. As the analysis itself take time the preset sample position might drift during the measurements and hence spot 3 might actually be located at the particle. If the sample has not drifted the Auger characterization has most likely detected dissolved iron

and boron in close connection. Another possibility is the existence of nanoprecipitates consisting of iron and where boron comes from the surrounding areas. However, it is peculiar that only iron should be present in such a nanoprecipitate since the chromium content is at least equivalent to the iron content. In addition, the nanoprecipitate should occur at low energy sites as grain boundaries or regions rich of crystal defects.

7.1.8 Summary

Davis *et al.* [4] did not account for the interaction between several elements nor the defect levels introduced by complexes (e.g. CrB pairs), and an comparison between Davis *et al.*'s study and the Elkem Solar feedstock must simply be applied as guidelines.

Even though the ingots contained quite low concentrations of chromium (50 % height), iron and titanium, these impurities can still have a significant impact on minority carrier lifetime. If present as dissolved species within the grain their point defect range extends much further than when found as precipitates. Moreover, if the area analyzed by GDMS does not embrace a grain boundary or other defects decorated with precipitates, the concentration measured is only a perspective of the impurity content of the grain. This does also concern the p- to n-type transition that did not occur, where measurements within the dendritic region might not be representable for the real concentrations present.

Several sources contribute to the final distribution of oxygen and carbon within the ingot. Diffusion of oxygen from coating and crucible, segregation during solidification, the evaporation of SiO gas off the melt and the incorporation of CO from the atmosphere are the most important ones [25]. In total four ingots were investigated regarding oxygen and carbon concentrations. No consistent trend could be found between the distribution of interstitial and total oxygen or substitutional and total carbon. The lack of coherence between high/low oxygen and high/low carbon content as well as distribution in the different ingots cast in the same furnace leaves the work inconclusive. There can be found no correlation between the concentration of light elements and a specific source of origin.

MH1 contain high concentrations of dopants (especially Al) as well as oxygen. This will probably lead to some degradation of the electronic properties in silicon, however, the effect from each impurity cannot be separated from each other.

Several precipitates detected by EBIC were analyzed by Auger spectroscopy. Traces of boron and iron could be found at certain locations and depths, otherwise no elements except from silicon were detected. Since nitrogen was not among the elements analyzed for in Auger spectroscopy, the large precipitates can be of silicon nitride, as observed in the microprobe.

7.2 Microstructure

7.2.1 Casting

Due to very high concentrations of aluminum in MH1, it was decided to cast a parallel casting to MH1, called MH2. MH2 is more representative with respect to impurities present in SoG-silicon and gives a more reasonable perspective of the chromium doped material. One reference ingot would in principle be good enough for comparison. However, this master thesis is part of a larger project, and the reference castings for the chromium doped ingots are under investigation by Modanese *et al.* [90].

A slightly longer solidification time was observed for MH1. MH1 also changed into dendritic growth earlier than MH2. In general, MH1 contained more impurities than MH2, namely boron, phosphorus, oxygen and aluminum, which can account for the earlier transition in growth morphology. Additionally, the furnace settings did not correspond to the parameters set in the software, which leads to a higher pedestal and crucible position in the furnace during the casting of MH1 which are more likely the reason for the dendritic growth.

Dendritic growth occurred at the surface in the centre of the ingot, which means that the outer circumference had solidified first and hence been able to maintain its planar solidification front. The transition from directional to dendritic has occurred exclusively for the last melted phase. Such a dendritic growth is observed in most of the lab-scale ingots produced in the same furnace and is consequently due to process conditions and not the material itself.

In contrast to MH1, crucible rotation was applied to MH2 during solidification. The crucible rotation ensures refining conditions closer to the equilibrium situation given by Scheil's equation and hence some differences can occur due to this.

7.2.2 Grain orientation

The grain orientation and the number of grains and twins are dependent upon the nucleation and growth conditions during the early stages of solidification.

The grain orientation maps look normal for the three wafers compared to maps obtained from the reference ingots as well as earlier castings in the same furnace [22, 23, 25]. Many small grains are present at the beginning of the solidification. When growth proceed grains grow at the expense of others, and twins are developed. An example is the bright green grain shown in Figure 81 above and to the right of the centre of the wafer which decreases in size when moving from the bottom to the middle of the ingot. Towards the top of the ingot the structure is disordered and at the very top a transition

from directional to dendritic growth has occurred for MH1 due to furnace conditions discussed in the previous section.

For MH2 no EBSD maps were recorded because of a broken instrument. However, by looking at the wafers from bottom to top the same characteristics is observed as for MH1.

At the bottom MH1 seems to have four main growth directions, which all have their origin in the centre of the wafer, as marked with the white stippled lines in the map in Figure 81. Whether this is representative or not for wafers from other parallel lateral positions is not know.

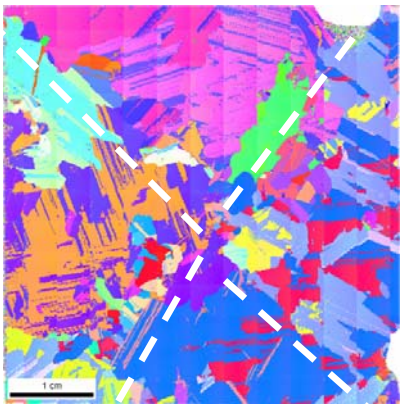

Figure 81: EBSD map of wafer from the bottom of ingot MH1. Four main growth directions are marked with white stippled lines.

A transition from directional to dendritic growth is about to happen at the uppermost characterized wafer as the solidification approaches the very top due to casting conditions. Furthermore, MH ingots contain a larger number of grains compared to the reference ingots. Another feature of the reference ingots is that a higher fraction area is covered by twins than in the MH castings, an example of wafer ES1-200 (88.5 % height) is shown below in Figure 82.

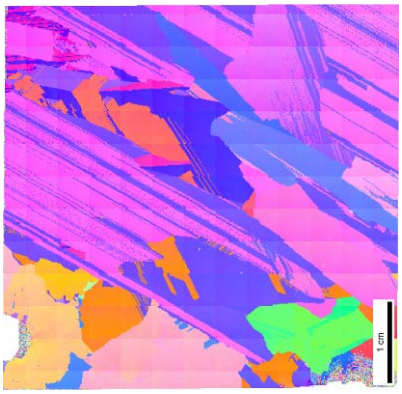

Figure 82: EBSD map of wafer from ES1 close to ~90 % ingot height

What is somewhat peculiar is that the structure throughout MH2 is divided in two. As can be seen from Figure 60 half the wafer, closer to the centre of the ingot, is dominated by large grains and twins while the other half contain numerous small grains.

7.2.3 Dislocation density

The overall density of dislocations for MH1 and MH2 is quite ordinary distributed with both areas of high (> 10^6 cm^{-2}) and low (< 10^5 cm^{-2}) density. Compared to MH1, MH2 contain considerably more dislocations throughout the ingot, as can be seen in Figure 62. ES1 (not included in the results section) on the other hand is extensively twinned along the ingot height and with few dislocation clusters even towards the top. Ryningen [22] observed that ingots with smaller grain size can contribute to more dislocations due to grain boundaries acting as nucleation sites, as is the case in the MH ingots. In addition, temperature conditions and the coating quality at the point of nucleation are important for the dislocation distribution [22].

Cuevas *et al.* [48] observed the following dislocation density in multicrystalline silicon wafers:

Ingot region	τ_{eff} (pre-gettered) [µs]	Dislocation density [cm^{-2}]
Top	1	$6 \cdot 10^6$
Near Top	15	$6 \cdot 10^5$
Centre	35	$5 \cdot 10^5$
Bottom	2	$1 \cdot 10^4$

This is comparable to the dislocation density of the MH castings. A comparable increase of dislocation density is observed for the MH ingots.

7.3 Properties

7.3.1 Resistivity

Due to very high concentrations of aluminum, an acceptor in silicon, the resistivity in MH1 shows very little trend variation. The resistivity of MH1 is constant around 0.5 ohm·cm with more scatter close to the top of the ingot, as can be seen in Figure 54. Aluminum is however not a significant contributor to the resistivity in MH2, the increase can be attributed to higher boron and phosphorus concentrations at the top as the Elkem Solar feedstock is a compensated material, i.e. decrease of net carrier concentration occurs. The same is observed for other castings with Elkem Solar material [7].

7.3.2 Minority carrier lifetime

Impurities and crystal defects are the two main reasons for degraded electrical properties in silicon. Hypothetically the difference between the ES and MH castings is exclusively the chromium. However, the real picture is somewhat different with other elements and the grain structure interacting, where each and one must be taken into consideration to understand the complete impact of chromium. Several factors that can cause low lifetimes will be discussed in the following section.

Effect of impurities

In comparison, the lifetimes of ES1 (15 µs) show significantly higher lifetime than MH2 (0.51 µs). Even though the interstitial oxygen and aluminum content in MH2 is lower than in MH1, the lifetime seems to be unaffected. Despite that ES1 contains comparable oxygen contents to MH2, both interstitial and total, the lifetime is considerably higher in the former. Hence, precipitated oxygen is either not widespread or the precipitated specie does not possess as strong recombination properties as reported by [93].

The presence of B-O complexes is known to cause degradation of lifetime. Especially in MH1 where both oxygen and boron concentrations are high, the conditions for constituting such a complex is appropriate. The complexes are induced by light, only 4 minutes of illumination with 1 sun is necessary. However, the degradation properties are recovered with a short anneal above 200 ºC, as reported by several researchers [11, 52]. This means that if the B-O complexes had a significant effect on lifetime in MH1 and MH2 it should be observed in experiments where lifetime is measured both after light soaking and after heat treatment. Since no variation in lifetime was obtained for neither MH1 nor MH2, the B-O complexes cannot be the main cause of lifetime degradation. Another issue to discuss is the Al-O complexes that introduce a deep-level defect. It is not known whether the Al-O complex behaves the same way as B-O, but it is known that aluminum concentrations above 10^{15} atoms/cm^3 induce Al-O defect centers (if O concentration is sufficiently high) [71]. This is the case in MH1, but not in MH2. Hence, a difference should be evident between MH1 and MH2 if this is a dominating effect.

If titanium is contributing significantly to the degradation in lifetime, it will also have the same effect on the reference castings. Hence, titanium can only to some extent be detrimental to ingots investigated in this thesis. The dopant concentrations are similar for MH and ES ingots, and should thus not affect the minority carrier lifetimes on one or the other more significantly. The same is true for the iron content. As reported by Davis *et al.* [4], iron concentrations exceeding 10^{14} atoms/cm^3 (equivalent to ~4 ppbw) will be detrimental to the minority carrier lifetime. Except for bottom and top of the ingot, the iron concentration is below this limit and should not have a substantial impact on the core parts of the ingot.

The main factor of low solar cell performance observed by Kvande [25] in an iron doped (53 ppmw) ingot, was the reduced bulk diffusion length. The lifetime of as-cut material

was in the range of 1-2 µs for [Fe] of $5 \cdot 10^{13}$ atoms/cm^3. It can be assumed that this is applicable to the MH castings as well, containing iron concentrations in the order of 10^{12} atoms/cm^3 based on µw-PCD measurements and ~10^{13} atoms/cm^3 based on GDMS measurements. Since at least ES1 contain the same levels of iron as MH1 and MH2, iron contaminations must affect the lifetime similarly in all three ingots. The very low lifetimes in MH ingots cannot be caused entirely by iron as average lifetime in ES1 is more than one order of magnitude larger.

Poor lifetime is observed for both chromium doped ingots, as shown in Figure 48 and Figure 49, which strongly indicates that chromium impurities are detrimental to the electrical properties of this SoG-silicon material. An EU-project, FoXy (SES6 – contract no. 019811), doped an equivalent sized ingot with 20 ppmw chromium and observed bulk lifetimes below 1 µs. Previous discussions also indicate that chromium has a strong recombination activity lowering the lifetime.

Effect of crystal structure

As seen in Figure 83 for MH1 and Figure 84 for MH2 the grain orientation and dislocation density map of correspond quite well with the lifetime map obtained by µw-PCD. Notice that the lifetime map is a mirror image of the other two images. For both ingots the high lifetime regions correspond to surprisingly enough highly dislocated and disordered areas, while the grains and twin boundaries seems to enclose the lowest lifetime. Identical observations were done by Nærland [91]. She studied, among others, the lifetime and grain orientation of the red zone, the bulk and a transition zone between the two former regions. Red zone areas with twin boundaries corresponded to low lifetime, while regions with enhanced lifetime were constituted of high dislocation density. However, the transition zone and bulk material showed the expected behavior with high dislocation density areas being analogous to the lowest lifetime. A reasonable explanation can be provided for Nærland's observation as well as ingot MH1 and MH2. Impurities in large grains and impurities surrounding twin boundaries have not been exposed to "sinks" during post-solidification annealing. Internal gettering of impurities, where the impurities have precipitated on grain boundaries and dislocations, has left the closely surrounded area much less contaminated. Large grains and twins have not been subjected to this and consequently the lifetime is lower in these regions.

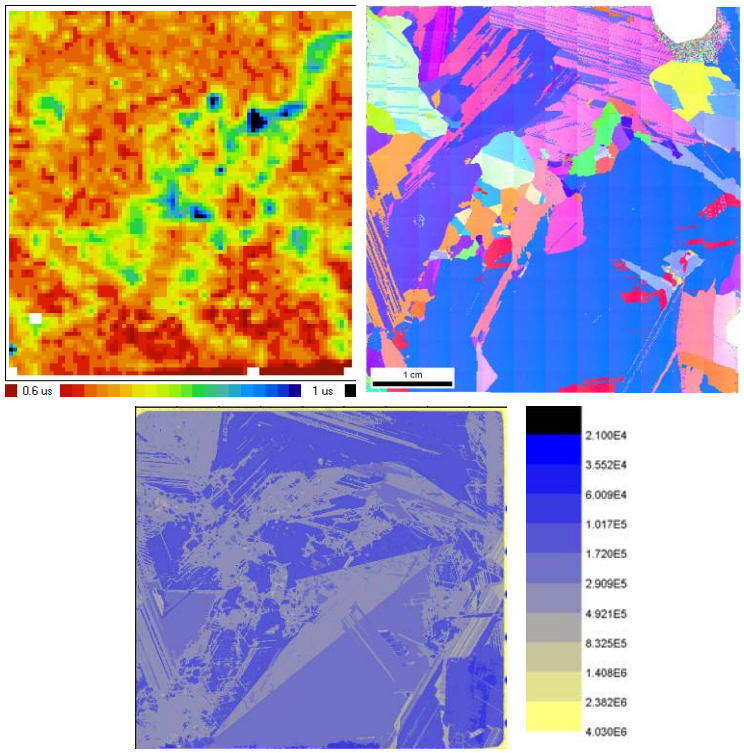

Figure 83: Wafer MH1-116 characterized by µw-PCD (top left), and EBSD and PVScan conducted on wafer MH1-112 (top right and bottom, respectively). Notice that the lifetime map is a mirror image of the other two.

White arrows are indicated on the optical image of MH2-125, Figure 84. The arrows indicate the high lifetime regions of the corresponding lifetime map.

Large grains and few dislocation clusters are desirable in a silicon ingot with minor contaminations. In SoG-silicon where the total concentration of impurities are higher, low-energy precipitation sites must be located within a reasonable diffusion length from where the impurities are distributed. If the grains become too large the impurities might not be able diffuse to the precipitation sites and hence low lifetime grains are the result. In the ingots investigated here this has not been the case. Based on observations done, it does not seem like solely the grain structure contribute significantly to degrading the minority carrier lifetime in MH1 and MH2.

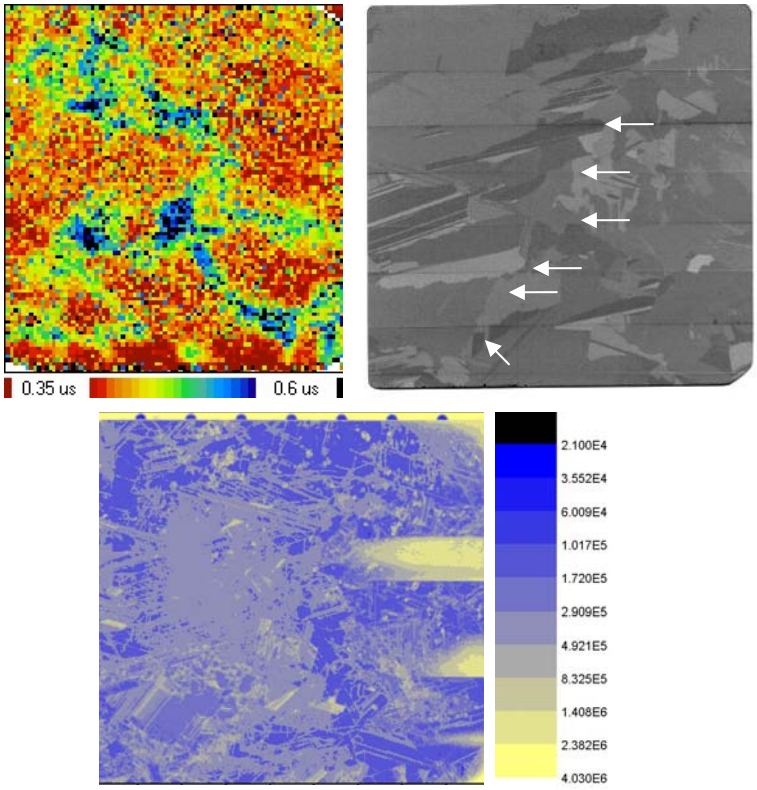

Figure 84: Lifetime map of MH2-120 recorded by µw-PCD (top left), optical image of wafer MH2-125 (top right) and dislocation density imaged by PVScan (bottom) of wafer MH2-116. Notice that the lifetime map is a mirror image of the other two.

Comparison of lifetime mapping by µw-PCD and CDI

The lifetime recorded by µw-PCD and CDI are low in both maps but do not correspond well, as can be seen from Figure 50. The CDI measurements have an uncertainty that will increase as the lifetime approaches low values (< 3 µs). The negative values of the CDI map are due to a non-uniformity correction which has probably not been calibrated correctly (for a black body). Furthermore, the absolute value of the lifetime obtained by CDI cannot be trusted due to the following factors.

It was recently brought to attention that the wafers should be polished prior to passivation to eliminate substantial surface structure. The wafer characterized in this work was not polished because the effect of preparation was not known at this time. Additionally, the calibration of the CDI is performed on a polished wafer. The influence of surface structure can be understood by looking at the topographic image of the identical wafer, also included in Figure 50. The topographic structure coincides with the lifetime map of CDI, while there is little correlation between the lifetime maps from the two techniques of CDI and µw-PCD. Due to the strong influence from surface structure, further investigations were not conducted. For a complete understanding of the variations between the two techniques polished neighboring wafers from the same block should be passivated in the same batch. Then, the distinction of good and bad areas as well as comparing wafers relative to each other can be made.

For the μw-PCD wafers originate from block Q3, while the wafers employed in CDI are from block Q1. The crystal structure can be different in the two blocks, also affecting the lifetime obtained. Furthermore, the passivation process applied to the wafers from each block is not identical (Q1: Fraunhofer ISE, Q3: IFE). Due to time limitations it could not have been done differently at this point.

7.3.3 Gettering

The difference of absolute lifetimes for the best and worst areas, prior to gettering, is small and overall lifetimes are very low. The gettering process improved the lifetime drastically in MH2, and it is obvious that interstitially bonded impurities have been removed from the grains. MH2 obtained better lifetimes after gettering than ES2 (8.54 to 30.0 μs at ~ 50 % height), and it implies the presence of interstitially dissolved chromium which has been gettered externally at low energy sites within the crystal structure of MH2. With no addition of chromium ES2 should be a cleaner material than MH2, and the lifetime improvement is consequently less. Other factors than interstitial impurities must also contribute to lifetime degradation in ES2.

At 97 % height most of the transition elements have probably been precipitated and only a small fraction of the interstitially bonded species are left in the grains. Therefore only minor enhancements in lifetime occur. Another possibility is that equilibrium has been reached between the removal of interstitial impurities and the dissolution of precipitates, releasing interstitial elements simultaneously as removing them. Furthermore, at this height the wafer is in the dendritic region, where most impurities are found as larger complexes and particles.

Since the silicon material is basically non-homogeneous the improvements can vary considerably from region to region of each wafer. A surprising observation occurred when studying the lifetime maps before and after gettering. The best and the worse areas of the wafers are inverted after the gettering process, i.e. areas with high minority carrier lifetimes prior to gettering experienced what seems to be less effect from the gettering and were altered to the worst area with lowest minority carrier lifetime after gettering.

As mentioned previously, the master thesis work of Nærland [91] led to some of the same observations when she investigated the corresponding lifetime, grain orientation and iron concentration maps in the red zone. In the red zone area, twin boundaries were analogous to the lowest lifetimes obtained and areas of high angle grain boundaries (and dislocations) provided highest lifetime. During gettering the impurities have probably diffused longer than during the post-solidification annealing and hence dislocations and grain boundaries have discharged also larger grains and twins for impurities. After gettering the lifetime is thus improved considerably within the grains and at twin boundaries.

Another explanation for the inversion of the lifetime regions of high dislocation density was provided by Kvande [25] for an iron doped multicrystalline ingot. She suggests that strong trapping effects are the reason that areas of numerous defects provide high minority carrier lifetime. Macdonald *et al.* [92] claimed that the trapping levels originate from the boron-interstitial impurity pair. The strong trapping is not occurring for the reference casting, ES2, and hence it may seem to be related to chromium, as Kvande related it to iron. If this is the case, the chromium must be present as interstitial specie where the trapping consequently originate from the chromium-boron defect level functioning more like a trapping level than recombination centre.

Prior to gettering, the highest lifetime regions in wafers from MH2 corresponds to a "boundary" between an area with large grains and twin boundaries, and an area with higher dislocation density and many, small grains. The gettering process is long enough to getter most of the dissolved interstitial species, and hence a significant increase in lifetime is observed in these regions. The dissolved impurities are gettered at low-energy sites, i.e. grain boundaries and dislocations, which do not undergo quite the same enhancement in lifetime.

Even though the grain structure does impact lifetime, metal impurities appear to have a more dominating role and be the reason for the detrimental properties in silicon. Generally, such a great enhancement in lifetime as observed for MH2 after gettering supports the fact that most of the chromium must be bonded interstitially.

7.3.4 Solar cell characteristics

The solar cell properties of ES1 and ES2 are not included in the results section. Large scattering in the fill factor between neighboring wafers were observed. Even though ES1 have similar J_{SC} and V_{OC} behavior to R5 the fill factor is substantially lower implying that the process conditions rather than the material itself degrade the cells. The reference castings for MH1 and MH2 within this section is thus R5 and R6.

The open circuit voltage is slightly higher for MH2 than MH1. Low resistivity normally gives high open circuit voltage, but this is not the case for these solar cells. Both the reference cells and MH2 show comparable voltages to what is usually obtained, some examples are given in Table 2 and Table 3.

The short circuit current density for MH1 is substantially lower than for the reference cells, which implies poor material quality. Since both oxygen and aluminum is present in considerable amounts, it cannot be ruled out completely that these impurities have an impact on J_{SC}. Despite the same amount of added chromium, MH2 show much better quality and hence the poor characteristics of MH1 can be due to other factors than the material quality.

The short circuit current density as well as the open circuit voltage of MH1 is substantially lower than reported by Green *et al.* [29] for multicrystalline solar cells.

Green reported the best recorded solar cell efficiencies for each solar cell material type; an extraction is shown in Table 2. However, these cells are not of the same area or resistivity as cells of the MH ingots, and efficiencies are achieved in lab scale.

The fill factor computed for MH1 is a pseudo-FF which simply accounts for shunt resistance while any series resistance is not considered. Hence, the resistivity of the material is not taken into account due to the fact that resistivity of the material itself is negligible compared to the resistance of the emitter sheet and contact. For MH2 the FFs are recorded as normal from the maximum power point in the I-V curve, as shown in Figure 6. There is a large scattering in the fill factor for neighboring wafers of MH1 as well as being overall lower than for standard solar cells. The large scattering is affected by the processing conditions to which the wafers are subjected to and results of the solar cells from MH1 are consequently not reliable.

It is not likely that the variation between neighboring wafers is due to the material. Several emitter thicknesses and firing temperatures have been tried without luck. A low resistivity and non-optimal process conditions for small wafers, including the drying conditions for the metal contact paste applied, contributes to the above mentioned challenges. Also the measurement "chuck" is not adapted to 50x50 mm^2 wafers. Further investigations performed at ISC Konstanz included the study of edge isolation by thermal imaging. A large edge effect due to rough edges influenced the small 50x50 mm^2 cells and resulted in large scattering effects for solar cell characteristics, especially fill factor, of MH1 as well as ES1/2. Fine laser cutting of the edges provided proper edge insulation and eliminated the scattering results.

In MH2 the appropriate adjustment of the process has been conducted and only small scattering effects are present. Consequently the cells of MH2 are comparable to the references and can even match the J_{SC} and V_{OC} of some commercial cells.

All the aspects discussed above, especially the low J_{SC} and V_{OC} of MH1, are reflected in the low average solar cell efficiency. Cells close to the top and bottom of the ingots have very poor solar cell characteristics. It is not surprising that a decrease occurs at the top where the wafers are in the dendritic region, with high impurity concentrations due to segregation. The bottom contains high concentrations of iron and somewhat higher oxygen content from the diffusion from crucible and coating. In addition, there is probably no planar solidification front at this point and consequently the solar cell efficiency will be severely degraded.

It is more realistic to compare the solar cells from MH1 and MH2 with the reference castings as well as previous results reported by Hoffmann *et al.* [31] than performances of ES1/ES2. The cells produced by 100 % ESS^{TM} showed efficiencies of 15.4 %, which is slightly higher than achieved for MH2. However, polysilicon cells from an ingot produced in the same furnace as MH2 give similar efficiencies. Ingot number 2 shown in Table 3 [7], with comparable resistivity and size to these cells, obtained short circuit current density and fill factor of 30 mA/cm^2 and 74 respectively. This is comparable to the values obtained for MH2.

J_{SC} for MH1 is lower than both MH2 and the reference ingots, while MH2 match these. Additionally, a significantly lower fill factor and efficiency is achieved for MH1. Based on problems with great variations in fill factor for MH1 between neighboring wafers, the short circuit current density should rather be compared than fill factor and efficiency. For cells from MH2 another situation occurs, the efficiencies are as good or even higher compared to R5 and R6.

The resistivity will influence the efficiency of the solar cell. Gessert *et al.* [95] reported a peak efficiency corresponding to a value of 0.8 Ω cm in mc-silicon. The low resistivity of the wafers (average of 0.5 Ω cm up to ~75 %) is a contributor to degradation of cell performance due to the decreasing depletion region width. However, the silicon material resistivity is not dominating in these cells, as mentioned previously.

The area of the solar cell can also be a contributor to low efficiencies. The cells produced of the ES and MH castings are 50x50 mm^2 while commercial solar cells are typically 156x156 mm^2. The small cells can show better or worse efficiencies depending on the grain structure included in the measured area. If only few, larger grains discharged for impurities are present in the cells, the efficiency will be drastically enhanced compared to a cell with several large defect clusters decorated with precipitates. The larger cell size of cells reported by Hoffmann *et al.* [31] can contribute negatively or positively compared to the measured efficiency of MH2.

It is clear that the poor solar cell properties and scattering effects between neighboring wafers obtained for ES1/2 and MH1 are due to non-optimal process conditions and not the material itself. The new edge insulation technique is to be performed on cells from ES1/2.

As demonstrated by the cell of MH2 solar cell efficiencies can match commercial solar cells by adjusting the process to the material. The chromium impurities added to MH2 seems to be, in accordance with the gettering experiments, non-detrimental to the complete solar cells. The impurities are confined to defects in the material. The difference in total concentration of impurities of SoG-silicon compared to polysilicon is of less importance as long as appropriate high temperature and solar cell processing is applied.

8 Conclusion

The electrical properties of two chromium doped compensated SoG-silicon ingots have been investigated. The material quality from as-cast ingot to solar cells was studied by means of chemical analysis, lifetime mapping, grain orientation, precipitation investigations, resistivity measurements and mapping of dislocation density.

The grade of compensation is not as significant in ESS^{TM} compared to the reported acceptor and donor concentration for other compensated materials. Due to dendritic solidification at the top of the ingots no p- to n-type transition could be observed.

In general the chromium-doped ingots investigated contained low concentrations of metallic impurities, approaching the detection limit of the GDMS instrument at 50 % ingot height. Chromium has segregated well despite the high concentrations added to MH1 and MH2. However, the low contamination levels measured in these ingots are still detrimental to the bulk properties of silicon. Chromium strongly reduced the minority carrier lifetime in MH1 and MH2. The solubility limit of chromium has not been exceeded and great improvements in lifetime after gettering, corresponding to two orders of magnitude, imply that the chromium is not exclusively confined to defects, but are mainly found as an interstitially dissolved element. The exceptions are particles of 1-3 μm size precipitated on grain boundaries that could clearly be detected in wafers originating from 90 % ingot height.

Chromium-boron or iron-boron pairs was not detected, due to the initially very low carrier lifetimes which constituted minor or no variation in lifetime between the interstitial species and their respective boron pairs. Chromium behaves similarly to iron with respect to the segregation, distribution and impact on electrical properties. Good correspondence exists between the observations in this thesis to the observations made by Kvande [25] in an identical size iron doped multicrystalline silicon ingot.

Exceptionally high concentrations of aluminum contributed to the net majority carrier content, while minority carrier lifetime was unaffected. Aluminum is a slow diffuser and would therefore have slowed down the gettering process if it had substantial impact on the electrical properties of silicon.

The grain structure does not have a direct impact on the electrical properties in the ingots investigated. However, when the grain boundaries are heavily decorated with metal precipitates the lifetime is considerably lowered compared to the surrounding grains. Metal impurities are the dominating factor influencing the minority carrier lifetime and diffusion lengths in SoG-silicon material. The total impurity content of fast diffusing elements is of less relevance as long as their diffusion length extends to a low energy precipitation site.

9 Further work

The work of this thesis has included a wide range of characterizing techniques for chromium doped materials. Going deeper into all the details of the most interesting features and results has not been possible, but would substantiate the work from this thesis and lead to a more comprehensive understanding of the effect on contaminations in SoG-silicon.

To investigate the distribution of precipitates and clusters of particles, especially chromium, several characterization analyses should be performed;

- EBIC of wafers from different heights and in comparison with ES ingots to study the extent and location of precipitates as well as to analyze the composition of precipitates by Auger spectroscopy
- Transmission Electron Microscope (TEM) to search for particles on grain boundaries and Electron Dispersive Spectroscopy (EDS) or an equivalent technique in order to characterize the particles
- DLTS scan of the silicon band gap to position defect levels originating from different atomic states of diverse impurities, e.g. interstitial chromium versus chromium boron pairs

Contributing to understanding the complex of which state the impurity elements are in and how defects and crystal structure interact with the impurities, additional work must be performed;

- Gettering of wafers from other heights in MH2 as well as in MH1, ES1 and ES2, which can imply the state of the impurity atoms
- LBIC of solar cells parallel to images obtained from PVScan (dislocation density) and μw-PCD (lifetime)
- EBSD grain orientation mapping of MH2 to complete the results
- Heat treatments to dissolve Cr precipitates and study their interaction with other impurities, e.g. oxygen

10 References

1. Solarbuzz. *Marketbuzz - Annual World Solar Photovoltaic Market Growth*. [cited 2009 26.01]; Available from: http://www.solarbuzz.com.
2. Istratov, A.A., et al., *Control of metal impurities in "dirty" multicrystalline silicon for solar cells.* Materials Science and Engineering B, 2006. **134**: p. 282-286.
3. Nelson, J., *The Physics of Solar Cells*. 2005, London: Imperial College Press.
4. Davis, J.R., et al., *Impurities in Silicon Solar Cells*, in *IEEE Transactions on Electron Devices*. 1980. p. 677-687.
5. Green, M.A., *Solar Cells - Operating Principles, Technology and System Applications*. 1998, Kensington: Prentice-Hall Inc.
6. Aldous, S. *Anatomy of a solar cell*. How Solar Cells Work [cited 2009 04]; http://science.howstuffworks.com/solar-cell3.htm.
7. Zahedi, C., et al., *Solar Grade Silicon from Metallurgical Route*, in *PVSEC-14*. 2004: Bangkok.
8. Dubois, S., et al., *Beneficial effects of dopant compensation on carrier lifetime in upgraded metallurgical silicon*, in *23rd EU-PVSEC*. 2008: Valencia.
9. Kopecek, R., et al. *Light induced degradation in compensated SoG-Si material: effect of reduced B-O complex formation*. in *Crystal Clear Workshop*. 2008. Amsterdam.
10. Peter, K., et al., *Future Potential For SoG-Si Feedstock from the Metallurgical Route*, in *23rd EU-PVSEC*. 2008: Valencia.
11. Dubois, S., et al., *Light-Induced Degradation and Regeneration in Compensated Upgraded Metallurgical silicon.*
12. Flemings, M.C., *Solidification Processing*. 1974: McGraw-Hill.
13. Kurz, W. and D.J. Fisher, *Fundamentals of Solidification*. 4th ed. ed. 1998: Trans Tech Publications.
14. Trumbore, F.A., *Solid solubilities of impurity elements in germanium and silicon*, in *Technology of Semiconductors*, Muehlbauer, Editor. 1960, Bell Laboratories: New Jersey.
15. Nozaki, T., et al., *Behaviour of light impurity elements in the production of semiconductor silicon*, in *Technology of Semiconductors*, Muehlbauer, Editor. 1974, Akadémiai Kiadó: Japan. p. 109.
16. Hopkins, R.H., et al., *Silicon materials task of the low cost solar array project - Fourth quarterly report*, in *Technology of Semiconductors*, Muehlbauer, Editor. 1976, Dow Corning Corp.: Hemlock, US.
17. Fischler, S., *Correlation between Maximum Solid Solubility and Distribution Coefficient for Impurities in Ge and Si*, in *Technology of Semiconductors*, Muehlbauer, Editor. 1962: Massachusetts.
18. Kalejs, J.P., B. Bathey, and C. Dube, *Segregation and impurity effects in silicon grown from the melt in the presence of second phase formation.* Journal of Crystal Growth, 1991. **109**: p. 174-180.
19. Istratov, A.A., et al., *Dependence on precipitation behavior of Cu and Ni in Cz and multicrystalline silicon on cooling conditions*, in *14th NREL Workshop on*

Crystalline Silicon Solar cell material, B. Sopori, Editor. 2004: Colorado, US. p. p.165.
20. Shockley, W. and W.T.R. Jr., *Statistics of the Recombination of Holes and Electrons.* Physical review, 1952. **87**(5): p. 835-842.
21. Markvart, T. and L. Castañer, *Solar Cells - Materials Manufacture and Operation: IIa-2 Semiconductor materials and Modelling*. 2005.
22. Ryningen, B., *Formation and growth of crystal defects in directionally solidified multicrystalline silicon for solar cells*, in *Department of Materials Science and Engineering*. 2008, NTNU: Trondheim.
23. Stokkan, G., *Characterization of Multricrystalline Silicon Solar Cells, Development of Characterization method for the combined effect of dislocations and grain boundaries on the minority carrier lifetime*, in *Department of Materials Science and Engineering*. 2004, NTNU: Trondheim.
24. Seifert, W., G. Morgenstern, and M. Kittler, *Influence of dislocation density on recombination at grain boundaries in multicrystalline silicon.* Semiconductor Science Technology, 1993. **8**: p. 1687-1691.
25. Kvande, R., *Incorporation of Impurities during Directional Solidification of multicrystalline silicon for Solar Cells*, in *Department of Materials Science and Engineering*. 2008, NTNU: Trondheim.
26. Martinuzzi, S., et al., *P-type vs. N-type Wafers from the Metallurgical Route*, in *23rd EU-PVSEC*. 2008: Valencia.
27. Macdonald, D., *Recombination and Trapping in Multicrystalline Silicon Solar Cells*. 2001, The Australian National University: Canberra.
28. Markvart, T., *Solar Electricity*. 2nd ed. 2000, Southampton: John Wiley & Sons.
29. Green, M.A., et al., *Solar Cell Efficiency Tables (Version 32).* Progress in Photovoltaics: Research and Applications, 2008. **16**: p. 435-440.
30. Kaes, M., et al., *Over 18 % Efficient Mc-Si Solar Cells From 100 % Solar Grade Silicon Feedstock from a Metallurgical Process Route.*
31. Hoffmann, V., et al. *First results on industralization of Elkem Solar Silicon at Pillar JSC and Q-cells*. in *23rd EU-PVSEC*. 2008. Valencia.
32. Ludwig, G.W. and H.H. Woodbury, *Electron Spin Resonance in Semiconductors*, in *Solid State Physics*, F. Seitz and D. Turnbull, Editors. 1962, Academic Press: New York. p. 223.
33. Woodbury, H.H. and G.W. Ludwig, *Spin Resonance of Transition Metals in Silicon.* Physical review, 1960. **117**(1): p. 102-108.
34. Macdonald, D., et al., *Impurities in Solar-Grade Silicon and their Characterisation*, in *22nd European Photovoltaic Solar Energy Conference*. 2007: Milan, Italy. p. 820-828.
35. Buonassisi, T., et al., *Synchrotron-based investigations of the nature and impact of iron contamination in multicrystalline silicon solar cells.* Journal of Applied Physics, 2005. **97**(7): p. 074901.
36. Macdonald, D., et al., *Transition-metal profiles in a multicrystalline silicon ingot.* Journal of Applied Physics, 2005. **97**: p. 033523-1 - 033523-7.
37. Lebedev, A.A. and N.A. Sultanov, Sov. Phys. Semicond., 1970. **4**.

38. Schmidt, J., et al., *Recombination activity of interstitial chromium and chromium-boron pairs in silicon.* Journal of Applied Physics, 2007. **102**: p. 123701-1 - 123701-10.
39. Istratov, A.A., et al., *Metal content of multicrystalline silicon for solar cells and its impact on minority carrier diffusion length.* Journal of Applied Physics, 2003. **94**(10): p. 6552-6559.
40. Macdonald, D., et al., *Phosphorus Gettering in multicrystalline silicon studied by Neutron Activation Analysis*, in *29th IEEE PVSC*. 2002: New Orleans, U.S.
41. Geerligs, L.J., et al. *Specification of Solar Grade Silicon: How common impurities affect the cell efficiency of mc-silicon solar cells*. in *20th European Photovoltaic Solar Energy Conference and Exhibition*. 2005. Barcelona, Spain.
42. McHugo, S.A., et al., *Direct correlation of transition metal impurities and minority carrier recombination in multicrystalline silicon.* Journal of Applied Physics Letters, 1998. **72**(26): p. 3482-3484.
43. McHugo, S.A., et al., *Nanometer-scale precipitates in multicrystalline silicon solar cells.* Journal of Applied Physics, 2001. **89**(8): p. 4282-4288.
44. Park, S.H., D.K. Schroder, and J.P. Kalejs, *Electrical Behavior of Chromium-contaminated EFG silicon*, in *IEEE*. 1991. p. 864-868.
45. Zeman, M., *Solar Cells*. 2007, Technical University of Delft: Delft, Netherlands.
46. Holt, A., E. Enebakk, and A.-K. Soiland, *Effect of Impurities in the Minority Carrier Lifetime of Silicon made by the Metallurgical Route.* 2007.
47. Mjøs, Ø., *Directional Solidification of Silicon for Solar Cells*, in *Department of Materials Science and Engineering*. 2006, NTNU: Trondheim.
48. Cuevas, A., et al., *Recombination and Trapping in multicrystalline silicon*, in *IEEE Transactions on Electron Devices*. 1999. p. 2026-2034.
49. Schroeter, W. and M. Seibt, *Solubility and diffusion of transition metal impurities in c-Si*
in *Properties Crystalline Silicon* R. Hull, Editor. 1999, Institution of Engineering and Technology.
50. Perichaud, I., *Gettering of impurities in solar silicon.* Solar Energy Materials & Solar Cells, 2002. **72**: p. 315-326.
51. Bentzen, A., *Phosphorus diffusion and gettering in silicon solar cells*, in *Department of Physics*. 2006, University of Oslo: Oslo.
52. Bothe, K. and J. Schmidt, *Electronically activated boron-oxygen-related recombination centers in crystalline silicon.* Journal of Applied Physics, 2006. **99**(1): p. 013701.
53. Bothe, K., R. Hezel, and J. Schmidt, *Understanding and Reducing the Boron-Oxygen Related Performance Degradation in Czochralski Silicon Solar Cells.* Solid State Phenomena, 2004. **95**: p. 223-228.
54. Istratov, A.A., H. Hieslmair, and E.R. Weber, *Iron and its complexes in silicon.* Journal of Applied Physics A, 1999. **69**: p. 13-44.
55. Coletti, G., et al., *Effect of iron in silicon feedstock on p- and n-type multicrystalline silicon solar cells.* Journal of Applied Physics, 2008. **104**(10): p. 104913.
56. Istratov, A.A., H. Hieslmair, and E.R. Weber, *Iron contamination in silicon technolgy.* Journal of Applied Physics A, 2000. **70**: p. 489-534.

57. Martinuzzi, S., S. Dubois, and N. Enjalbert. *Minority Carrier Lifetime and Diffusion length in voluntarily Chromium contaminated n-type mc-Si wafers*. in *23rd EU-PVSEC*. 2008. Valencia.
58. Mishra, K., *Identification of Cr in p-type silicon using the minority carrier lifetime measurement by the surface voltage method.* Journal of Applied Physics Letters, 1996. **68**(23): p. 3281-3283.
59. Dubois, S., O. Palais, and P.J. Ribeyron, *Determination at 300 K of the hole capture cross section of Chromium-Boron pairs in p-type silicon.* Journal of Applied Physics Letters, 2006. **89**: p. 232112-1 - 232112-3.
60. Conzelmann, H., K. Graff, and E.R. Weber, *Chromium and Chromium-Boron Pairs in Silicon.* Journal of Applied Physics, 1983. **30**: p. 169-175.
61. Bathey, B.R., et al., *The Effects of Cr on Edge-defined Film-fed Growth (EFG) polycrystalline silicon for solar cells*, in *IEEE*. 1990. p. 687-690.
62. Schmidt, et al. in *22nd European Photovoltaic Solar Energy Conference*. 2007. Milan, Italy.
63. Bendik, N.T., V.S. Garnyk, and L.S. Milevskii, Sov. Phys. Sol. State, 1970. **12**(150).
64. Dubois, S., et al., *Dissolved chromium in crystalline silicon - Detection and Impact on solar cell performances*, in *22nd European Photovoltaic Solar Energy Conference* 2007: Milan, Italy. p. 1193-1196.
65. Dubois, S., N. Enjalbert, and J.P. Garandet, *Effects of the compensation level on the carrier lifetime of crystalline silicon.* Applied Physics Letters, 2008. **93**(3): p. 032114.
66. Macdonald, D., et al., *Doping dependence of the carrier lifetime crossover point upon dissociation of iron-boron pairs in crystalline silicon.* Applied Physics Letters, 2006. **89**(14): p. 142107.
67. Birkholz, J.E., et al., *Electronic properties of iron-boron pairs in crystalline silicon by temperature- and injection-level-dependent lifetime measurements.* Journal of Applied Physics, 2005. **97**(10): p. 103708.
68. Macdonald, D.H., L.J. Geerligs, and A. Azzizi, *Iron detection in crystalline silicon by carrier lifetime measurements for arbitrary injection and doping.* Journal of Applied Physics, 2004. **95**(3): p. 1021-1028.
69. Rein, S., et al., *Lifetime spectroscopy for defect characterization: Systematic analysis of the possibilities and restrictions.* Journal of Applied Physics, 2002. **91**(4): p. 2059-2070.
70. Rosenits, P., et al., *Determining the defect parameters of the deep aluminum-related defect center in silicon.* Applied Physics Letters, 2007. **91**(122109): p. 1-3.
71. Rodot, M., et al., *Al-related recombination center in polycrystalline Si.* Journal of Applied Physics, 1987. **62**(6): p. 2556-2558.
72. Roth, T., et al., *Titanium-related defect levels in silicon analyzed by temperature-dependent photoluminescence lifetime spectroscopy*, in *33rd IEEE PVSEC* 2008: San Diego.
73. Rohatgi, A., et al., *Effect of titanium, copper and iron on silicon solar cells.* Solid-State Electronics, 1980. **23**(5): p. 415-422.

74. Buonassisi, T., et al., *Chemical Natures and Distributions of Metal Impurities in Multicrystalline Silicon Materials.* Progress in Photovoltaics: Research and Applications, 2006. **14**: p. 513-531.
75. *Finnigan Element GD Hardware Manual*. 2005, Thermo Electron Company.
76. *Product brochure: Thermo Scientific ELEMENT GD Glow Discharge Mass Spectrometer*. 2008 [cited 04/2009]; Available from: http://www.thermo.com/eThermo/CMA/PDFs/Product/productPDF_25212.pdf.
77. *Electron Backscattered Diffraction - Explained*. 2004, Oxford Instruments Analytical. p. 1-31.
78. West, A.R., *Basic Solid State Chemistry*. 2nd ed. 1999, Chichester: John Wiley & Sons.
79. Lauer, K., et al., *Detailed analysis of the microwave-detected photoconductance decay in crystalline silicon.* Journal of Applied Physics, 2008. **104**(10): p. 104503.
80. Sopori, B., et al., *High-speed mapping of grown-in defects and their influence in large-area silicon photovoltaic devices.* Journal of Crystal Growth, 2000. **210**(1-3): p. 346-350.
81. *ASTM F 723-99*, in *Standard Practice for Conversion Between Resistivity and Dopant Density for Born-doped, Phosphorus-doped and Arsenic-doped Silicon*. 1999.
82. Sinton, R.A., A. Cuevas, and M. Stuckings, *Quasi-Steady-State Photoconductance, A new method for solar cell material and device characterization*, in *25th IEEE Photovoltaic Specialists Conference*. 1996: Washington D.C., U.S. p. 457-460.
83. Schubert, M.C., J. Isenberg, and W. Warta, *Spatially resolved lifetime imaging of silicon wafers by measurement of infrared emission.* Journal of Applied Physics, 2003. **94**(6): p. 4139-4143.
84. Isenberg, J., et al., *Imaging method for laterally resolved measurement of minority carrier densities and lifetimes: Measurement principle and first applications.* Journal of Applied Physics, 2003. **93**(7): p. 4268-4275.
85. Leamy, H.J., *Charge collection scanning electron microscopy.* Journal of Applied Physics, 1982. **53**(6): p. R51-R80.
86. Reniers, F. and C. Tewell, *New improvements in energy and spatial (x, y, z) resolution in AES and XPS applications.* Journal of Electron Spectroscopy and Related Phenomena, 2005. **142**: p. 1-25.
87. *Documentation manual for Crystalox DS 250*, Crystalox Inc.
88. Sopori, B., *A new defect etch for polycrystalline silicon.* Journal of Electrochem. Soc., 1984. **131**(3): p. 667-672.
89. ASTM, *Standard test method for Interstitial Atomic Oxygen Content of Silicon by infrared absorption.* **F1188-93a**.
90. Modanese, C., et al., *(unpublished work)*, Department of Materials Science and Engineering: Trondheim.
91. Nærland, T., *Investigation of the causes for red zone in multicrystalline silicon*, in *Department of Materials Science and Engineering*. 2008, NTNU: Trondheim.
92. Macdonald, D., M. Kerr, and A. Cuevas, *Boron-related minority-carrier trapping centers in p-type silicon.* Applied Physics Letters, 1999. **75**(11): p. 1571-1573.

93. Hassler, C., et al., *Formation and annhilation of oxygen donors in multicrystalline silicon for solar cells.* Materials Science and Engineering B, 2000. **71**: p. 39-46.
94. O'Mara, W.C., R.B. Herring, and L.P. Hunt, *Handbook of semiconductor silicon technology*. 1990, William Andrew Publishing/Noyes.
95. Gessert, C., D. Helmreich, and M. Peterat. *Recent Advances in SILSO Casting*. in *6th Photovoltaic Solar Energy Conference*. 1985. London.

APPENDICES

A: Calculating the effective segregation coefficient

B: Complete ICP-MS analysis of MH1 and MH2

C: Lifetime maps recorded by μw-PCD before and after gettering

D: Dislocation density maps measured by PVScan

APPENDIX A

The effective segregation coefficient was calculated by the least squares method. An example is given below for chromium.

$$C_s^* = kC_0(1-f_s)^{(k-1)}$$

$$SQ = (GDMS - C_s^*)^2$$

$k_0 = 1.0 \cdot 10^{-5}$

$C_0 = 11.5$ ppbw

f_s	height from bottom (mm)	Cs (ppbwt)	GDMS (ppbwt)	SQ	Σ (SQ)
0.999	106.0	0.115	2.803	7.225	815.990
0.981	104.0	0.006	17.009	289.087	
0.972	103.0	0.004	21.249	451.349	
0.953	101.0	0.002	4.545	20.632	
0.943	100.0	0.002	2.968	8.795	
0.915	97.0	0.001	1.853	3.428	
0.906	96.0	0.001	4.987	24.854	
0.873	92.5	0.001	0.913	0.832	
0.863	91.5	0.001	1.569	2.460	
0.840	89.0	0.001	0.774	0.599	
0.830	88.0	0.001	1.767	3.122	
0.736	78.0	0.000	0.826	0.681	
0.726	77.0	0.000	0.913	0.834	
0.425	45.0	0.000	0.517	0.267	
0.415	44.0	0.000			
0.123	13.0	0.000			
0.113	12.0	0.000	1.032	1.065	
0	0.0	0.000	0.873	0.762	

Microsoft Office Excel 2003:
- Tools
- Solver…

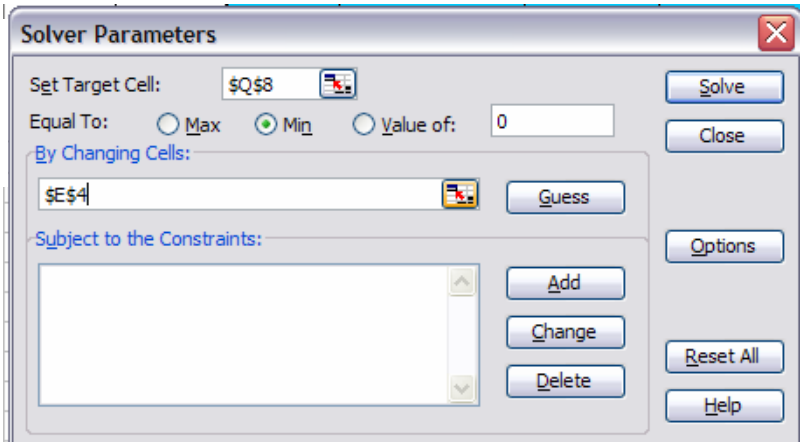

APPENDIX B

The complete ICP-MS measurements of the two ingots are shown below.
Abbreviation ‘e’ stands for edge and ‘c’ stands for centre (e.g. MH1-Ae: ingot MH1, position A, edge measurement).

Element	MH1-Ae	MH1-Ac	MH1-Be	MH1-Bc	MH1-Ce	MH1-Cc	MH1-De	MH1-Dc	MH1-Ee	MH1-Ec
Al	< 0.4	1.1	0.54	< 0.4	< 0.4	< 0.4	0.62	< 0.4	30	1.8
Ca	2.6	2.7	5.1	2.9	2.8	3.4	2.4	2.5	5.5	3.6
Cr	< 0.5	1.0	< 0.5	< 0.5	< 0.5	< 0.5	< 0.5	< 0.5	>97	3.7
Cu	< 0.5	< 0.5	< 0.5	< 0.5	< 0.5	< 0.5	< 0.5	< 0.5	< 0.5	<0.5
Fe	< 2	< 2	9.02 / 2.82	2.1	< 2	< 2	2.7	< 2	< 2	<2
Mn	< 0.1	< 0.1	< 0.1	< 0.1	< 0.1	< 0.1	< 0.1	< 0.1	< 0.1	<0.1
Ni	< 0.3	< 0.3	< 0.3	< 0.3	< 0.3	< 0.3	< 0.3	< 0.3	< 0.3	<0.3
Ti	< 0.2	< 0.2	< 0.2	< 0.2	< 0.2	< 0.2	< 0.2	< 0.2	< 0.2	<0.2
V	< 0.1	< 0.1	< 0.1	< 0.1	< 0.1	< 0.1	< 0.1	< 0.1	< 0.1	<0.1
P	< 0.5	< 0.5	< 0.5	< 0.5	< 0.5	< 0.5	0.65	0.67	2.1	1.1

Element	MH2-Ae	MH2-Ac	MH2-Be	MH2-Bc	MH2-Ce	MH2-Cc	MH2-De	MH2-Dc	MH2-Ee	MH2-Ec
Al	<0.4	<0.4	<0.4	< 0.4	<0.4	<0.4	<0.4	<0.4	<0.4	<0.4
Ca	<1	<1	<1	2.9	<1	<1	<1	<1	<1	1.6
Cr	<0.5	<0.5	<0.5	< 0.5	<0.5	<0.5	<0.5	<0.5	2.8	56
Cu	<0.5	<0.5	<0.5	< 0.5	<0.5	<0.5	<0.5	<0.5	<0.5	<0.5
Fe	<2	<2	<2	2.1	<2	<2	<2	<2	<2	<2
Mn	<0.1	<0.1	<0.1	< 0.1	<0.1	<0.1	<0.1	<0.1	<0.1	<0.1
Ni	<0.3	<0.3	<0.3	< 0.3	<0.3	<0.3	<0.3	<0.3	<0.3	<0.3
Ti	<0.2	<0.2	<0.2	< 0.2	<0.2	<0.2	<0.2	<0.2	<0.2	<0.2
V	<0.1	<0.1	<0.1	< 0.1	<0.1	<0.1	<0.1	<0.1	<0.1	<0.1
P	<0.5	<0.5	<0.5	< 0.5	<0.5	<0.5	<0.5	<0.5	1	1.6

APPENDIX C

Lifetime maps before and after gettering for three additional heights to what has already been presented.

MH2-205
87.2 % height

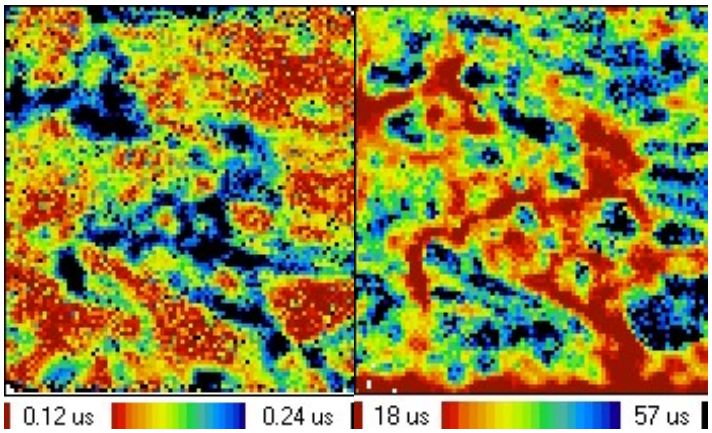

MH2-216
91.9 % height

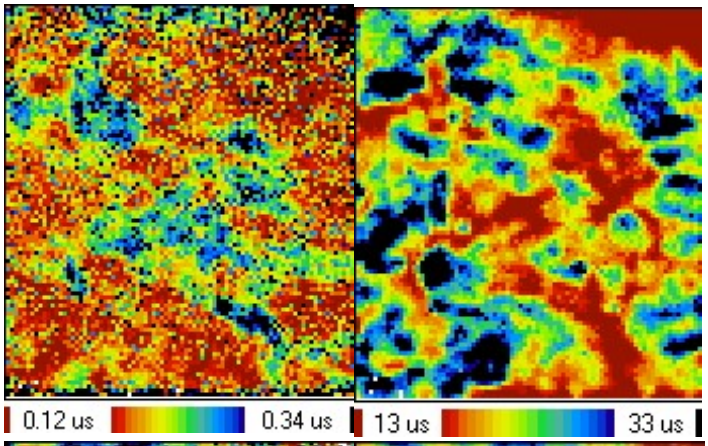

MH2-228
97.0 % height

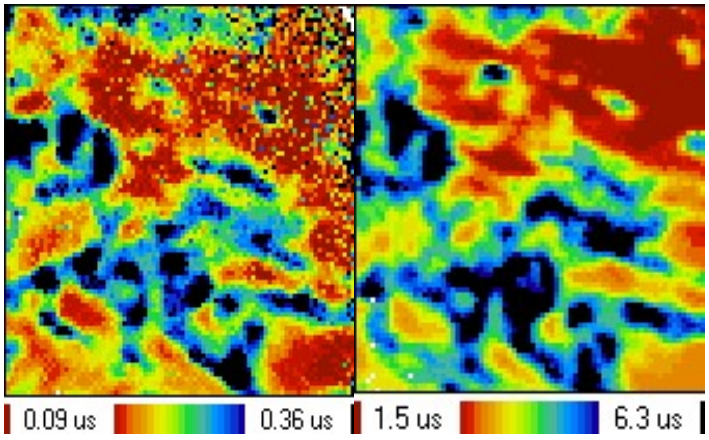

APPENDIX D

The complete collection of dislocation density maps recorded by a PVScan 6000 instrument. The maps are shown in descending order and hold a common scale bar.

Maps of ingot MH1:

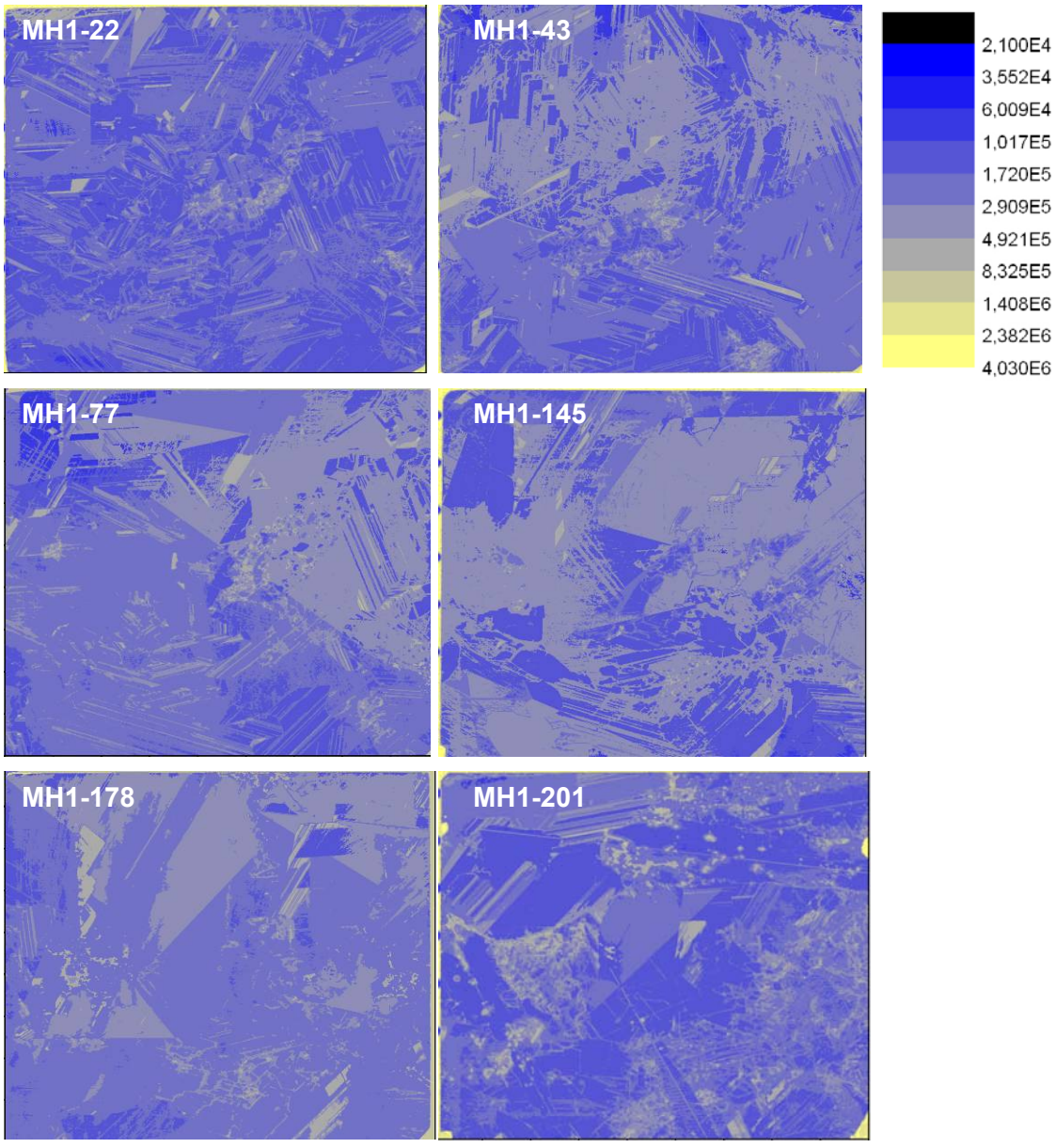

Maps of ingot MH2: